Tuning Electron Transport in Metal Films and Graphene with Organic Monolayers

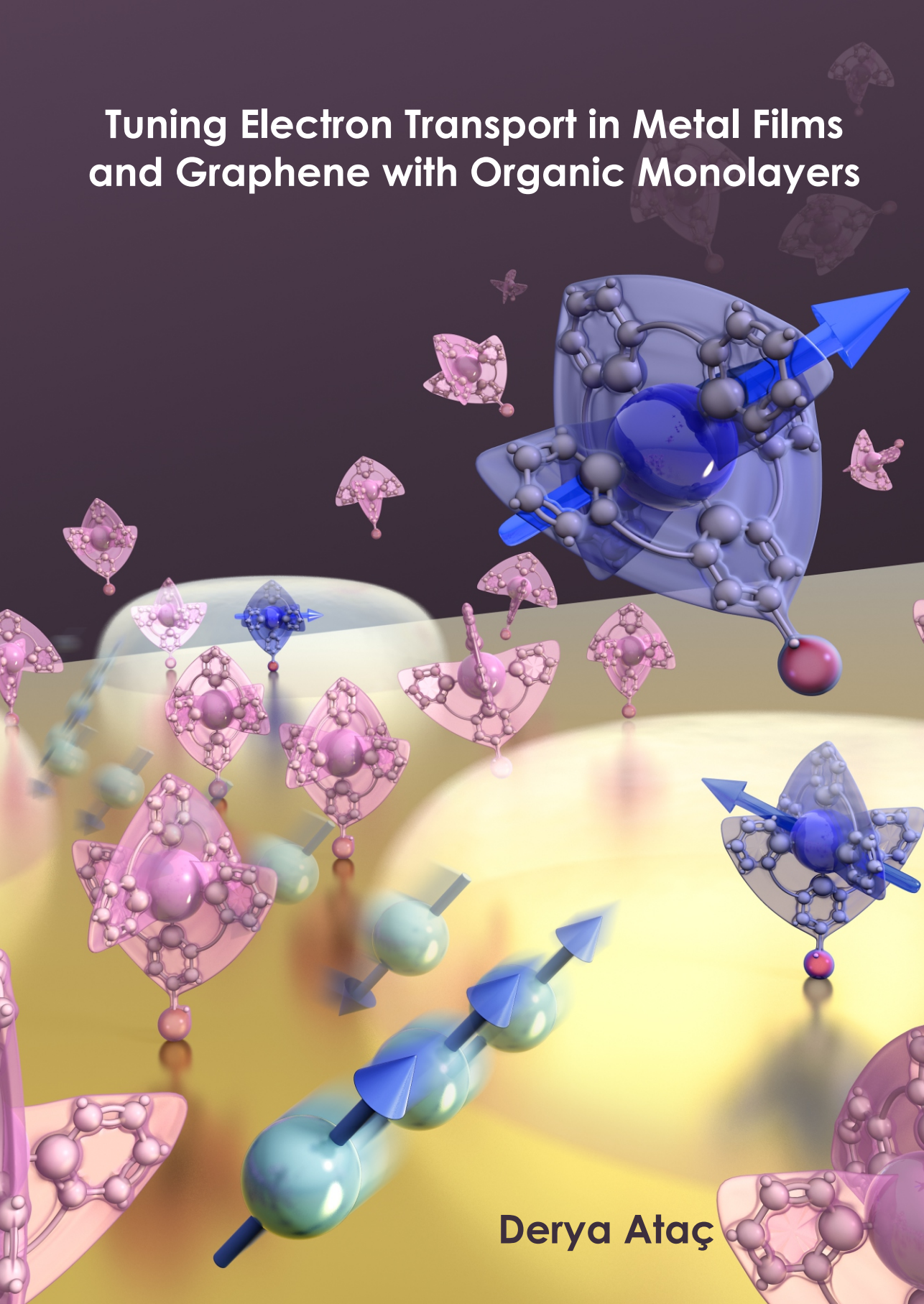

Derya Ataç

TUNING ELECTRON TRANSPORT IN METAL FILMS AND GRAPHENE WITH ORGANIC MONOLAYERS

Derya Ataç

The research described within this thesis was carried out in the NanoElectronics Group at the MESA+ Institute for Nanotechnology at the University of Twente, Enschede, The Netherlands. European Research Council (ERC) Starting Grant no. 240433 financially supported this research.

UNIVERSITY OF TWENTE.

NANOELECTRONICS.

MESA+
INSTITUTE FOR NANOTECHNOLOGY

erc
European Research Council
Established by the European Commission

Thesis committee members

Chairman & secretary:

Prof. dr. P. M. G. Apers	University of Twente

Promotors:

Prof. dr. ir. W. G. van der Wiel	University of Twente

Other members:

Prof. dr. ir. W. G. van der Wiel	University of Twente
Prof. dr. ir. Jurriaan Huskens	University of Twente
Prof. dr. ir. Harold Zandvliet	University of Twente
Assoc. Prof. dr. Cees Otto	University of Twente
Prof. dr. Bart Jan Ravoo	University of Münster, Germany
Adj. Prof. Tamalika Banerjee	University of Groningen
Dr. Monica Craciun	University of Exeter, United Kingdom

Title: Tuning Electron Transport in Metal Films and Graphene with Organic Monolayers
Author: Derya Ataç
Cover picture: Nymus 3D
Cover design: Derya Ataç

Printed by Gildeprint Drukkerijen, Enschede, The Netherlands, 2014.
ISBN: 978-90-365-3820-2
DOI: 10.3990/1.9789036538022

TUNING ELECTRON TRANSPORT IN METAL FILMS AND GRAPHENE WITH ORGANIC MONOLAYERS

DISSERTATION

to obtain

the degree of doctor at the University of Twente,

on the authority of the rector magnificus,

prof. dr. H. Brinksma,

on account of the decision of the graduation committee,

to be publicly defended

on Thursday 4 December 2014 at 14.45

by

Derya Ataç

born on 2 March, 1984

in Balikesir, Turkey

This dissertation has been approved by:

Promotor:

Prof. dr. ir. W. G. van der Wiel

This thesis is dedicated to my family.

Contents

Chapter 1

Introduction

In this chapter, hybrid organic-inorganic electronics, which combines inorganic and molecular components is briefly introduced. Self-assembled monolayers and graphene are mentioned as widely used components for the hybrid electronics for applications and fundamental research. Following, the outline of the thesis is presented.

1.1 Introduction

Conventional electronics mainly makes use of inorganic semiconductors like Si, inorganic insulators like SiO_2, and metals owing to their robust properties. The technological advances in micro- and nanofabrication enabled Si-based technology to shrink the transistor sizes down to below 20 nm [1]. However, further miniaturization of silicon-based integrated circuits is approaching its fundamental physical and economical limits. An alternative route for achieving even smaller sizes beyond the physical limit lies in hybrid electronics, where inorganic and organic (molecular) components are integrated [2]. This approach, combines the robustness of inorganic materials with the chemical tunability of organic molecules, and in principle allows for shrinking devices down to molecular sizes (1 nm, the aim of the field "molecular electronics").

In addition to its technological potential, hybrid electronics offers a wide spectrum for fundamental research. The possibility of engineering organic molecules at the atomic level, with a large choice of building elements is a major advantage. As will be shown in this work, it enables experimental investigation of some key problems in solid-state physics, like quantum coherence and magnetic interactions. As an example, a very important and critical issue is the understanding of electronic phenomena at the interface between inorganic and molecular materials, as they usually play a dominant role in the overall properties.

In hybrid systems, self-assembled monolayers (SAMs) are extensively used [3-6]. SAMs are organic assemblies formed simultaneously by the adsorption of molecular species from solution or the gas phase onto the surface of solids. The molecules or ligands that form the SAM chemisorb on the surface via their ‘head groups’ and then a slow (in comparison to the chemisorption process) reorganization follows. The adsorbed molecules can organize spontaneously into crystalline (or semicrystalline) structures. Since only a monolayer is anchored to the surface, they can be prepared in very small thicknesses in the 1-3 nm range and are patternable with 10-100 nm scale dimensions. It is easy to prepare SAMs and it does not require ultrahigh vacuum or other sophisticated equipment [5]. They allow construction of large-area two-dimensional systems. It is possible to engineer SAM molecules to obtain different electronic functionalities.

Molecular monolayers have been used for tuning metal workfunctions [7], for surface transfer doping of semi-conductors [8], for self-assembled-monolayer field-effect transistors [9], for modifying the electronic properties of graphene [10], and for uniform [11] and patterned [12] doping of silicon with donor atoms. In Chapter 4 of this thesis work, SAMs of organometallic complexes was used as magnetic doping elements, which resulted in a novel magnetic doping method. This method enables doping of metals with isolated magnetic impurities in a controlled way and without clustering, different from conventional alloying techniques. The method is easy to apply and highly reproducible. The obtained magnetic impurity doped metal provides a model system to learn about interesting physical phenomena such as the Kondo effect and RKKY.

Organometallic complexes (hereafter simply referred to as "metal complexes") that are used in this work are formed by complexation of functionalized terpyridine ligands with Co^{2+} or Zn^{2+} core ions . The molecules containing Co^{2+} ions are paramagnetic (spin 1/2), and these were used to integrate magnetic dopants into a thin film. On the other hand, the Zn^{2+} complex is non-magnetic (spin 0) and it was used to dilute the magnetic dopant concentration in a controlled way.

Another component that has attracted a significant attention in building hybrid electronic devices in recent years is graphene. Graphene is a two-dimensional crystal of carbon atoms arranged in a hexagonal lattice structure. Graphene is identified as a zero band gap semiconductor or semi-metal and has a novel electronic structure with its conduction band and valence band touching each other at the charge neutrality point (Dirac point). Around the Dirac point, the energy dispersion is linear and the carriers behave like massless relativistic particles [13-15]. It exhibits very high mobility (values up to 120000 $cm^2\ V^{-1}s^{-1}$ were observed in clean suspended graphene at 240 K). Its Fermi-energy can be tuned continuously by an electric field between the valence band, where current is carried by holes and the conduction band, where electrons carry the current. This possibility to control the carrier density in graphene by simple application of a gate voltage enables various electronic applications like field-effect transistors, sensors, memory devices etc. It should be noted that the gapless nature of graphene is also a weakness, since the absence of a band gap makes it very hard

to fabricate field effect devices with good on/off ratio. Introducing a band gap in graphene is still under investigation.

Apart from its technological use, graphene has great promise in fundamental research. In this work, as described in Chapter 6, we combined graphene with the SAMs of complexes with a different version of the metal Co^{2+} and Zn^{2+} terpyridine complexes, which was functionalized with an amine group instead of thiol group so that it can be assembled on SiO_2/Si substrates. It was aimed to tune the memory effect in graphene due to the charge transfer between the graphene and the metal complex.

1.2 Outline of the Thesis

In this thesis work, the electrical and magnetic properties of hybrid organic-inorganic electronic systems are investigated. Hybrid systems of a SAM of organometallic complexes in combination with a thin Au metal, as well as single-layer graphene were fabricated and studied to exploit the electron transport properties.

Chapter 2 provides an introduction to the theoretical concepts used in this work. First, the Kondo effect is discussed to describe electron-spin interactions and how they affect the electrical resistivity of a metallic system. Next, weak (anti-)localization is explained to understand the electron interference contribution to the resistivity in disordered metals. Subsequently, crystal field theory is introduced to explain the electronic structure and the origin of the spin of the molecular complexes used in this thesis work.

In Chapter 3, the experimental methods that were used throughout the thesis work are discussed. The preparation of SAMs on thin Au films and SiO_2/Si substrates, and the deposition techniques that were used for Au capping of the SAMs are explained. Next, low-temperature electric and magnetic characterization systems, synchrotron radiation techniques and surface-enhanced Raman spectroscopy are introduced.

In Chapter 4, a novel magnetic doping method using SAMs of organometallic complexes as magnetic doping agents is introduced. This method

consists of introducing a monolayer of paramagnetic molecules inside a disordered thin gold film. The molecules provides a robust way to control the concentration of magnetic impurities in the metal thin film. They enable doping of metals with isolated magnetic impurities in a controlled way and without clustering, different from conventional alloying techniques. The method was proved to be highly reproducible. The low-dimensional spin system obtained by this method enabled studying of the Kondo effect and quantum coherent transport, which also verified the success of the doping method.

In Chapter 5, the spin-electron interactions in the SAM-Au hybrid system are further investigated. The spin-electron interaction was tuned by altering the ligand structure of the molecular complex by depositing a thin Au layer on top of the SAM (Au capping) by magnetron sputtering and e-beam evaporation. It was observed that the Au capping deposited by e-beam evaporation increased the Kondo effect slightly compared to the uncapped case, while capping by magnetron sputtering increased the Kondo effect significantly. It was shown that Au capping by magnetron sputtering, where Au atoms arrive on the SAM surface with high energies change the ligand structure around the core ion and increase its interaction with the surrounding conduction electrons.

In Chapter 6, the electronic properties of graphene sheets that were transferred onto SAMs on SiO_2/Si substrates are investigated. The SAM molecules used in this Chapter involved the same metal containing groups as the complexes that were used in Chapters 4 and 5. It was aimed to investigate the effect of the SAMs on the transport properties of the graphene.

References

[1] IntelPR. (2011, 01-05-2014). Available: http://newsroom.intel.com/docs/DOC-2032

[2] K. Likharev, "Electronics below 10 nm," *Nano and Giga Challenges in Microelectronics,* pp. 27-68, 2003.

[3] L. Newton, T. Slater, N. Clark, and A. Vijayaraghavan, "Self assembled monolayers (SAMs) on metallic surfaces (gold and graphene) for electronic applications," *Journal of Materials Chemistry C,* vol. 1, pp. 376-393, 2013.

[4] S. A. DiBenedetto, A. Facchetti, M. A. Ratner, and T. J. Marks, "Molecular Self-Assembled Monolayers and Multilayers for Organic and Unconventional Inorganic Thin-Film Transistor Applications," *Advanced Materials,* vol. 21, pp. 1407-1433, 2009.

[5] J. C. Love, L. A. Estroff, J. K. Kriebel, R. G. Nuzzo, and G. M. Whitesides, "Self-assembled monolayers of thiolates on metals as a form of nanotechnology," *Chem. Rev.,* vol. 105, pp. 1103-1170, 2005.

[6] J. J. Gooding, F. Mearns, W. Yang, and J. Liu, "Self-Assembled Monolayers into the 21st Century: Recent Advances and Applications," *Electroanalysis,* vol. 15, pp. 81-96, 2003.

[7] B. de Boer, A. Hadipour, M. M. Mandoc, T. van Woudenbergh, and P. W. M. Blom, "Tuning of metal work functions with self-assembled monolayers," *Advanced Materials,* vol. 17, pp. 621-625, Mar 8 2005.

[8] W. Chen, D. Qi, X. Gao, and A. T. S. Wee, "Surface transfer doping of semiconductors," *Progress in Surface Science,* vol. 84, pp. 279-321, Sep-Oct 2009.

[9] E. C. P. Smits, S. G. J. Mathijssen, P. A. van Hal, S. Setayesh, T. C. T. Geuns, K. A. H. A. Mutsaers*, et al.*, "Bottom-up organic integrated circuits," *Nature,* vol. 455, pp. 956-959, Oct 16 2008.

[10] B. Lee, Y. Chen, F. Duerr, D. Mastrogiovanni, E. Garfunkel, E. Y. Andrei*, et al.*, "Modification of Electronic Properties of Graphene with Self-Assembled Monolayers," *Nano Letters,* vol. 10, pp. 2427-2432, Jul 2010.

[11] J. C. Ho, R. Yerushalmi, Z. A. Jacobson, Z. Fan, R. L. Alley, and A. Javey, "Controlled nanoscale doping of semiconductors via molecular monolayers," *Nature Materials,* vol. 7, pp. 62-67, Jan 2008.

[12] W. P. Voorthuijzen, M. D. Yilmaz, W. J. M. Naber, J. Huskens, and W. G. van der Wiel, "Local Doping of Silicon Using Nanoimprint Lithography and Molecular Monolayers," *Advanced Materials,* vol. 23, pp. 1346-1350, Mar 18 2011.

[13] A. K. Geim and K. S. Novoselov, "The rise of graphene," *Nature materials,* vol. 6, pp. 183-191, 03//print 2007.

[14] K. I. Bolotin, K. J. Sikes, J. Hone, H. L. Stormer, and P. Kim, "Temperature-Dependent Transport in Suspended Graphene," *Phys. Rev. Lett.,* vol. 101, p. 096802, 08/25/ 2008.

[15] K. S. Novoselov, A. K. Geim, S. V. Morozov, D. Jiang, Y. Zhang, S. V. Dubonos*, et al.*, "Electric Field Effect in Atomically Thin Carbon Films," *Science,* vol. 306, pp. 666-669, October 22, 2004 2004.

Chapter 2

Background

This chapter gives an introduction to the theoretical concepts used in this work. First, the Kondo effect, which results from the interactions between conduction electrons and localized spins, and how it affects the electrical resistivity of a metallic system is discussed. Next, weak (anti-)localization, the electron interference contribution to resistivity in disordered metals, is explained. Next, crystal field theory explaining the electronic structure and the origin of the spin of the molecular complex is introduced.

2.1 Kondo effect

The Kondo effect is described in detail in several books and review papers [1-3]. Below, a brief description of the effect is presented.

The resistivity of a metal originates from the scattering of conduction electrons via several mechanisms. The scattering events can be categorized in two elementary groups: *elastic scattering* and *inelastic scattering* events. In elastic scattering events, the electron preserves its energy and phase, whereas inelastic scattering events result in a change in the electron's energy and phase. This gives rise to quantum corrections to the conductance, due to interference effects. These effects only occur if the phase is conserved over distances that are long enough to come back to the same position (weak (anti-)localization). Some examples of scattering events are electron-defect scattering, electron-electron scattering and electron-phonon scattering. Elastic electron-defect scattering is the scattering of conduction electrons from crystal defects, which can be in the form of a lattice site vacancy, a static lattice defect in an otherwise perfect crystal lattice, or an impurity atom. Inelastic electron-electron scattering occurs between electrons that take part in conduction and has a T^2 temperature dependence, but this contribution is often negligible at higher temperatures, since it is overshadowed by other scattering mechanisms such as electron-phonon scattering. Inelastic electron-phonon scattering occurs due to scattering of conduction electrons from phonon excitations and it has a T^5 temperature dependence. With these, the resistivity of a piece of metal $\rho\ (T)$ can be approximated as

$$\rho(T) = AT^5 + \rho_0\ , \tag{2.1}$$

where the first and the second term are the contribution from electron-phonon scattering and the electron-defect scattering, respectively.

As the temperature is lowered, the resistivity drops since the energy and the number of phonons that the conduction electrons can scatter off decreases. At low enough temperatures, all the phonons freeze while the number of defects and impurities remain the same. Therefore the resistivity reaches a saturation value (ρ_0), which is determined by the purity of the metal and the number of

defects in the metal. The addition of impurities to a metal is predicted to move the *ρ (T)* curve upwards but not to alter its shape [2].

However, in 1934, it was observed that the resistivity of Au as a function of temperature showed an anomalous increase below ~4K instead of saturation [4]. Later, similar resistivity behavior was observed for other metals as well. This indicated that there must be an additional scattering mechanism to cause the increase in resistivity (resistivity upturn) at low temperatures. The origin of this behavior remained unexplained until 1964, when the Japanese theorist Jun Kondo was able to provide an explanation [3], and the phenomenon is named after him as the Kondo effect. In his paper, he discussed the experimental work on the resistivity of the dilute alloys of Fe (one atomic percent) with the series of NbMo alloys as host metals [5], dilute Cu alloys [6] and dilute AuFe alloys [7].

Kondo attributed the increase in the resistance to the higher order scattering processes involving dilute magnetic impurities and the conduction electrons in the host metal. During this interaction, the spin of the localized electron on the impurity (localized magnetic moment) and the spins of the interacting conduction electrons are exchanged and the conduction electrons are spin scattered [8]. Since many electrons need to be involved in the process, the Kondo effect is a many-body phenomenon [9]. The Anderson impurity model, together with numerical renormalization group theory, provided important contributions to understanding the physics of the Kondo effect [10, 11].

Anderson assumed in his impurity model that the localized electron on a magnetic impurity atom (e.g. Co) inside a metal (e.g. Au) has a net magnetic moment [10]. In this model, he also described the interaction of this moment with the surrounding conduction electrons in the metal, as depicted in figure 2.1.a

The impurity is assumed to have only one electron level with energy "ε_o" which is below the Fermi level [9]. The level is filled with a spin ½ electron as either "spin up" or "spin down". Adding a second electron into this orbital requires an additional Coulomb charging energy (U) and removing the electron in the impurity level costs the excitation energy of ε_o. Therefore, the orbital will be singly occupied and the spin of the electron will result in a net magnetic moment. This regime is called the "local moment regime". Classically, the impurity electron

is trapped in the ε_o level, however quantum mechanically, it can tunnel out of the impurity site to a "virtual state" (or "intermediate state") for a very short time, leaving an empty impurity level. In order to satisfy energy conservation, an electron from the Fermi sea must tunnel into the empty impurity level. If the replacing electron has an opposite spin, the spin of the impurity in the final state will be flipped.

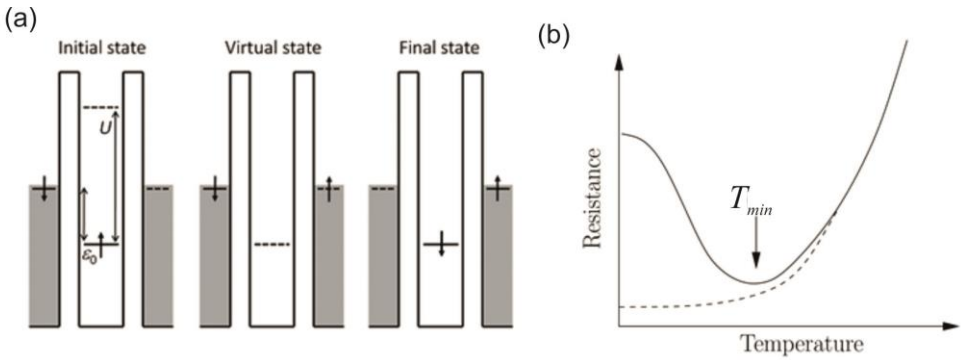

Figure 2.1. (a) Schematic of Anderson impurity model describing the spin flip of the localized spin ½ moment with the conduction electrons in the Fermi sea via a virtual state. (b)Temperature behavior of resistivity in metals with dilute magnetic impurities (solid line) and pure metals (dashed line) [10].

Another type of spin flip process is also possible where the order of tunneling out and tunneling in the impurity level is interchanged. In this case, first, an electron will tunnel into the impurity orbital (electron creation in the intermediate state) and the impurity will be doubly occupied in the intermediate state. If the electron with the original spin direction tunnels out the impurity (electron annihilation in the intermediate state), the spin of the impurity will be flipped [1]. The Kondo effect is the quantum coherent combination of many such tunneling events back-and forth, resulting in spin exchange interaction between the impurity spin and the conduction electron spins, and therefore spin scattering of the conduction electrons [9]. It reveals itself as a logarithmic resistivity increase at low temperatures as shown in figure 2.1.b.

Kondo recalculated the resistivity by modifying Anderson's impurity model. He worked on the case in which the magnetic impurity concentration is so low that they are not interacting with each other and act as single impurities in a Fermi sea. The modification he made was to add higher order corrections to the calculation using perturbation theory which is an iterative process in which the equation is usually written as a series of smaller and smaller terms [2, 3]. In the second order perturbation, he took into account that the order of creation and annihilation of a conduction electron from the Fermi sea (first annihilation or first creation) gives a different result. Spin scattering involving a doubly occupied intermediate state or empty intermediate state also gives a different result. Due to this, the occupation number of the intermediate state influences the scattering processes. The occupation number is related to the Fermi-Dirac function, which gives rise to a -ln$T$ dependence of resistivity. The minus sign of the -ln$T$ term results from the negative sign of the antiferromagnetic impurity spin-electron spin interaction, leading to an increasing resistivity with decreasing temperature figure 2.1.b. The resistivity increase ($\Delta\rho$) is described as:

$$\Delta\rho = -\beta\, ln(T) \qquad 2.2)$$

where β is a parameter which is dependent on the host metal and the impurity species and concentration.

Kondo's calculation for resistivity for dilute magnetic impurities was in good agreement with the experimental data at low temperatures. However, it becomes problematic when the temperature approaches zero since the -ln$T$ term diverges giving rise to infinite resistivity, which is unphysical. This failure of the Kondo theory in explaining the resistivity at extremely low temperatures got known as the "Kondo problem" and the temperature below which the Kondo theory starts to fail is known as the "*Kondo temperature* (T_K)".

Costi and Hewson [11] provided a solution to the Kondo problem by using the scaling approach of Anderson [12], and adapting the numerical renormalization group (NRG) approach of Wilson [13]. They showed that the normalized resistivity below and above the T_K falls on top of a universal curve, which can be given with the expression (which will be also used in Chapters 4 and 5 of this thesis. See also figure 4.2.c):

$$\rho/\rho_0 = f(T/T_K) \tag{2.3}$$

Here, ρ_0 is the resistivity value at absolute zero and $f(T/T_K)$ is the same temperature-dependent function for all materials that contain spin-1/2 impurities. So the parameters that characterize the Anderson impurity model, U, ε_0 and Γ, can be replaced by a single parameter, T_K [9]. T_K was related to the parameters of the Anderson model by

$$T_K = \frac{1}{2}\sqrt{\Gamma U}\, e^{[(\pi\varepsilon_0\,(\varepsilon_0+U))/\Gamma U]} \tag{2.4}$$

where U is the Coulomb repulsion energy between two electrons at the site of the impurity and Γ is the width of the impurity level which is broadened by electrons tunneling to and from it.

The situation for temperatures lower than T_K can be explained in the context of Kondo cloud formation. As explained earlier, the Kondo effect is the combination of many spin scattering events. These scattering events result in the formation of a many-body spin-singlet state. At temperatures where this singlet state starts to develop, the resistivity rises with a ln$T$ temperature dependence. Well below the T_K, the conduction electrons surrounding the impurity are paired with the impurity electrons and fully screen the impurity spin. The screening of the local magnetic moment by a cloud of conduction electrons compensate its magnetic moment. After this point, the impurity spin no longer behaves as a magnetic scattering entity for further conduction electrons and transferred into an overall non-magnetic state [8, 14]. This phenomena is named as the "*Kondo screening"* and the cloud of conduction electrons responsible of the screening is named as the *"Kondo cloud"*. The spatial extension of the Kondo cloud is characterized by the Kondo length (ξ_K) [15].

$$\xi_K = \frac{\hbar v_F}{k_B T_K} \tag{2.5}$$

where $\hbar$ is the reduced Planck constant, v_F is the Fermi velocity and k_B is the Boltzmann constant. However, the experimental observation of the Kondo cloud has proven to be very difficult. The saturated resistivity after the formation of the singlet state is referred to as the "unitary limit". Van der Wiel *et al.* showed this limit in electron transport measurements through a quantum dot [16].

The T_K is an important indication of the Kondo coupling strength of conduction electrons and the impurity electron. It should be noted that T_K is not a sharp or distinct transition temperature, but is rather a characteristic temperature centered with a broad region in T [14].

The total resistivity including residual resistivity, phonon contribution and Kondo-magnetic contribution the resistivity takes the form:

$$\rho\,(T) = \; aT^5 \; + c\rho_0 - c\,\rho_1 ln\left(\frac{T}{T_K}\right) \qquad 2.6)$$

where c is the impurity concentration. This expression exhibits a minimum at finite temperatures ($d\rho/dT=0$):

$$T_{min} = \left(\frac{\rho_1}{5a}\right)^{1/5} c^{1/5} \qquad (2.7)$$

As a result, T_{min} has a dependence on the magnetic ions concentration in the order of $c^{1/5}$.

An effective way of investigating the Kondo effect is investigation of temperature dependence of electrical resistivity. As described earlier, at very high temperatures the resistivity decreases with T^5 dependence and reach to a minimum. At lower temperatures the resistivity shows two regions for $T >> T_K$ and $T << T_K$. In the first region, the resistivity increases with the logarithm of the temperature ($\rho(T) \sim -\ln T$) and in the second region the resistivity saturates to the so-called "unitary limit" as $T \rightarrow 0$ K. Around $T \approx T_K$, the Kondo contribution to the resistivity is non-analytical and characterizes the transition from region of strong correlation with the magnetic ions ($T << T_K$) to the region of weak or negligible correlation ($T >> T_K$) [14].

As stated in the beginning of the chapter, the Kondo effect occurs in the presence of isolated magnetic impurities, meaning the concentration of magnetic impurities is very low. However, if the impurity concentration increases, in addition to the inelastic scattering between the impurity and the conduction electrons, a different phenomenon appears. It is the conduction-electron-mediated interaction between different magnetic impurities, the so-called the RKKY (or Ruderman–Kittel–Katsuya–Yoshida) interaction. RKYY interaction occurs because a magnetic moment on one impurity site polarizes the conduction

electrons, which propagate the polarization to another impurity site [2]. When this happens, the spins of the localized magnetic moments are locked and therefore spin flip events are blocked, resulting in the suppression of the Kondo effect. The RKKY interaction dies out as the separation between the impurities increases. Therefore the competition and transition between the Kondo and RKKY regime can be studied by changing the separation of the magnetic impurities, in other words, changing the impurity concentration. In order to investigate this, a precise control over the concentration of isolated magnetic impurities is required. Such an investigation can provide clues about the Kondo length.

In this thesis work, as discussed in Chapter 4, we studied the Kondo effect as a result of inserting isolated magnetic impurities from a SAM of metal-organic complexes. We observed that the Kondo upturn in resistivity increases with increasing concentration of the magnetic impurities. In the concentration regime that we studied, the resistivity remained in the logarithmic increase region and no indication of RKKY interaction was observed. In Chapter 5, we were able to tune the Kondo effect by increasing the strength of the electron-impurity interaction by destructing the ligand structure around the magnetic ion.

2.2 Weak (anti-) localization

The Kondo effect is a quantum correction to the resistivity due to spin flip scattering events. Another correction to the resistivity that should be taken into account in the quantum diffusive transport regime is weak (anti-)localization. In Chapters 4 and 5 experiments where the Kondo effect and weak anti-localization play an important role are presented.

Weak localization is a phenomenon arising from phase coherent electron interference in disordered metals with small or absent spin-orbit coupling. It results in an increase in resistivity at low magnetic fields.

Resistivity is related to the probability of an electron to reach from one point to another in a conducting medium. During travelling from one point to another, the electron participates into various scattering effects. In elastic scattering events, the electron preserves its energy and phase. However in

inelastic scattering events, the electron changes its energy and loses or "forgets" its phase. The time and distance between two elastic scattering events are named as elastic scattering time (τ) and elastic mean free path (l), respectively. Similarly, the time and the distance that the electron loses its phase are called as phase coherence time (τ_φ) and phase coherence length (l_φ). The electron is able to scatter elastically a number of times before losing its phase memory, if elastic scattering events are more frequent than inelastic scattering events. This happens when the elastic scattering time is smaller than phase coherence time ($\tau << \tau_\varphi$) and accordingly elastic mean free path is smaller than the phase coherence length is ($l << l_\varphi$). If the scattering path is a closed loop with time-reversal symmetry, i.e. starting and ending at the same point, constructive interference leading to backscattering of the electron can occur. This results in an increase in the resistivity at small or absent magnetic field, known as *weak localization* (WL) [17].

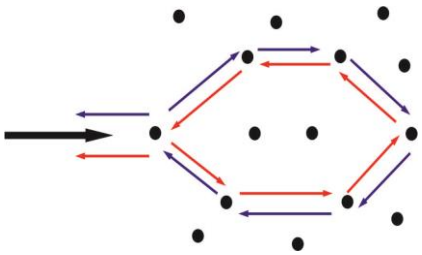

Figure 2.2. Time-reversed paths in a diffusive sample. At zero magnetic field the interference of such paths is always constructive.

Figure 2.2 depicts an example of two time reversed paths. If an electron scatters in the closed path as indicated by blue arrows after the injection (black arrow), then quantum mechanically the partial wave of this electron has the same probability to scatter in such a way that it takes the time-reversed path and comes back to its origin, thus enclosing a loop as in the red path.

Classically, the electron is a point particle and the probability of the electron to return to its original place is $|A_1|^2+|A_2|^2=2A^2$, where A_1 and A_2 are the amplitudes of the wave functions of the time reversed paths and when there is time reversal symmetry, $A_1 = A_2 = A$. Quantum mechanically the wave like behavior

of the electron is also taken into consideration and the probability is $|A_1+A_2|^2=|A_1|^2+|A_2|^2+2|A_1\,A_2|=4A^2$. The probability of the electron to be present at the end point is doubled owing to the $2|A_1\,A_2|$term, which can also be referred as the interference term. This term indicates that the electron interferes with itself constructively and the probability of finding the electron at the end point increases (tendency of the electron to 'localize' increases). This translates into enhanced backscattering (coherent backscattering) as a result of constructive interference. This results in a decreased probability of transmission, therefore increase in resistivity. Due to this phenomena, a quantum correction to resistivity is required, also known as *weak localization* [18]. It is observed as a peak in resistivity at low magnetic fields as shown figure 2.3.a for a thin Cu film.

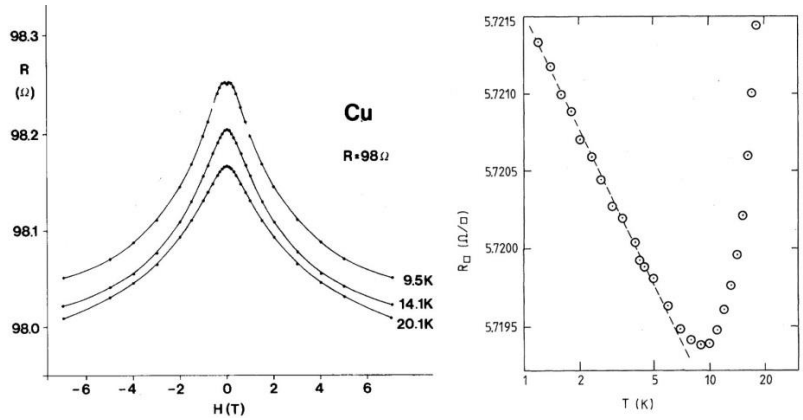

Figure 2.3. (a) WL effect in thin Cu film at different temperatures (modified from [20]) (b)Temperature dependence of Cu film resistivity [19].

At low temperatures, the phonons freeze increasing the inelastic scattering time and as a result, the phase coherence time overcomes the elastic scattering time [17]. The dependence of coherence time to temperature makes weak localization to be temperature dependent starting at a certain temperature satisfying $\tau << \tau_\varphi$ as illustrated in figure 2.3.b for Cu thin films. It can be seen that the resistivity of the sample increases as sample is cooled down below 10K [19].

It is important to note that the resistivity increase at low magnetic fields due to WL is observed for the systems with small or absent spin-orbit coupling (SOC). If on the other hand, the metal film includes atoms with large spin-orbit coupling such as Au, a decrease in resistance is observed instead of the increase, which is named as *weak anti-localization* (WAL).

SOC is the interaction of a particle's spin with its motion. The electric field produced by the nuclei results in a magnetic field in the rest frame of the electrons moving through the lattice with velocity v. This magnetic field interacts with the electron's spin magnetic moment (μ), which causes the spin to rotate. As the partial waves travel along self-intersecting paths in a closed loop, the spin is rotated under the influence of the SOC. The time scale that describes the randomization of the spin direction in time due to SOC is "τ_{SO}". For times $t>>\tau_{SO}$, the spin orientation is completely randomized.

When the SOC is weak, ($\tau_{SO} >> \tau_{\varphi}$) the spin remains polarized in the same direction throughout the closed loop and the backscattering is enhanced, leading to WL. On the other hand, when strong SOC is present ($\tau_{SO} << \tau_{\varphi}$), the spin of the electron rotates and completely randomized as it goes around a self-intersecting path. However, on the time-reversed path, the spin experiences a rotation in exactly the opposite direction. If the interference terms are averaged over many pairs of time-reversed paths, it is found the two paths interfere *destructively* which *lowers* net resistivity, leading to WAL (figure 2.4.a).

The electric field intensity produced by the nuclei (E) strongly depends on the charge of the nucleus (the atomic number Z). Therefore, the effect of the spin-orbit interaction is more pronounced in materials containing heavy atoms like Au [17]. As observed in figure 2.4.b, the pure Mg film shows weak localization peak (the bottom curve), whereas after addition of Au (with strong SOC) on top of the film, it starts to show weak anti-localization dips instead (top five curves). It can be seen that the depth of the WAL curves increase with increasing Au thickness due to increasing spin-orbit coupling in the film [18].

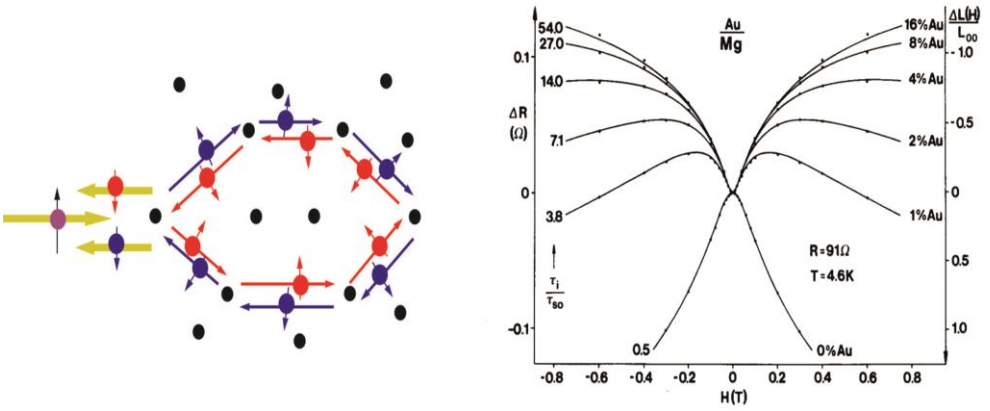

Figure 2.4. (a) Schematic of the weak-anti localization mechanism when strong spin orbit coupling exists. (b) The magneto-resistance of an Mg thin film measured at 4.5K for different coverages of Au on top of Mg [20].

An electron moving along a loop-like path in a perpendicular magnetic field gains an additional phase. The phase shift of an electron propagating for time t is given by:

$$\varphi = 2\pi\,(BS/\phi_0) = 2\pi\,(BDt/\phi_0)\ ,\ \text{for } t < \tau_\varphi \qquad (2.8)$$

where B is the magnitude of the magnetic field, S is the area enclosed by the trajectories, ϕ_0 is the magnetic flux quantum and D is the diffusion constant. The probability of the electron to return to its original place under the external magnetic field is modified to be:

$$|A_1+A_2|^2 = |A_1|^2 + |A_2|^2 + 2|A_1||A_2|\cos(\varphi) \qquad (2.9)$$

When B=0, $\cos(\varphi)$ =1 and the weak localization has its maximum value. For large fields, the phase factor will be large and the probability of returning to the origin will get smaller suppressing the interference at the origin point. Therefore, an external perpendicular magnetic field has a suppressing effect on both weak localization and weak anti-localization.The minimum magnetic field needed to suppress the coherent backscattering is the critical magnetic field (B_φ). If it is assumed that the interference starts to break down at φ = 1 at t = τ_φ , then the B_φ can be estimated as $B_\varphi \approx h/eD\,\tau_\varphi$.

For both WL and WAL, l_φ determines the FWHM of the magnetoresistance curves on a field scale of $B_\varphi = \phi_0/l_\varphi^2$ around zero field. For a homogeneous film thinner than l_φ, the phase coherence length can be estimated as $l_\varphi = \sqrt{D\,\tau_\varphi} \approx \sqrt{h/eB_\varphi}$. The spin-orbit length l_{SO} introduces an additional field scale $B_{so}=\varphi_0/\ l_{SO}^2$ which marks the turnover from weak antilocalization to weak localization. If phase coherence is destroyed by e.g. increasing temperature, the peaks smoothen out and the localization effects disappear.

Another quantum correction to the resistivity caused by interference is the electron-electron interaction (Aronov–Altshuler effect). WL is caused by an electron interfering with itself. Interference can also occur between different electrons if they meet twice, resulting in the electron-electron interaction. Electron-electron interaction gives a very similar negative conductivity correction as weak localization. The details can be found in [17]. Although it is very hard to distinguish conductivity contributions from electron-electron interaction and weak localization, WAL can be easily seperated due to its opposite sign, as will be seen in Chapter 4.

In Chapter 4 of this thesis work, weak anti-localization was observed in thin Au films doped by a SAM of metal complexes. The WAL analysis was used as an independent way to verify the molecular spin doping of the thin Au film by the metal complexes.

2.3 Crystal field theory

As mentioned earlier, in order to investigate the interaction of localized spin and conduction electron spin, the transition metal complex [Co(tpy)(tpy-SH)]$^{2+}$ is used to insert isolated magnetic moments inside thin Au films. Here, the (tpy) stands for the terpyridine ligand: 4'-(5-ercaptopentyl)-2,2':6',2"-terpyridinyl and (tpy-SH) is the thiol-modified version of the same ligand to enable chemisorption on Au surfaces. The origin of the spin in the complex (the unpaired electron) can be described by the crystal field theory (CFT) [21].

CFT describes the electronic structure of transition metal complexes such as [Co(tpy)(tpy-SH)]$^{2+}$. It relies on the breaking of orbital degeneracy in the d and f

orbitals of transition metal complexes due to the presence of the ligands. The term 'ligand' is used for a negatively charged ion, molecule, or functional group that binds to another chemical entity to form a larger complex. CFT qualitatively describes the strength of the bonds formed between the metal ion and the ligand. Depending on the metal-ligand bonds, the energy of the system is changed. Change in the chemical bonds may alter the magnetic properties of the molecule-metal system, as will be shown in Chapter 5. The change in energy of the system depends on the number of ligands interacting with the metal ion and the geometry of the molecule. Here, only the octahedral geometry, which is the case in the $[Co(tpy)(tpy\text{-}SH)]^{2+}$ complex (albeit distorted, see figure 2.5.b) will be considered.

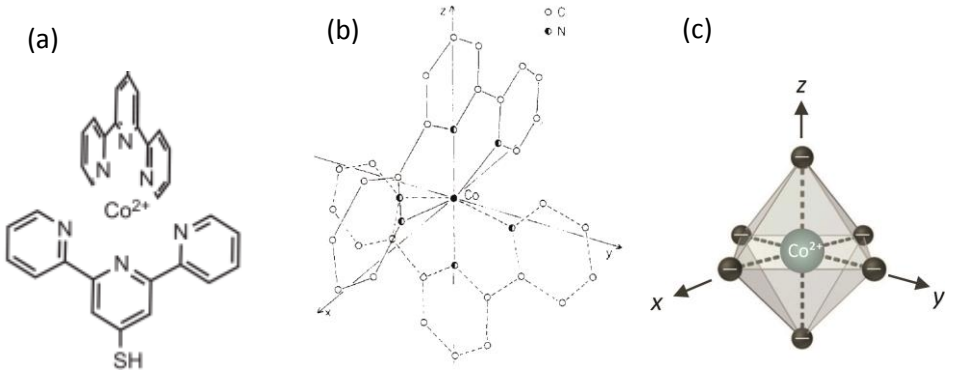

Figure 2.5. (a) representation of $[Co(tpy)(tpy\text{-}SH)]^{2+}$ complex. (b) the molecular geometry of the complex [22]. (c) the ligands are represented as point charges located on the vertices of an octahedron [23].

$[Co(tpy)(tpy\text{-}SH)]^{2+}$ complex consists of six ligands (carbon rings with a nitrogen atom) that are bonded to the central Co^{2+} ion in approximate octahedral geometry as shown is figure 2.5.a and figure 2.5.b. The ligands can be considered as six negative charges placed around the Co^{2+} ion on the vertices of an octahedron (figure 2.5.c). As shown figure 2.6, all of the d orbitals have four lobes of electron density, except for the d_{z^2} orbital, which has two opposing lobes and a doughnut of electron density around the middle. The d orbitals can be divided into two smaller sets, e_g and t_{2g} states, as discussed below.

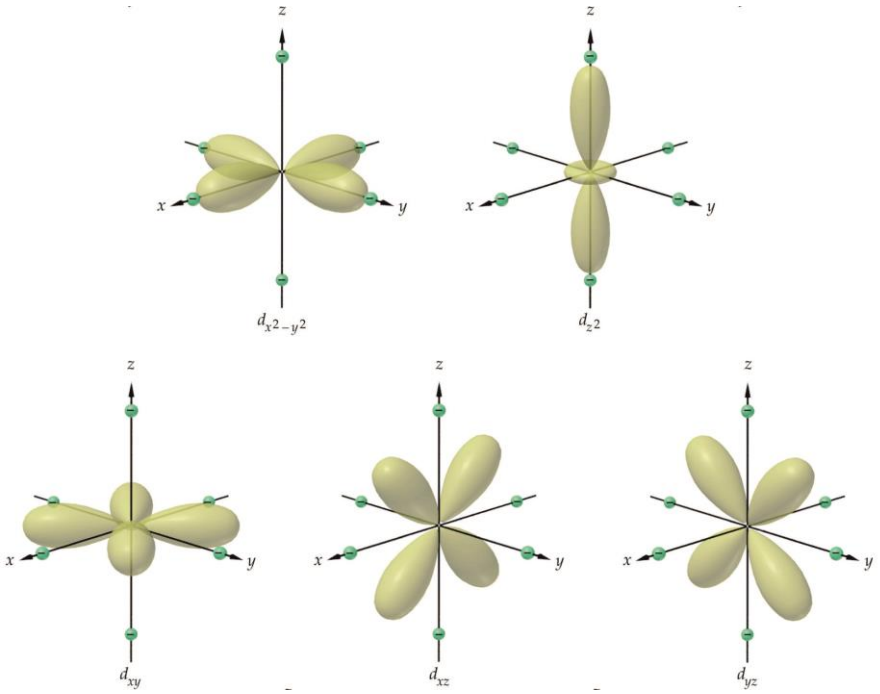

Figure 2.6. The shapes of the five d orbitals (in yellow) and their orientation with respect to an octahedral array of negatively charged ligands (green points). The lobes of the orbitals indicate the regions of space where a d electron is most likely to be found [24].

The electrons in the metal d-orbitals and those in the ligands repel each other due to the repulsion between like charges. For a spherical distribution of charges where the charges are distributed uniformly over the surface of a sphere around the metal ion, the repulsion is experienced uniformly by all orbital electrons, therefore all energy levels rise equally (figure 2.7). However, for non-spherical distribution of charges, as is the case for the d-orbitals, not all d-electrons feel the same repulsion. As described, in the $[Co(tpy)(tpy\text{-}SH)]^{2+}$ complex, the six ligands are located on the x, y, and z axes. Since the d_{z^2} and $d_{x^2-y^2}$ orbitals point directly towards the ligands in these axes, electrons in these orbitals experience greater repulsion. It requires more energy to have an electron in these orbitals than it would to put an electron in one of the other orbitals. The energy of these two orbitals (forming the doubly degenerate e_g level) will be lifted up compared to that of a spherically distributed orbital. In contrast, the other

three d orbitals are all oriented at a 45° angle to the coordinate axes, so they point between the six negative charges. The energy of an electron in any of these three orbitals is lower than the energy for a spherical distribution of negative charge since it would experience less repulsion. The lowered d_{xy}, d_{xz}, and d_{yz} orbitals form the triply degenerate t_{2g} level. Consequently, the d orbital level splits into two levels due to the electrostatic environment: e_g and t_{2g} levels. This splitting in d orbital levels due to the presence of the ligands is called the *crystal field splitting*. The energy between the two levels is referred to as the *energy splitting parameter* and denoted by Δ_o or *10Dq*. The e_g orbital is $0.6\Delta_o$ (or 6Dq) higher and the t_{2g} orbital is $0.4\Delta_o$ (or 4Dq) lower than the spherical distribution level.

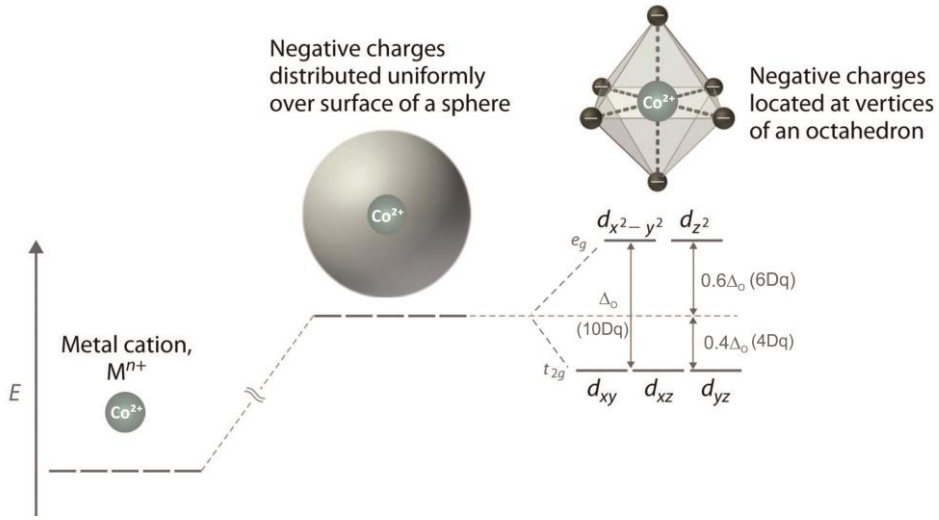

Figure 2.7. Energy level of the d orbital of an isolated Co^{2+} ion (left). The energy of all five d orbitals increases due to electrostatic repulsions when a charge of −6 is distributed over a spherical surface surrounding a metal ion. Uniform distribution causes the five d orbitals to remain degenerate (middle). Placing a charge of −1 at each vertex of an octahedron causes the d orbitals to split into two groups with different energies. The average energy of the five d orbitals is the same as for a spherical distribution of a −6 charge (right) [23].

The electronic configuration of a neutral Co atom is [Ar] $3d^7 4s^2$, therefore the Co^{2+} ion has 7 electrons on the d orbital. The first three electrons fill the t_{2g}

orbitals, with their spins aligned. The fourth electron can either fill one of the orbitals in e_g level, which lies Δ_o higher in energy, or occupy a t_{2g} orbital but with opposite spin (see figure 2.8). The latter requires the *exchange energy (J)*. If the $J < \Delta_o$, first the t_{2g} orbitals will be filled by electrons with opposite spin whereas, if $\Delta_o < J$, the electrons start filling the e_g levels with the same spin. The latter situation is observed for small Δ_o values and results in a larger number of electrons with the same spin, and is therefore referred to as the *high spin state*. Ligands that cause a transition metal ion to have a small crystal field splitting, which leads to high spin, are called *weak-field ligands*. The Δ_o value depends on the on the specific ligands, the metal ion, the oxidation state of the metal ion and the distance between the ligands and the metal ion. In literature, the $[Co(tpy)(tpy\text{-}SH)]^{2+}$ is given to be in the low-spin state [22].

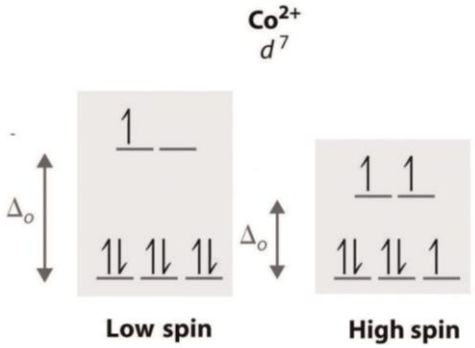

Figure 2.8. High spin and low spin configurations of Co^{2+} and Co^{3+} ion. In literature, the $[Co(tpy)(tpy\text{-}SH)]^{2+}$ complex is given to be in the low-spin state [23].

References

[1] A. C. Hewson, *The Kondo problem to heavy fermions*: Cambridge university press, 1997.

[2] P. L. Taylor and O. Heinonen, "A Quantum Approach to Condensed Matter Physics," ed: Taylor & Francis, 2003.

[3] J. Kondo, "Resistance minimum in dilute magnetic alloys," *Prog. Theor. Phys.,* vol. 32, pp. 37-49, 1964.

[4] W. De Haas, J. De Boer, and G. Van den Berg, "The electrical resistance of gold, copper and lead at low temperatures," *Physica,* vol. 1, pp. 1115-1124, 1934.

[5] M. Sarachik, E. Corenzwit, and L. Longinotti, "Resistivity of Mo-Nb and Mo-Re Alloys Containing 1% Fe," *Phys. Rev.,* vol. 135, p. A1041, 1964.
[6] W. B. Pearson, *Phil. Mag.,* vol. 46, p. 920, 1955.
[7] B. Knook, PhD, University of Leiden, 1962.
[8] D. J. Goldhaber-Gordon, "The Kondo effect in a single-electron transistor," PhD, Department of Physics, Massachusetts Institute of Technology. , 1999.
[9] L. Kouwenhoven and L. Glazman, "Revival of the Kondo effect," *Physics world,* vol. 14, pp. 33-38, 2001.
[10] P. W. Anderson, "Localized magnetic states in metals," *Phys. Rev.,* vol. 124, p. 41, 1961.
[11] T. Costi, A. Hewson, and V. Zlatic, "Transport coefficients of the Anderson model via the numerical renormalization group," *Journal of Physics: Condensed Matter,* vol. 6, p. 2519, 1994.
[12] P. Anderson, "A poor man's derivation of scaling laws for the Kondo problem," *Journal of Physics C: Solid State Physics,* vol. 3, p. 2436, 1970.
[13] K. G. Wilson, "The renormalization group: Critical phenomena and the Kondo problem," *Rev. Mod. Phys.,* vol. 47, p. 773, 1975.
[14] Z. Guo, "Electrotransport Studies of the Anomalous Semimetal Ground State in CeRu4Sn6," University of Johannesburg, 2005.
[15] I. Affleck, "The Kondo screening cloud: what it is and how to observe it," *ArXiv.org,* vol. 0911.2209v2, 2010.
[16] W. Van der Wiel, S. De Franceschi, T. Fujisawa, J. Elzerman, S. Tarucha, and L. Kouwenhoven, "The Kondo effect in the unitary limit," *Science,* vol. 289, pp. 2105-2108, 2000.
[17] V. F. Gantmakher and L. I. Man, *Electrons and disorder in solids*: Oxford University Press, 2005.
[18] T. Ihn, "Semiconductor Nanostructures: Quantum states and electronic transport ", ed: Oxford University Press, 2010.
[19] L. Van den dries, C. Van Haesendonck, Y. Bruynseraede, and G. Deutscher, "Two-Dimensional Localization in Thin Copper Films," *Phys. Rev. Lett.,* vol. 46, pp. 565-568, 02/23/ 1981.
[20] G. Bergmann, *Physics Reports* vol. 107, p. 1, 1984.
[21] J. Van Vleck, "Theory of the variations in paramagnetic anisotropy among different salts of the iron group," *Phys. Rev.,* vol. 41, p. 208, 1932.
[22] S. Kremer, W. Henke, and D. Reinen, "High-spin-low-spin equilibriums of cobalt (2+) in the terpyridine complexes Co (terpy) 2X2. nH2O," *Inorg. Chem.,* vol. 21, pp. 3013-3022, 1982.
[23] B. Averill and P. Eldredge, "General chemistry: principles, patterns, and applications," 2011.
[24] R. C. F. John McMurry, *Chemistry*: Prentice Hall, 2003.

Chapter 3

Experimental Methods

In this chapter, the experimental methods used for sample preparation and measurements are presented. The chapter consists of five sections. In the first section, preparation of self-assembled monolayers is described. In the second section, Au deposition methods and deposition conditions are given. In the third section, low-temperature electrical and magnetic characterization systems and measurements are explained. In the fourth section, synchrotron radiation techniques and data acquisition are described and finally in the last section, the surface-enhanced Raman spectroscopy method is described.

3.1 Preparation of self-assembled monolayers

As mentioned in Chapter 1, self-assembled monolayers (SAMs) are 1-molecule thick films formed on a surface by spontaneous adsorption. In this study, SAMs were used as a carrier medium for magnetic impurities to be inserted in a metallic thin film resulting in a controlled magnetic doping method and a model system to investigate conduction electron spin-localized spin interaction. In order to dope thin Au films (Chapters 4 and 5) and graphene (Chapter 6) with isolated impurities, we use a SAM of metal-terpyridine complexes, containing a metal ion with an unpaired spin (magnetic moment). The metal ion was coordinated in a distorted octahedral manner by two perpendicularly positioned terpyridine (tpy) ligands.

In Chapter 3, we will discuss the case where the metal core of the metal ion containing group is either a Co^{2+} ion (Co complex: Co(tpy)(tpy-SH)) or a Zn^{2+} ion (Zn complex: Zn (tpy)(tpy-SH)). Since Co^{2+} carries a net spin (spin 1/2), but Zn^{2+} is spin free, the Co complex acted as the magnetic (spin) dopant and the Zn complex was used to dilute the magnetic dopant concentration in the film. One of the ligands in the molecules was attached to a thiol (SH) group, which allowed them to form a monolayer on a gold surface. The complexes were synthesized according to procedures in the literature by Mahmut Deniz Yilmaz of the Molecular Nanofabrication (MnF), University of Twente [1]. By cyclic voltammetry, it was confirmed that Co^{2+} ions in the complex can be oxidized to zero-spin Co^{3+} at relatively low energy (~0.25 eV). Figure 3.1 illustrates the complexes with SH end group.

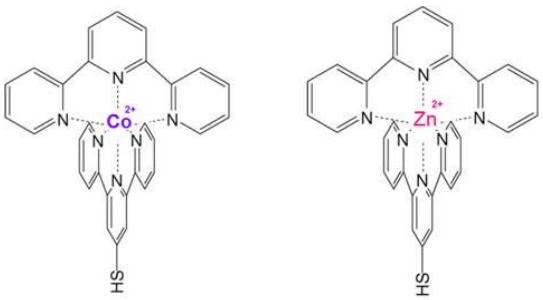

Figure 3.1 Schematics of Co complex: Co(tpy)(tpy-SH) and Zn complex: Zn(tpy)(tpy-SH)

Thin Au films on Si/SiO_2(300nm) (2.2 mm x 6.8 mm) were used as substrates. The details of the Au thin film preparation are described in section 3.2. 0.1 mM acetonitrile solutions of a mixture of the Co and Zn complexes with Co:Zn ratios of 1:0, 2:1, 1:1, 1:3 and 0:1 were prepared and the substrates were immersed inside the solutions overnight at room temperature. The substrates were subsequently rinsed in acetonitrile to remove excess of compounds, and dried in a nitrogen stream. As the molecular complexes are identical (in outer ligand structure, overall charge, size and shape) except for their core metal ion, the same adsorption rate, footprint and affinity for the gold substrate were expected for both species. We therefore anticipated a homogeneously mixed monolayer on top of the gold film, reflecting the Co:Zn ratio of the mixed donor solution. The assumption was verified via x-ray photoemission studies, which will be explained in section 3.4. After formation of the molecular layer, a gold capping layer was sputtered immediately (details in the next section).

It should be noted that the perpendicular arrangement of the tpy-ligands in the Co and Zn complexes and the lack of strong intermolecular interactions prevent the formation of a highly ordered (lattice-like) monolayer.

In Chapter 5, we will discuss about the effect of Au deposition over the Co complexes. The assembling method was exactly the same, only the solution concentration was 1 mM in this case. The Au deposition had noticeable effects on the strength of the interaction between the Au electrons and the localized impurity.

In Chapter 6, we consider the situation where a graphene flake was transferred on top molecules with the same metal ion-ligand groups, but different anchoring groups to investigate the monolayer-graphene interaction. In order to be able to apply gate voltages to the graphene, the monolayers were assembled on Si/SiO_2(300nm) substrates. Since the substrate surface was SiO_2 in this case, a modified version of the complexes; Bis-[4'-(5-aminopentyloxy)-2,2',6',2"terpyridine] cobalt(II) complex and Bis-[4'-(5-aminopentyloxy)-2,2',6',2"terpyridine] zinc(II) complex (NH_2-Co-BisTpy and NH_2-Zn-BisTpy) was synthesized by Richard Egberink from the MnF Group, University of Twente and the assembling conditions were optimized together with Carlo Nicosia from the same group.

The assembling procedure consisted of three steps:

1. The substrates were oxidized with piranha solution for 45 min (concentrated H_2SO_4 and 33 % aqueous H_2O_2 in 2:1 ratio) and rinsed with MilliQ water. After drying with nitrogen flow, the samples were immediately transferred into a vacuum desiccator to form a silanized monolayer by overnight vapor deposition of TPEDA (N-([3-(trimethoxysilyl) propyl]ethylenediamine). Two containers with 150µm TPEDA were inserted in the desiccator. After the silanization, to remove the excess silane, the substrates were rinsed, sonicated for 1-2 min and washed individually with ethanol and dried with nitrogen flow.

2. The resulting amine-terminated monolayers were immersed in 0.05M solution of p-Phenylene diisothiocyanate (DITC) (480 mg in 50 mL ethanol) for 2 hrs at 55^{o}C in Ar atmosphere. After the reaction, the samples were rinsed, sonicated, rinsed again with ethanol and dried in a flow of nitrogen.

3. The DITC-terminated monolayer was functionalized with 2mM (NH_2-Co-BisTpy) complex (51 mg, m.w.= 845.85 g/mol) or (NH_2-Zn-BisTpy) complex (48 mg, m.w.=851 g/mol) or a 1:1 mixture of (NH_2-Co-BisTpy) and (NH_2-Zn-BisTpy) complex (25.5mg:24 mg) in 30 mL ethanol for 2h at 55^{o}C in Ar atmosphere. After the reaction, the samples were rinsed with ethanol and dried with nitrogen flow.

After each step, a contact-angle measurement and X-ray photoemission measurements was performed to verify the surface modification.

After the monolayer formation, the samples were sent to University of Exeter, UK in vacuum sealed packages. Matt Barnes and Gareth Jones transferred the graphene flakes over the monolayers and patterned the graphene devices. Details can be found in Chapter 6.

3.2 Magnetron sputtering and e-beam evaporation methods

3.2.1 Magnetron sputtering

In this thesis, magnetron sputtering together with e-beam evaporation (will be explained in the next section) were used to deposit thin Au films.

Magnetron sputtering is a widely used deposition technique, which uses a combination of electric and magnetic fields to create and confine an Ar plasma close to a target material that is to be deposited. Its operation principle is illustrated in figure 3.2. A low pressure of neutral Ar gas is released into the deposition chamber. A plasma is ignited by applying a strong electric field, which accelerates charged particles that are naturally present, causing an avalanche of ionization events. By suitable application of a magnetic field, the electrons in the plasma are deflected to stay near the target surface. By an appropriate arrangement of the magnets, the electrons can be made to circulate on a closed path on the target surface [2], confining the plasma there. The Ar^+ ions are accelerated to the negatively charged target as a result of the electric field and strike to the target surface with high velocities. As a result of the momentum transfer from the ions to the target material, the target atoms are removed from the target surface. Since sputtered atoms are mostly free of charge they will not be affected by magnetic or electric field and move towards the substrate surface to form the desired film.

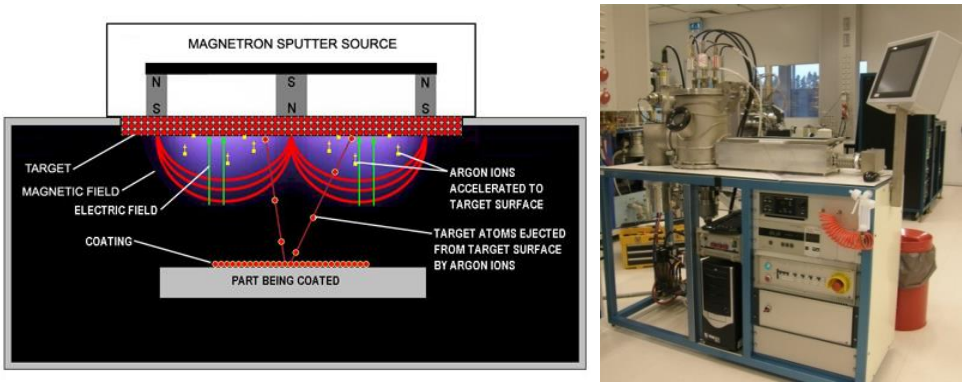

Figure 3.2 Illustration of the magnetron sputtering process [2] and photograph of the magnetron sputtering system 'Sputterke' in the MESA+ cleanroom.

In sputter deposition, the sputtered particles condense on the substrate surface and heat up the substrate. Substrate heating arises not only from the condensation energy of the depositing adatoms, but also from the high kinetic

energy of the depositing particles [2]. Many sputtered atoms have kinetic energies much higher that than those of thermally evaporated atoms. The kinetic energy per deposited metal atom in sputtering is on the order of 40 eV [3]. Therefore, magnetron sputtering can have destructive effects on organic molecules present on the substrate surfaces. In fact, in Chapter 5 this effect was exploited to alter the ligand structure around the Co ion to increase electron spin-impurity spin interaction by sputter deposition of a thin Au layer over the SAM.

In this thesis, the magnetron sputtering system 'Sputterke' was used for sputtering of Au. Before each deposition, the chamber was coated with 50-100 nm of Au in order to prevent cross contamination from the chamber. The lowest sputtering power that allows a stable plasma was used in order to decrease the deposition rate. To allow for straightforward comparison of measurement results, sets of samples were sputtered in the very same sputtering run. The magnetron sputtering conditions for all depositions were the same: at room temperature in 6.6×10^{-3} mbar Ar pressure with 60 W power (at 440 V) from an Au (99.99%) target. The Au target was cleaned by 1 min pre-sputtering before every deposition run.

In Chapter 4 and Chapter 5, Si/SiO_2(300 nm) substrates (2.2 mm x 6.8 mm) were used. After depositing ~5 nm of Au (deposition time: 10s), the samples were immersed into molecule solutions containing the Co- and/or Zn-complexes. After SAM formation, a second layer of Au of about the same thickness was sputtered with the same deposition conditions.

In Chapter 4, the same procedure was repeated for the sample with the sputtered Au capping layer. Si/SiO_2(300 nm) and transparent CaF_2 substrates were used for electron transport and Raman spectroscopy measurements, respectively (will be explained in coming sections). The total thicknesses for the samples with the sandwiched molecules were ~10 nm and for bare Au samples ~18 nm.

3.2.2 E-beam evaporation

Electron beam evaporation (e-beam evaporation) is a physical vapor deposition (PVD) process. Unlike sputtering, the atoms or molecules from a vaporization source reach the substrate without collisions with residual gas

molecules in the deposition chamber [4]. It is known to be less destructive compared to magnetron sputtering since the evaporated atoms arrive on the surface with less kinetic energy. Considering this, in Chapter 5 a thin Au capping layer was deposited over the molecules by e-beam evaporation to prevent the altering of the ligands upon the Au deposition.

The e-beam evaporation procedure is illustrated in figure 3.3. The target material inside a crucible is heated via an electron beam that is generated from a tungsten filament. The generated electron beam is accelerated to a high kinetic energy, using high voltages between 10-20 kV and directed towards the evaporation material. Upon striking the evaporation material, the electrons will lose their energy very rapidly. The kinetic energy of the electrons is converted into thermal energy through interactions with the evaporation material causing it to melt or sublimate. Once the temperature and vacuum level are sufficiently high, vapor will be released from the melt or solid. The resulting vapor can then be used to coat surfaces. The advantage of e-beam evaporation over thermal evaporation is the deposition rate and arrival energy of the evaporated atoms can be adjusted by adjusting the beam energy and beam size on the target material. Even very small deposition rates (1nm/min) are possible with this technique.

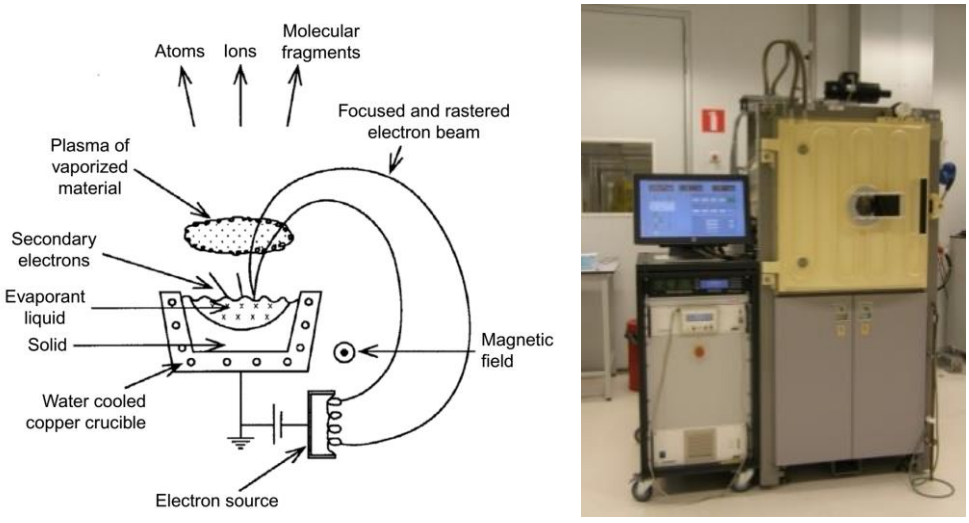

Figure 3.3. Focused electron beam (e-beam) vaporization source [4] and photograph of the BAK 600 e-beam evaporation system in the MESA+ cleanroom.

The heat of vaporization for gold is about a few eV per atom and the mean kinetic energy of the vaporized gold atom is about 0.3 eV, showing that the kinetic energy is only a small part of the energy released at the substrate during deposition [4]. This energy is significantly smaller compared to magnetron sputtered atoms (40 eV) as indicated in the previous section.

The e-beam evaporation of the Au capping layer on SAMs in Chapter 5 was performed with a Balzers BAK 600 evaporation system. The samples were stationed above the target at a distance of about 40 cm. The base pressure was lower than 1×10^{-6} mbar. The electrons were accelerated by using a 10 kV voltage source. Before the shutter was opened, the evaporation was started and stopped without turning the power off in order to clean the target and to be able to adjust small deposition rates in a controllable way. When the shutter was still closed, 260 mA current was used and the vacuum gauge was monitored. When the pressure increased, the current was ramped down to 180 mA and the shutter was opened. At this time, there was no evaporation. By slowly increasing the current, evaporation was started with 0.2 Å/s and about 5 nm Au film was evaporated on top of the SAMs.

3.3 Low-temperature electrical and magnetic characterization setups

3.3.1 Low-temperature probe station

In order to confirm that the graphene devices in Chapter 6 were measurable before they were loaded into a cryostat, they were tested in a probe station with needle probes that can be manipulated by micrometers. Electrical measurements can be done using external current/voltage source-measure units, as well as low-noise measurement electronics purchased from Delft University of Technology. The probe station enables a fast check of the devices without wire-bonding, simply by landing the probes on the contact pads. Electrical measurements can be done quickly at room temperature and in air, as well as in vacuum and at various temperatures. The sample chamber can be pumped down to pressures around $1x10^{-6}$ mbar with a turbo pump. The sample stage can be

cooled down to 4K by liquid ^{4}He flow and heated with a heater under the sample stage. A thermocouple under the stage enables adjusting the sample stage temperature, which makes it a very handy system to do temperature-dependent tests.

3.3.2 Physical property measurement system (PPMS)

Electrical and magnetic measurements (Chapter 4 and Chapter 5) at temperatures between 2 K to 300 K were performed with a Physical property Measurement system (PPMS) manufactured by Quantum Design [5].

The system consists of a dewar containing the ^{4}He bath (where the sample probe is inserted), the sample chamber and the sample probe with superconducting solenoid magnet. The sample chamber is inside the two vacuum tube (figure 3.4). The very base of the sample chamber contains a 12-pin connector that contacts the bottom of an installed sample puck. Two thermometers and a heater are immediately below the sample puck connector. The wiring for the sample puck connections, heaters, and thermometers runs up the outside of the sample chamber to the probe head. The region between the sample chamber and the inner vacuum tube is referred to as the cooling annulus. Helium is pulled through the impedance tube into the cooling annulus and pumped away causing the He to evaporate. This costs latent heat, and cools down the liquid. The temperature can be set between 1.8 K and 400 K.

The superconducting solenoid magnet is on the outside of the probe, so it is always immersed in liquid helium. The magnet coil constitutes a closed superconducting circuit, which eliminates the need for a current source during constant field operation. This state is referred to as the persistent mode of the magnet. The persistence switch is a small heater on the magnet wire that drives a section of the magnet non-superconducting so that the magnetic field can be changed. The magnetic field can be adjusted between 0 to 9 T.

The sample can be measured by supplying current between 5 nA to 5 mA. The compliance voltage is 95 mV and the maximum measurable resistance is 4 MΩ for current driven measurements.

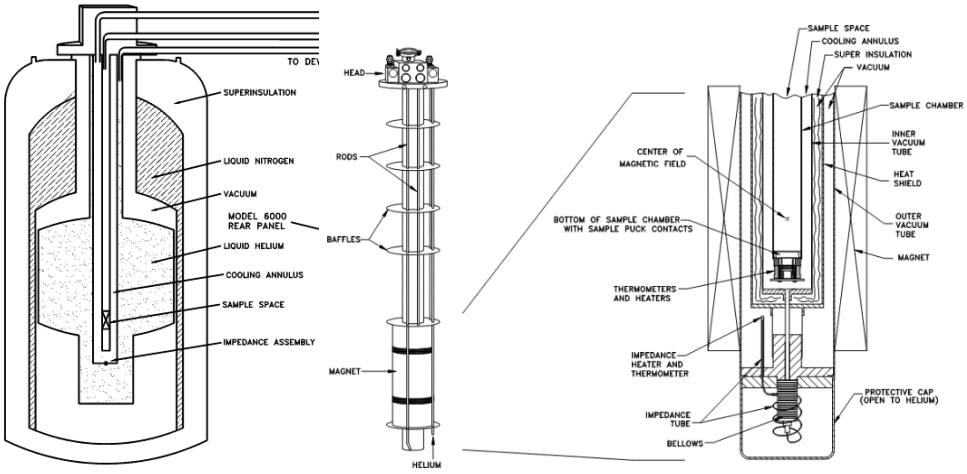

Figure 3.4 The PPMS dewar, the sample probe and the sample chamber [5].

In the experiments of Chapters 4 and Chapter 5, the sample resistance was measured in a standard four-terminal configuration as a function of temperature and magnetic field. The used temperature and magnetic field range was 2 K to 300 K and 0 T to 4 T, respectively. The excitation current was between 0.5 μA and 1.5 uA .

3.3.3 Heliox

In order to perform electrical and magnetic measurements down to 250 mK, we used a ^{3}He cryostat, namely a Heliox VL from Oxford Instruments [6]. The system can be cooled down to temperatures less than 300 mK by removing the ^{3}He, which is an artificially produced isotope of ^{4}He and with a lower boiling point. The overview of the cooling down procedure of the system is given below.

The system consists of an outer chamber with liquid N_2 (for pre-cooling) and liquid ^{4}He compartments, a superconducting coil which can provide magnetic fields up to 8 T and the insert involving the inner vacuum chamber (IVC) (figure 3.5). Inside the IVC, the sorb, the charcoal sorption pump, the 1K pot, the ^{3}He pot, and the sample are enclosed and isolated from the ^{4}He filling the outer chamber. A capillary and a needle valve is connected to the IVC to let liquid ^{4}He flow into 1K

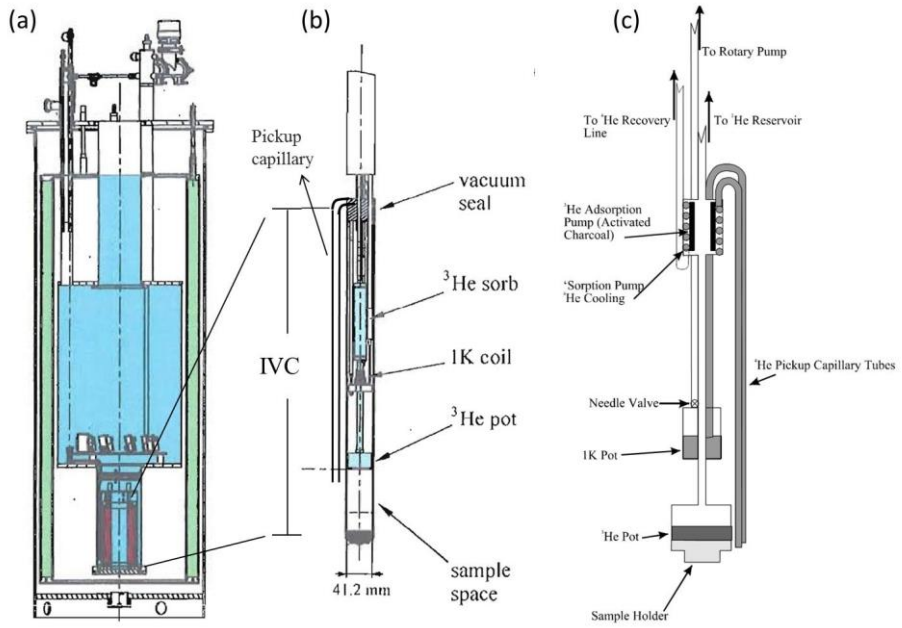

Figure 3.5 (a) Heliox dewar. Green, blue and red shadings: liquid nitrogen shielding, liquid helium tank, and the superconducting solenoid, respectively. (b) Inner vacuum chamber (IVC) and sample insert. Shaded components are the sealed ^{3}He position [7]. (c) detailed sketch of the sample insert inside the IVC [8].

pot. Electrical connections from the sample reach through the interior of the inserts and connected to the measurement electronics unit from the cryostat via a multi-pin interface at the top of the insert.

The sample is mounted in contact with the ^{3}He pot. The IVC is sealed and vacuumed. After vacuum is reached, a small amount of He gas is transferred inside the IVC as exchange gas to make thermal contact to the walls of IVC. The insert is dipped into the liquid ^{4}He and the temperature reaches to about 4.2K. In order to cool down to base temperature, the 1K pot is constantly evacuated by a rotary pump and then filled with liquid ^{4}He from the outer chamber via the capillary and needle valve. By evacuating, the 1K pot cools down to below 1.5 K; lower than the condensation temperature of ^{3}He. The sorb is a charcoal sorption pump, which will pump on helium gas if its temperature is below 10K, but it will

completely expel any gas if kept above 30K. The sorb is heated to about 35K, so that it will release the adsorbed ^{3}He gas. The released ^{3}He gas will condense when it comes in contact with the 1K pot and run down to the ^{3}He pot. After about 30 minutes, the ^{3}He pot will be nearly full of liquid ^{3}He at approximately 1.5 K. At this stage, heating of the sorb is stopped and it is cooled instead, so it will start evacuating the ^{3}He pot. The pressure in the ^{3}He pot will decrease and the ^{3}He will evaporate from the bath to the sorb, decreasing the temperature down to 260mK. With heaters, the sample temperature can be controlled approximately between 260mK to 100K. Since ^{3}He is very expensive, it is kept in a closed system and recycled by evaporation and condensation. Therefore, the system can be at the base temperature only until all the ^{3}He in liquid phase is evaporated, then condensation must be done. This means that he system can be at base temperature for about 24-30 hours.

The system has a superconducting solenoid magnet immersed in liquid ^{4}He. It can provide adjustable and homogeneous magnetic field from 0T to 8T by a superconducting current that runs through the coil. When a constant current is running through the coil, it is in the so-called persistent mode. To change the current, therefore the magnetic field, a small part of the magnet is heated and turned into the “normal” state (opposed to superconducting state).

In order to make accurate measurements at such low temperatures, several measures were taken. For instance, at temperatures lower than 1K, the electron temperature can rise due to high frequency noise in the MHz/GHz regime, which originates from stray fields of electrical instruments at room temperature. In order to prevent such noise, π (LC) filters (at room temperature) and RLC filters (low temperature) were used. In addition, to prevent electron heating, the voltage drop across the samples (V) was adjusted such that $eV < 3.5\ k_B T$ (=81.2 μeV at T=270mK).

In order to perform low noise measurements, battery driven measurement electronics designed by R.N. Schouten from Delft University of Technology was used. The measurement electronics consists of isolation amplifiers: current sources and voltage amplifiers, which isolate the measurement electronics from the outside world (e.g. external sources like lock-in amplifiers and external measurement units like digital multimeters). An AC

voltage is sourced from a lockin amplifier with a frequency of 17.7 Hz and converted into current by the current source unit. The voltage drop across the sample was amplified by the voltage amplifier of the measurement unit and read by the lockin amplifier. The read value was sent to the measurement computer via a GPIB connector. The measurement electronics and the computer were connected by an optical fiber.

3.4 Synchrotron radiation techniques

Synchrotron radiation techniques are intensively used to probe electronic (band) structure and chemical composition of materials. Also in this thesis work, these techniques were used to obtain information about the material composition on the surface and the electronic environment of the core ions in the SAMS. The synchrotron radiation techniques that are used in this thesis are photoemission spectroscopy (PES) and x-ray absorption spectroscopy (XAS).

Synchrotron radiation is the electromagnetic radiation emitted by electrons when they are accelerated radially at highly relativistic velocities as their direction is changed by bending magnets. In synchrotron sources (figure 3.6), electrons from a source (e.g. a heated filament in an electron gun) are accelerated in a linear accelerator (linac) into an evacuated booster ring, where they undergo further acceleration. They are then injected into the so-called storage ring. There, they are maintained in a closed path using bending magnets at arc sections. The beamlines use the radiation emitted from insertion devices and/or from the bending magnets, and therefore are positioned downstream, on the axis of emission. The energy lost by radiation of synchrotron light by the electrons is replenished by a radio frequency (RF) supply [9] .

Intense and tunable x-ray beams can be created in synchrotron radiation sources. x-rays are able to probe deeply and nondestructively in solid materials. Many synchrotron radiation techniques depend on the detection of electrons emitted from the sample upon interaction with the incident x-rays. These electrons can only escape from the near-surface region of the sample (depending on their kinetic energy and sample composition) resulting in surface sensitivity of these techniques [9].

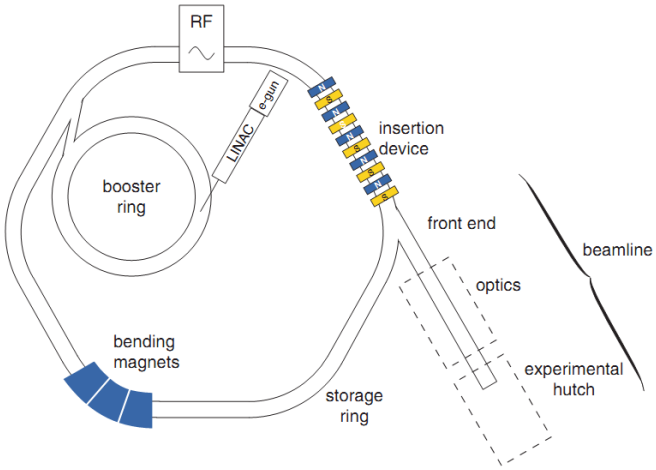

Figure 3.6 A schematic of the most important components of a modern synchrotron source [7].

The synchrotron measurements in Chapter 5 (PES, XAS) were acquired at beam line D1011 of the MAXII storage ring at the synchrotron radiation facility MAX-lab in Lund, Sweden. D1011 is a bending magnet beamline, covering a photon energy range of about 100 to 1800 eV. The measurement station consists of separate analysis and preparation UHV chambers, and a load-lock. The analysis chamber is equipped with a SCIENTA SES200 (upgraded) electron energy analyzer (for PES measurements), and a multi-channel plate (MCP) detector (for XAS measurements). An incident angle of 45° of the photon beam relative to the sample normal was used for all types of measurements, corresponding to "normal emission" (detection of electrons emitted along the sample normal) for PES measurements.

In Chapter 5, the electronic environment of Co ions was investigated by PES and XAS techniques. The effect of Au capping via evaporation and sputtering on the ligand structures of the molecules were studied. The “evaporation effect” was investigated via in-situ evaporation of Au inside the preparation chamber by thermal evaporation using a W filament wire coated with Au. The base pressure of the preparation chamber was 10^{-10} mbar and the pressure during the Au

deposition was ~5 × 10^{-9} mbar. The effect of Au on the SAMs were investigated with PES, XAS. The effect of sputtering was tested on an ex-situ sputtered sample.

3.4.1 Photoemission Spectroscopy

Photoemission spectroscopy (PES) is used for gathering information about a material's electronic (band) structure. Studies of core-levels with soft x-rays give information about the chemical composition of the surfaces. An approximate calculation of the thickness of very thin layers is also possible, using the attenuation of substrate signals and knowledge of the inelastic mean free path of photoelectrons in these layers. In this work, we used PES to study the properties of the SAMs and for calculating the thicknesses of the Au capping films.

The brief principle of the technique is as follows: When a photon with an energy higher than the binding energy of a core electron is absorbed, the core electron is ejected into an unbound state. The kinetic energies of these directly ejected photoelectrons can be measured, which supplies information on the elemental and chemical composition of materials. PES is used to draw quantitative conclusions about the electronic and/or chemical nature of materials over a broad range of excitation x-ray energies, and explained by Einstein's explanation for the photoelectric effect:

$$E_B = h\nu - E_k - e\phi \qquad (3.1)$$

where E_B is the binding energy which can be defined as the energy needed to promote the electron to the continuum (or 'vacuum level') but is insufficient to pull it away from the sample, $h\nu$ is the incident photon energy, E_k is the kinetic energy of photoelectrons and $e\phi$ is the work function. The work function corresponds to the minimum energy required to eject an electron from the material [10]. The binding energies of energy levels in metals are generally measured with respect to the Fermi level, rather than the vacuum level since the spectrometer and the (conducting) sample has a common Fermi energy when in contact, which helps avoiding the use of often unknown work functions [9].

According to the used photon energy range, PES can be divided into three broad categories from: ultraviolet photoelectron spectroscopy (UPS), x-ray

photoelectron spectroscopy (XPS) and hard x-ray photoelectron spectroscopy (HAXPES). The synchrotron beamline D1011 covers the soft x-ray regime [11].

An important parameter determining the surface sensitivity in PES spectroscopies is the *inelastic mean free path (IMFP)*. The IMFP is defined as the average depth from which the photoelectrons can escape the surface without losing energy and reach the detector to contribute to the PES signal [9]. It can be used to calculate the layer thicknesses even for very thin layers as was used in Chapter 5 to calculate the in-situ evaporated Au capping layer thicknesses. By comparing the PES (or XPS) signal intensities before and after a layer is deposited over a metallic substrate (I and I_0, respectively), the thickness of the layer can be determined by using the equation: $I=I_0\ e^{-t/\lambda}$, t is the thickness of the deposited layer and λ is the IMFP of the electrons. The latter can be obtained from the "universal curve" of the inelastic mean free path of electrons in metals (which holds for Au) at a given kinetic energy [12]. In chapter 4, the thickness of the Au capping layers covering the molecules was calculated from this equation comparing the PES intensities before- and after deposition of the Au capping layers.

The analysis of the SAMs on Chapter 5 and SAMs on SiO_2 in Chapter 6 were investigated via XPS. The measurements were performed by Gerard Kip at the University of Twente with a Quantera SXM from Physical Electronics. An Al Kα x-ray source with 1486.6 eV incident photon energy was used to generate x-ray beams of 25W power with diameter of down to 9 μm (for lateral mapping). The beam-input and detector input angle was 45^o.

3.4.2 X-ray absorption spectroscopy (XAS)

In contrast with XPS, which is based on using a fixed incident photon energy and measuring the kinetic energy of the ejected photoelectrons, XAS probes excitations of core level electrons promoted to unoccupied valance states as a function of the incident photon energy (and therefore can only be performed at synchrotrons). In this work, the XAS spectra are recorded by measuring the total electron yield (TEY) of electrons emitted upon the decay of the core-excited states. This involves Auger electrons (see discussion below), and also secondary

electrons emitted due to inelastic scattering of these Auger electrons. The secondary electrons actually constitute the majority of the yield. Each point in an XAS spectrum can be thought of as being the energy-integrated intensity of an "XPS spectrum" recorded using the photon energy associated with that point in the XAS spectrum (figure 3.7) [12].

XAS is a powerful and, when electron yield is measured, surface-sensitive technique. It gives information about electronic structure of materials and the molecular bonds. Since unoccupied states are involved, the technique probes a part of the electronic structure that is not accessible by PES. The electronic state of an atom partaking in chemical bonding is different from that of the same atom in an isolated state, due to the redistribution of (primarily) the outermost electrons in the valence or conduction band. The redistribution of the valence electrons caused causes small changes in the binding energy (so-called 'chemical shifts') of core-electrons, which can provide valuable information on the chemical nature of the sample under investigation[9]. As mentioned earlier, in Chapter 5 XAS was used to gain information about the electronic environment of the metal core ions in the SAMS before/after Au capping via sputtering/evaporation. Since the Au capping layers were very thin, it was still possible to probe the spectral features of the molecules after capping. The effect of capping on the ligand structure and the Co ion was investigated by probing the C, N and Co spectra.

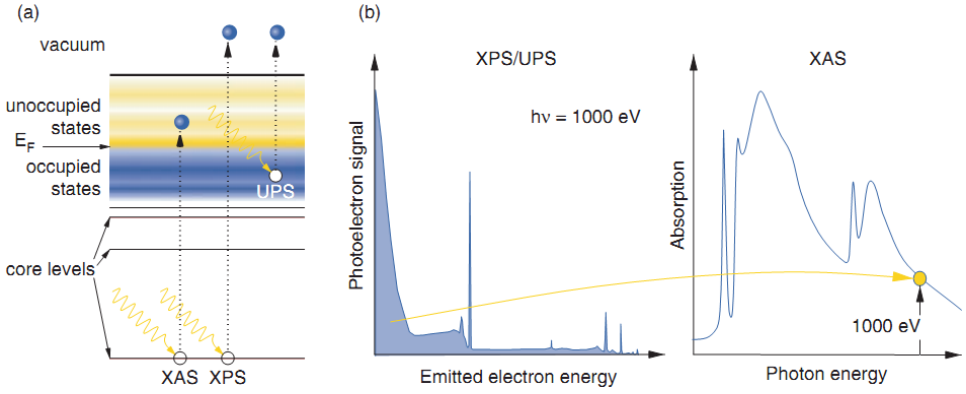

Figure 3.7 (a) Schematics of XAS, XPS and UPS processes and their relationship. (b) Each point in an XAS spectrum can be thought of as the integrated XPS signal for the photon energy of interest [7].

When a photon hits the sample surface, it can be scattered by the electrons of the sample, be absorbed, or transmitted. If it is absorbed, a core electron is excited to an unoccupied valence state (XAS process) or to the continuum (photoelectrons-PES process), leaving a hole in the core level. This hole can be filled by an electron from an outer shell. During this relaxation, the excess energy can either be emitted in the form of characteristic x-ray radiation (fluorescence) or by the ejection of Auger electrons. The ejected electrons may scatter on their way to the sample surface, leading to a collision cascade, in which a large number of low-energy electrons is produced.

XAS data can be acquired in two different ways: in transmission mode or in total electron yield mode (TEY) (figure 3.8) [9].

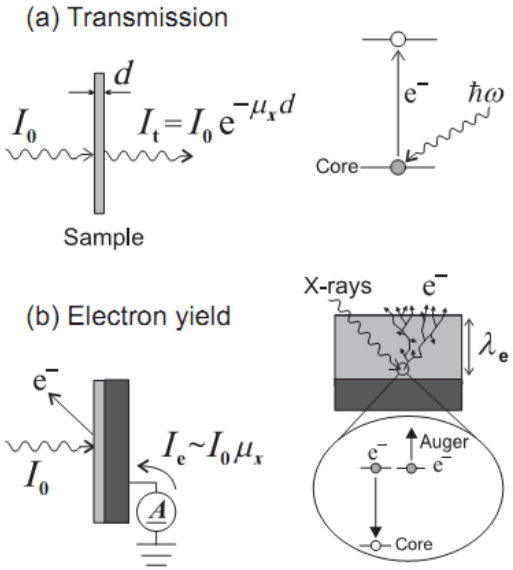

Figure 3.8 Two methods of XAS measurement transmission, and total electron yield detection, where L is the sampling depth (typically a few nanometers) [12] .

In transmission mode, the amount of x-ray that passes through a thin sample is measured. The x-ray intensities before entering the sample (I_0) and after (I_t) are measured using ionization chambers or other beam-intensity monitors.

The absorbing power of a material is given by the absorption coefficient μ, which describes the exponential drop in intensity of an incident beam passing through a medium. μ depends on the types of atoms constituting the medium, how they are distributed, the nature of their bonding, magnetism, the light polarization and the wavelength of the x-rays. In the simplest case, μ is determined by comparing the intensities of the beam entering and after it emerges from a sample of known thickness d such that $I_t = I_0 e^{-\mu d}$.

In the TEY mode, all emitted electrons (Auger electrons and low-energy electrons) are measured by a picoammeter connecting the sample to ground. The resulting "drain current" signals are proportional to the x-ray absorption intensity. In order to eliminate the low energy electrons, a grid at a fixed retarding potential can be inserted in front of an electron multiplier such as a microchannel plate detector (MCP). This type of measurement is called partial electron yield (PEY) measurements. In this work, all XAS spectra were measured at room temperature in total electron yield mode, with a probing depth of about 10 nm. The backgrounds for correction of the Co L-edge, C K-edge and N K-edge spectra were measured from a clean, in-situ deposited Au film on a Si substrate, and removed from the XAS spectra.

When the photon energy is just sufficient to eject the electron from the electronic orbital to the bottom of the conduction band in metals or to the lowest unoccupied molecular level (LUMO) in organic molecules, sharp increases are observed in the absorption spectrum, known as absorption edges. The energy at which electrons from the n=1 level (1s) are ejected is called K edge, whereas n=2 (2p) and n=3 (3s, 3p, 3d) ejection energies are known as L and M edges.

3.5 Raman Spectroscopy

Raman spectroscopy is a characterization method revealing vibrational transitions in matter. In Chapter 5, Raman spectroscopy was used to investigate molecular vibrational levels of the Co complexes to reveal possible changes in molecular structure before/after capping procedures. In Chapter 6, Raman spectroscopy was used to characterize graphene layers that were transferred over the molecular layers.

Raman spectroscopy depends on the interaction of (laser) light in the visible, near infrared or near ultraviolet range with the electron cloud and the bonds of the molecule. When light interacts with matter, scattering events via 'virtual energy levels' can take place. The light induces a dipole moment in the molecule. The generation of this dipole moment by the incoming electric field is modulated by the molecular vibrations. Therefore, the induced dipole oscillates not only at the frequency of the incoming field, but also at 'side bands', which can be referred to as virtual energy levels [13]. The scattering processes by these levels involve instantaneous absorption of an incoming photon and subsequent emission of another photon. Mostly, the emitted photon has the same energy as the incoming photon ($h\nu_0$, where h is the Planck constant and ν_0 is the frequency of incoming light) which makes it an elastic scattering event, also called Rayleigh scattering. In more rare occasions, the scattering event is inelastic, meaning the photon has lower or higher energy by an amount equal to a vibrational transition ($h\nu_1$). These inelastic scattering events are called Raman scatterings. The Raman scattered photons with lower energy $h(\nu_0 - \nu_1)$ is named as Stokes scattered photons, whereas photons scattered with higher energy $h(\nu_0 + \nu_1)$ is named as anti-Stokes scattered photons. Figure 3.9 illustrates these transitions.

Raman scattering probes vibrational levels of the molecule, which depend on the constituent atoms and their bond strengths and arrangements in a specific molecule. Therefore, a Raman spectrum provides a 'fingerprint' of a molecule [14]. However, a great disadvantage of the technique is that the Raman scattering process is extremely very weak, compared to Rayleigh scattering. Only a small fraction of the incident photons (approximately 1 in 10 million) are Raman scattered, which makes the Raman signal to be very weak and hard to detect [14]. The discovery of Surface enhanced Raman Spectroscopy (SERS) helped to overcome this problem. The SERS was first discovered on pyridine molecules on roughened silver electrodes with the observation of strongly enhanced Raman signals [15]. Similar observations in different laboratories with many different molecules verified the enhancement of Raman signals from various roughened metal surfaces [16].

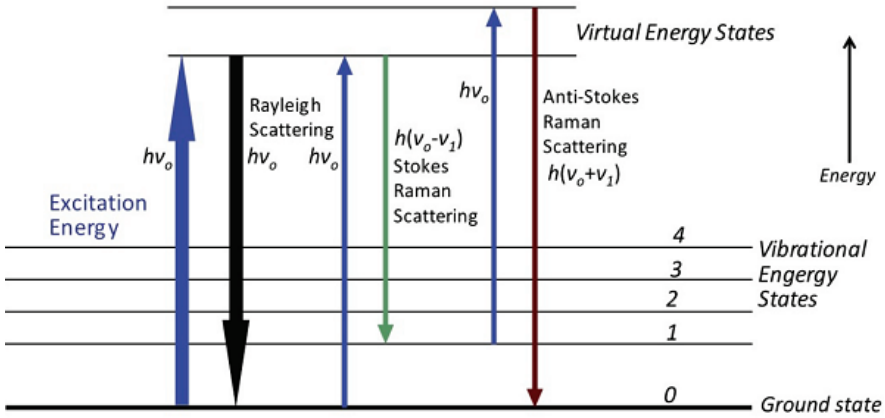

Figure 3.9 Spectroscopic transitions corresponding to Rayleigh scattering (hv_o), Stokes ($h(v_o-v_1)$) and anti-Stokes ($h(v_o+v_1)$) Raman scattering. The laser excitation frequency is v_o [14].

Over the years, the enhancements have been attributed to two main mechanism, although their relative contribution is still not completely clear [17, 18]. The first one is the electromagnetic enhancement, which is due to strong electromagnetic fields induced by laser excitation of surface plasmon polaritons (SPP) on nanoscale noble metal (Au, Ag and Cu) structures at wavelengths in the visible spectrum [19]. The enhanced electromagnetic field can transfer energy to molecules located near the surface of the nanostructures, which increases the magnitude of the induced molecular dipole, and therefore, the intensity of the inelastically scattered photons increases and greatly enhances the Raman scattering efficiency [20, 21]. The second mechanism is the chemical enhancement, resulting from the interaction between molecules and the metallic host and it is suspected that a charge transfer between the molecule and host metal is necessary to achieve a strong enhancement [18, 22]. However, it is commonly accepted that the dominant effect causing the large scattering enhancement is due to the electromagnetic enhancement. Raman signal enhancements enabling detection down to the single-molecule level have been reported.

Different SERS active substrates have been reported in literature. For a review, see Ref [19]. Amongst these, substrates prepared by sputtering thin Au layers are attractive due to easy preparation and success in signal enhancement [23]. Another technique reported for enhancement is to evaporate a thin layer of Au on a monolayer assembled on Au(111) epitaxial Au films. The evaporated layer resulted in the SERS activation of SAMs even on an atomically-flat Au(111) surface, probably by inducing a specific nanometer-scale roughness [18]. Our system in Chapter 5, which consists of SAMs on a thin sputtered Au showed significant Raman signals of the Co-complexes. The capping procedure was expected to result in further enhancement, as indicated above. In SERS measurements, CaF_2 substrates were used, which are known to have a silent background in the interested Raman shift region (900-2000 cm^{-1}).

SERS measurements in Chapter 5 were performed by Aufried Lenferink from Medical Cell BioPhysics (MCBP) Group, University of Twente with a custom-built laser-scanning Raman microspectrometer with an excitation light of 647.1 nm wavelength (the setup is described in more detail in [19]). Data acquisition was performed by stepping the laser beam over the sample in a raster pattern and spectra were acquired at each position. All spectra were corrected for setup response, and were averaged over 1024 (32 x 32) measurements. A laser power of 10 mW was used. It was confirmed that no degradation of the molecular layer occurred with this power level. The confirmation was based on measurements acquired with increasing laser power until a change in the spectrum was observed. Until 10 mW, no observable change was detected in the spectra.

References

[1] M. Maskus and H. D. Abruna, "Synthesis and characterization of redox-active metal complexes sequentially self-assembled onto gold electrodes via a new thiol-terpyridine ligand," *Langmuir,* vol. 12, pp. 4455–4462, 1996.

[2] D. M. Mattox, "Physical Sputtering and Sputter Deposition (Sputtering)," in *Handbook of Physical Vapor Depositon (PVD) Processing*, ed USA: Elsevier Inc., 2010, pp. 237-286.

[3] "Energy Deposition at the Substrate," in *Reactive Sputter Deposition*, ed Verlag Heidelberg Berlin: Springer, 2008, pp. 229-255.

[4] D. Mattox, "Vacuum Evaporation and Vacuum Deposition (PVD) Processing " in *Handbook of Physical Vapor Depositon*, ed USA: Elsevir Inc., 2010, pp. 195-235.
[5] *Physical Property Measurement System Hardware Manual*. San Diego: Quantum Design, 2008.
[6] *Heliox VL Manual*. Oxon: Oxford Instruments NanoScience, 2013.
[7] MatthewFairbanks, *PhD Thesis: Electron Transport in Microto Nanoscale Solid State Networks*: University of Oregon, 2010.
[8] G. Burnell, *PhD Thesis: Quasiparticle and Phonon transport in superconduxting particle detectors*: University of Cambridge, 1998.
[9] P. Willmott, *An introduction to synchrotron radiation: techniques and applications* West Sussex: John Wiley and Sons, Ltd, 2011.
[10] "MAX-lab D1011Beamline," ed.
[11] T. T. L. Anh, "PhD Thesis: Spintronics using C60 fullerenes: Interfaces and devices," ed. Enschede: NanoElectronics group, University of Twente, 2013.
[12] *J. Phys. Chem.,* vol. 28, p. 19, 1999.
[13] J. S. a. H. C. Siegmann, *Magnetism: from fundamentals to nanoscale dynamics*. Berlin Heidelberg: Springer, 2006.
[14] e. a. K. Kneipp, "Surface-enhanced Raman scattering and biophysics," *J. Phys.: Condens. Matter 14,* vol. 14, pp. R597–R624 2002.
[15] G. a. C. J. Turrell, *Raman Microscopy, Developments and Applications*: Elsevier Academic Press, 1996.
[16] M. Fleischman, P. J. Hendra, and A. J. McQuillan, *Chem. Phys. Lett 26 123,* vol. 26, p. 123, 1974.
[17] A. Otto, "Surface-enhanced Raman scattering: 'classical' and 'chemical' origins," *Topics in Applied Physic,* vol. 54, pp. 289-418 1984.
[18] A. e. a. Marlen, "Surface enhanced Raman spectroscopy of organic molecules deposited on gold sputtered substrates," *Nanotechnology 20,* vol. 20, p. 215705, 2009.
[19] T. a. O. Wadayama, M, "Surface-enhanced Raman spectral study of Au nano-particles/alkanethiol self-assembled monolayers/Au (111) heterostructures," *Surf Sci.,* vol. 600, pp. 4352–4356, 2006.
[20] M. Moskovits, *J. Chem. Phys.,* vol. 69, p. 4159, 1978.
[21] D. L. Jeanmaire and R. P. VanDuyne, *J. Electroanal. Chem. ,* vol. 84, p. 22, 1977.
[22] M. G. Albrecht and J. A. Creighton, *J. Am. Chem. Soc. ,* vol. 99, p. 5215, 1977.
[23] M. Fan, A. G.F., and B. A.G., "A review on the fabrication of substrates for surface enhanced Raman spectroscopy and their applications in analytical chemistry," *Anal Chim Acta,* vol. 693, pp. 7-25, 2011.

Chapter 4

Tunable Molecular Spin Doping of a Metal

The mutual interaction of localized magnetic moments and their interplay with itinerant conduction electrons in a solid is a key fundamental topic in solid-state physics. These mechanisms form the very basis of magnetic ordering and related many-body phenomena, such as the Kondo effect, Ruderman-Kittel-Kasuya-Yoshida (RKKY) interaction, and carrier-induced ferromagnetism in diluted magnetic semiconductors. Crucial parameters determining the strength and the relative importance of these spin phenomena, are the magnitude and sign of the exchange interaction, and the mean distance between the localized magnetic moments. To enable systematic study of a given magnetic impurity-host system, straightforward tuning of the mean distance between the impurities is highly desirable, as this sets its physical properties. In this Chapter a novel, facile molecular fabrication method for inserting isolated localized magnetic moments in a gold film with tunable density is presented. Kondo and weak localization measurements demonstrated that the magnetic impurity concentration can be systematically varied up to ~800 ppm concentration without any sign of inter-impurity interaction, or undesired clustering often suffered from in alternative methods.

This chapter has been published as T. Gang, M. Deniz Yilmaz, D. Ataç, S. K. Bose, E. Strambini, A. H. Velders, M. P. de Jong, J. Huskens and W. G. van der Wiel, *Nature Nanotechnology* 7, 232–236 (2012).

4.1 Introduction

The inclusion of even a small amount of magnetic impurities in a metal can have drastic effects on the physical properties, such as the electrical resistivity and magnetic susceptibility. A well-known example is the anomalous electrical resistivity minimum at low temperature, referred to as the Kondo effect [1]. Another example is the reduction of the carrier phase coherence time due to enhanced spin scattering introduced by the impurity magnetic moments [2]. For systematic experimental study of such phenomena, good control of the magnetic impurity concentration is indispensable. The most common method for varying the amount of magnetic impurities is by alloying a non-magnetic and magnetic metal in different ratios. The preparation of such alloys is far from trivial though, and each desired impurity concentration needs to be prepared separately. It requires delicate procedures such as melting, swaging, etching, annealing, and quenching to ensure uniform mixing and avoid element segregation [3]. Moreover, impurity concentrations are limited up to about 100 ppm, as for higher values segregation or clustering occurs. In a few other studies, magnetic atoms were deposited on a host metal (Au) in ultra-high vacuum and at cryogenic temperatures to prevent agglomeration [2]. However, also here impurity agglomeration is very hard to exclude at a few hundred ppm level.

In this Chapter, a novel, facile molecular fabrication method for magnetic doping up to high concentrations of isolated impurities is presented. The power and versatility offered by molecular bottom-up assembly are more and more exploited in the fabrication of electronic devices. As the critical dimensions approach the molecular scale, the application of molecules as building blocks or scaffolds for electronic components becomes increasingly attractive. Of particular interest are self-assembled molecular monolayers (SAMs), which, owing to their self-limited growth, offer large-area 2D systems that can be engineered at the molecular scale. Although molecular monolayers have been used for tuning metal work functions [4], for self-assembled-monolayer field-effect transistors (SAMFETs), for surface transfer doping of semiconductors [5], for uniform [6] and patterned [7] doping of silicon with donor atoms [8] and for the modification of the electronic properties of graphene [9] (as was also presented in Chapter 6), they were not used for magnetic doping of the metals before. In this chapter, we

realized magnetic doping from a molecular monolayer [10].

4.2 Doping Method

As was described in Chapter 3, our method consists of inserting isolated localized magnetic impurities in a gold film from a monolayer of metal-ligand complexes. The metal core is chosen to be either a Co^{2+} or Zn^{2+} ion, and is coordinated in a distorted octahedral manner by two perpendicularly positioned terpyridine ligands. Whereas Zn^{2+} is spinless, Co^{2+} does carry a spin (spin door). At low temperatures relevant for this work (2-80K), Co^{2+} is known to be in the low-spin ground state with S = ½ [11]. By cyclic voltammetry (see Section 4.4.A), we have confirmed that Co^{2+} in the bis-terpyridine complex can be oxidized to zero-spin Co^{3+} at relatively low energy (~0.25 eV), a property that allows for Kondo physics at low temperature [12]. The inset of figure 4.2 shows the metal terpyridine complex used in this study. By mixing these two metal complexes with/without spin we could straightforwardly control the concentration of magnetic moments.

Monolayers were formed on thin Au layers (~2.5nm) from 0.1 mM mixed complex solutions of acetonitrile having different ratios of Co^{2+} and Zn^{2+} complexes (0, 25, 50, 67 and 100% Co), on separate Si/SiO_2/Au substrates (see Chapter 3 for details). It should be emphasized that the perpendicular arrangement of the terpyridine ligands in the Co^{2+} and Zn^{2+} complexes and the lack of strong intermolecular interactions prevent the formation of a highly ordered (i.e. lattice-like) monolayer. The monolayer is thus expected to be rather disordered. The ~2.5 nm Au films (99.99% Au source) were sputter deposited (without adhesion layer) in a single run (see Chapter 3 for a detailed description of the fabrication process). The metal deposition process was optimized for getting sufficiently disordered films, suitable for weak localization measurements (described below). As the molecular complexes are identical (in outer ligand structure, overall charge, size, and shape), except for their core metal ion (i.e. either Co^{2+} or Zn^{2+}), the same adsorption rate, footprint, and affinity for the gold substrate are expected for both species. We therefore anticipate a homogeneously mixed monolayer on top of the Au film, reflecting the Co:Zn ratio

of the mixed donor solution. XPS measurements (see Section 4.4.C) confirm that this is indeed the case, as well as the detailed low-temperature electron transport measurements, discussed below. From electrochemical characterization, a molecular coverage of 5×10^{-11} mol/cm^2 was estimated, corresponding to ~1 molecule per 3 nm^2 (see Section 4.4.D). After monolayer formation, the samples were covered with a top Au layer of the same thickness as the bottom layer, meaning that the SAMs were sandwiched between two Au layers instead of sitting on top of a single layer (will be discussed below). Based on the measured molecular coverage and the total thickness of the Au layer, we expect a maximum realizable magnetic impurity concentration on the order of 10^3 ppm.

To confirm the systematic variation of the magnetic impurity density, low-temperature electron transport measurements exhibiting the Kondo effect and weak (anti-)localization were performed. In this Chapter the results of one series of samples prepared in the same Au deposition run are presented. Although not shown, the results were reproducible to a high degree for more than 5 independent fabrication runs.

4.3 Results and Discussion

4.3.1 Temperature dependence of resistivity

Electron transport measurements were performed on Au films molecularly spin doped from donor solutions with different Co complex:Zn complex ratios (0, 25, 50, 67 and 100% Co), as well as on a reference sample immersed in a solution without metal complexes. Sample resistances were measured in a standard four-terminal configuration with an excitation current between 0.5 and 1.5 μA.

Before investigating the different samples with different Co complex:Zn complex ratios, we inspected the films with 100% Co complexes and bare Au films to observe a clear resistivity difference between the two. We observed that if a thin layer of Au is deposited on the SAMs, the difference in the resistivity of the samples doped with Co complexes and the bare Au films becomes much more clear.

Molecular spin doping with 100% Co complex SAMs

Figure 4.1 shows the temperature dependence of the resistivity for 5nm thick Au films dipped into 0% (just acetonitrile) and 100% Co complex solutions with/without the deposition (by sputtering) of a thin second layer of Au on top. The films were dipped in the solutions i) after 2.5nm Au deposition, followed by the top Au deposition of the same thickness, and ii) after complete deposition of 5 nm. So, in the first case, the SAM was *in between* two layers of 2.5nm Au and in the latter case, the SAM was *on top* of complete Au layer of 5nm. A bare Au film of 5nm that was not dipped into any solutions was also characterized as reference.

Although the bottom/top Au layers (the complete Au layers) have been deposited in the same deposition runs for all samples, there are slight sample-to-sample resistivity variations (see Section 4.4.E). To make direct comparison possible, the resistivity values have been normalized according to $\rho_{\mathrm{norm}}(T) = \frac{\rho(T)-\rho_{\mathrm{min}}}{\rho(150\mathrm{K})-\rho_{\mathrm{min}}} \times \rho_{\mathrm{Au}}(150\ \mathrm{K})$ with ρ_{min} the minimum resistivity value of each curve, and $\rho_{\mathrm{Au}}(150\ \mathrm{K})$ the resistivity of the bare Au film at 150 K.

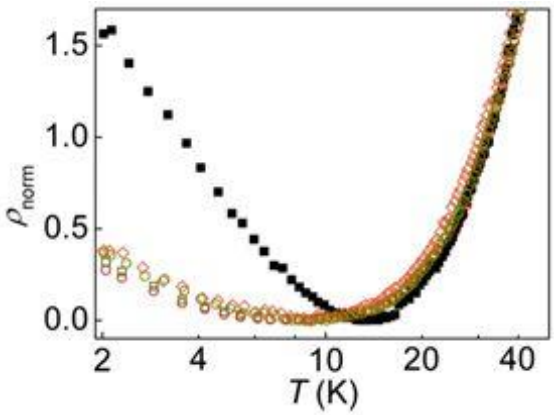

Figure 4.1 Temperature-dependent normalized resistivity plots of (99.99%) pure Au films (green hexagons), and Au films with 0% Co with top Au (orange diamonds) and without top Au (red circles), and 100% Co with top Au (black squares) and without top Au (green open squares).

It was observed that the 100% Co complex sample with the top Au shows a resistivity minimum $\rho_{\min}$ at T_{min} between 10 K and 20 K followed by a clear logarithmic resistivity upturn. Similar behavior was seen in a 100% Co complex sample without the top Au, but in a much weaker form. The resistivity minimum and logarithmic upturn are indicative of the Kondo effect, which arises from the interaction of a localized magnetic impurity with the spin of itinerant conduction electrons in the host metal [1]. Coherent superposition of (higher-order) spin-flip scattering eventually leads to the complete screening of the localized moment below a critical temperature, referred to as the Kondo temperature, T_K. A many-body singlet state is formed by the impurity and a "cloud" of conduction electrons (see Chapter 2). As the scattering cross section of this Kondo cloud is larger than that of the original impurity, the resistivity increases in case of bulk diluted impurity systems. The Kondo effect is in essence a single-impurity phenomenon. In metals, however, the resistivity upturn results from the contribution of many uncorrelated magnetic impurities. More recently, the Kondo effect has also been studied at the single-impurity level, using scanning tunnelling microscopy of single magnetic impurities formed by an adatom or molecule on a metal substrate [13, 14], or using electron transport through semiconductor quantum dots [15] or single molecules [12]. In such systems, it was shown that the impurity can indeed be completely screened [16].

The clear upturn in the 100% Co complex sample with top Au (much weaker in the sample without top Au) demonstrated that the metal film was effectively doped with localized magnetic impurities from the Co complex molecular monolayer. The much stronger upturn in the 100% Co-complex sample with the top Au was attributed to the increase of the interaction between the spin dopants and the conduction electrons in the Au film as a result of (partial) destruction of the organic ligands during the top Au deposition. Chapter 5 is dedicated to investigate the effect of Au deposition on the SAMs. All the samples that are discussed below had top Au deposition by sputtering on top of the SAMs.

It should be noted that instead of being saturating at low temperatures, the resistivity of the 0% Co complex (with/without top Au) and the bare Au showed a resistivity upturn slightly less than the 100% Co complex sample without the top Au. This upturn was related to unintentional dopants most probably

present in the Au target material (will be discussed below).

Tuning the concentration of molecular spin dopants

Given that the molecular spin doping of the metal via Co complex SAMs was successful, the next step was to tune the concentration of the spin dopants in a controlled way. As described earlier, the concentration was changed by using donor solutions with different Co complex:Zn complex ratios (0, 25, 50, 67 and 100% Co). A reference sample immersed in a solution without metal complexes, but fabricated in exactly the same way otherwise is also given. Figure 4.2.a shows the temperature-dependent normalized resistivity plots of the doped samples. For the highest temperatures, the resistivity of all films had the same T^5 dependence, characteristic for phonon scattering. All curves, however, showed a resistivity minimum $\rho_{\min}$ at $T_{\min}$ between 10 K and 20 K.

The low-temperature resistivity showed the Kondo upturn which increased with the increasing amount of Co in the donor solution. The growing Kondo resistivity upturn with increasing Co donor solution concentration demonstrated that the metal film was effectively doped with localized magnetic impurities from the molecular monolayer. In order to quantitatively compare the resistivity data with Kondo theory, only the incremental resistivity $\Delta\rho_{\mathrm{norm}}(T)$ obtained by subtracting the $\rho_{\mathrm{norm}}(T)$ curve of the bare Au film from all other $\rho_{\mathrm{norm}}(T)$ curves is considered. As seen in figure 4.2.a (also figure 4.1), the bare Au film data also showed a small low-temperature resistivity upturn, which was attributed to magnetic impurities (most likely Fe) in the 99.99% pure Au source material used, and to weak localization and electron-electron interactions, which can also contribute to a temperature-dependent part of the resistivity [17, 18]. As these contributions should be the same for all samples studied, $\Delta\rho_{\mathrm{norm}}(T)$ was expected to only reflect the effect of molecular spin doping.

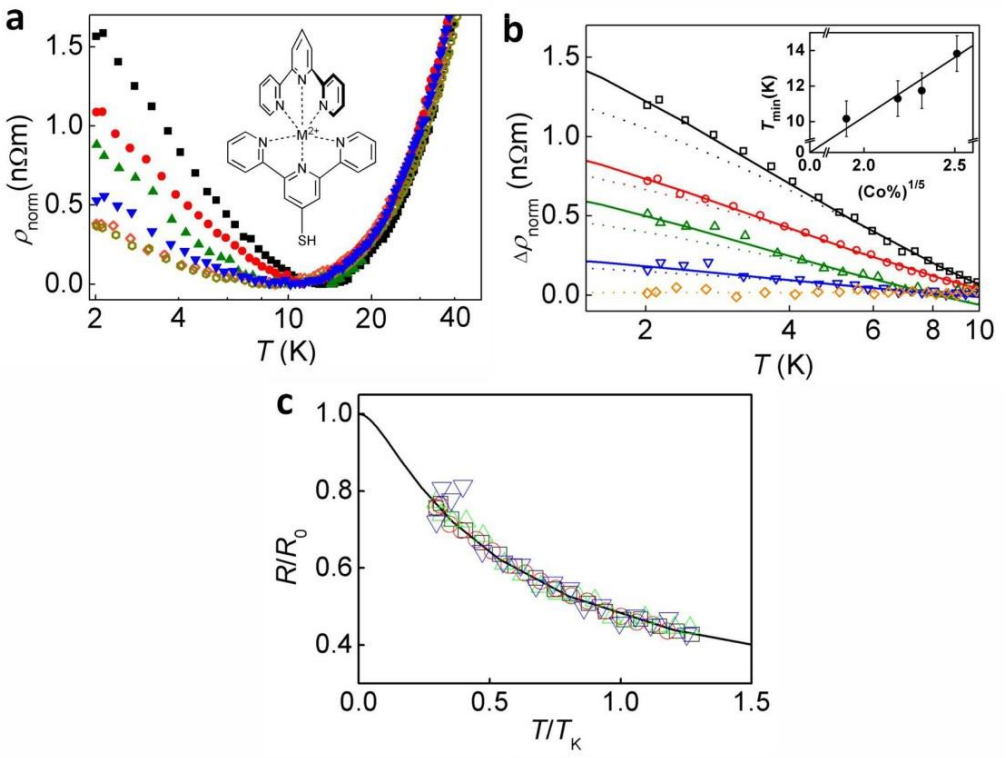

Figure 4.2 Kondo effect. (a) Temperature dependence of the normalized resistivity, $\rho_{\mathrm{norm}}(T) = \frac{\rho(T)-\rho_{\mathrm{min}}}{\rho(150\mathrm{K})-\rho_{\mathrm{min}}} \times \rho_{\mathrm{Au}}(150\ \mathrm{K})$ of a (99.99%) pure Au film (green hexagons), and the same Au film with inserted molecular monolayers made from mixed Co complex[x%]/Zn complex[(100-x)%] solutions with x = 0 (orange diamonds), 25 (blue down triangles), 50 (green up triangles), 67 (red dots), and 100 (black squares). Inset: structure of metal terpyridine complex, with "M" being either Co or Zn. (b) Data of (a) with the bare Au film curve subtracted. The solid curves are fits to NRG theory [19-21] and the doted curves are fits to an expression by Hamann [22]. Inset: T_{min} values of the resistivity minima ρ_{min}, showing (Co%)$^{1/5}$ dependence. (c) Normalized experimental data and NRG theory for S= ½.

Figure 4.2.b shows the thus obtained $\Delta\rho_{\mathrm{norm}}(T)$ curves, fitted to the exact numerical renormalization-group (NRG) theory for a S = ½ Kondo system [19-21]. We found T_K= 6.8 $\pm$0.2K for all curves, and R_0 of 0, 0.05, 0.14, 0.18, and 0.30 ($\pm$0.01) nΩm, for Co complex concentrations of 0%, 25%, 50%, 67% and 100%,

respectively. The $\Delta\rho_{\mathrm{norm}}(T)$ curves were also fitted to the self-consistent perturbative theory of Hamann [22] in the range $T > T_K$:

$$\Delta\rho = \frac{2\pi c}{ne^2 k_F}\left\{1 - \ln\left(\frac{T}{T_K}\right) \times \left[\ln^2\left(\frac{T}{T_K}\right) + S(S+1)\pi^2\right]^{-1/2}\right\} \qquad 4.1)$$

where c is the magnetic impurity concentration, n the electron density and k_F the Fermi wave vector of the host metal, and S a value reflecting the total impurity spin. For all curves, we found s = 0.45. This is close to the free electron spin of ½. It should be noted that the Hamann expression is the result of a perturbative theory, and therefore not exact below T_K. We have added a fit with the exact numerical renormalization group (NRG) theory, demonstrating that Hamann's theory (dotted curves) and NRG (solid curves) indeed differ for $T < T_K$ (figure 4.2.b). However, the difference was smaller than ~10-20%. Therefore we assume that the concentration derived from the Hamann expression gave a reasonable indication of the actual impurity concentration. We found impurity concentrations of 0, 123, 356, 507, and 786 ($\pm$10) ppm, for Co complex concentrations of 0%, 25%, 50%, 67% and 100%, respectively. The inset of figure 4.2.b is consistent with a T_{min} scaling with the Co concentration as $(\mathrm{Co\%})^{1/5}$, as expected for a Kondo system of non-interacting impurities [23]. In figure 4.2.c the experimental data with both normalized temperature and resistivity values were compared with the NRG result for S =1/2, showing very good agreement. The R_0 values obtained from the NRG fits and the impurity concentrations derived from the Hamann fits, were found to be directly proportional to the Co complex concentration in the donor solution (figure 4.3). This not only demonstrated that by mixing the Co and Zn complexes in solution we can effectively control the magnetic impurity concentration, but also confirmed that the Co complex:Zn complex ratio *in the monolayer* was the same as the ratio in the donor solution. This was also confirmed by XPS measurements (see Section 4.4.C). Importantly, no sign of saturation of the impurity concentration was observed, implying that no clustering of magnetic dopant atoms occurs even for the highest concentrations studied. The 786 $\pm$ 10 ppm concentration found for the 100% Co sample corresponded reasonably well with the ~10^3 ppm concentration expected from the monolayer coverage (see Section 4.4.B).

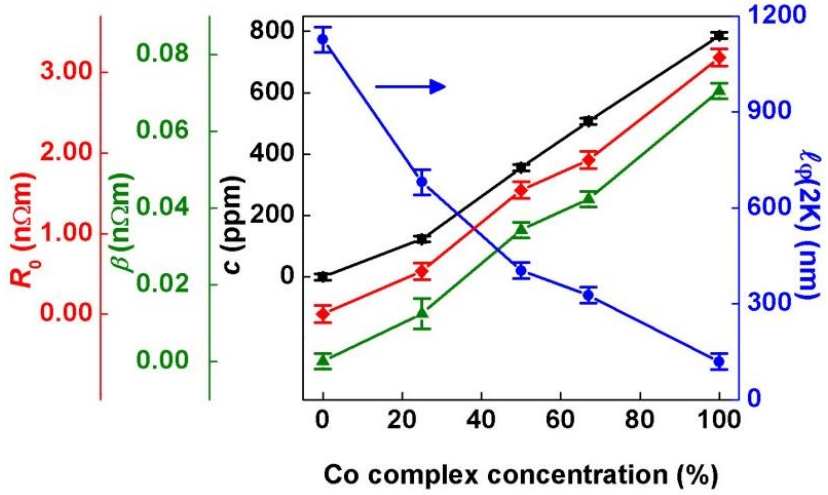

Figure 4.3 Tunable molecular spin doping. Resistivity at unitary limit, R_0 (red diamonds), obtained from the fits to NRG theory; magnetic impurity concentration, c (black squares), derived from the fits to Hamann expression; value of β (green triangles) in Eq. (1) obtained from the slope at T_K = 6.8 K of the data plotted in Fig. 1b; phase coherence length, l_ϕ(2 K) (blue dots), derived from the fits to Eq. (3) in Fig. 3b, versus the Co complex concentration in the donor solution.

In the Kondo regime, i.e. in the case of non-interacting magnetic impurities, and at temperatures above and around T_K, the resistivity increase was well described by

$$\Delta\rho = -\beta \ln(T)\,, \qquad (4.2)$$

where β is a positive coefficient with a magnitude that depends on the host material and is proportional to the magnetic impurity concentration [18]. The β values were obtained from the data in figure 4.2.b, by taking the slope at T_K = 6.8 K, and are also plotted in figure 4.3. β was indeed directly proportional to c (and hence to the Co complex concentration). Therefore it was concluded that up to the highest impurity concentration of 786 ($\pm$10) ppm, it was still in the Kondo regime. This is a significant finding, because pure Kondo behaviour has never been reported for such high impurity concentrations in Au (as to the best of our knowledge). In other studies on Au/impurity systems [24, 25], for similar or lower concentrations, the onset of impurity-impurity (RKKY) interaction was sometimes

put forward to explain deviations from the behaviour observed at the highest impurity levels. This work, however, suggested the absence of inter-impurity interactions up to very high concentrations.

Our molecular spin doping scheme thus allowed the creation of a system of non-interacting magnetic impurities at a doping level very hard to achieve with alternative methods. A concentration of 786 $\pm$ 10 ppm corresponds to a mean inter-impurity distance of ~3 nm (see Section 4.4.D). This value was compared to the (diffusive) Kondo length scale, l_K, which has been proposed as a measure for the extension of the Kondo cloud [26]:

$$l_{\mathrm{K}} \sim \sqrt{\frac{\hbar D}{k_{\mathrm{B}} T_{\mathrm{K}}}}\,, \tag{4.3}$$

where $\hbar$ is the reduced Planck's constant, *D* the diffusion constant and k_{B} the Boltzmann constant. The diffusion constant $D = \frac{1}{\rho e^2 \nu}$, where ρ is the residual resistivity, e is the elementary charge and ν is the density of states at the Fermi level for gold. With T_K = 6.8 K we found l_K~ 23 nm, about one order of magnitude larger than the mean inter-impurity distance derived above. We thus concluded that the Kondo length (at least in this case) is not a good indicator for the onset of impurity coupling, as pure Kondo behaviour for mean inter-impurity distances well below l_K was continued to be observed. A similar conclusion was reached in earlier studies on Au(Fe) [18], although for much lower impurity concentrations than described here. The Kondo screening cloud predicted by the basic Kondo model is in the order of microns. However, such a long characteristic length scale has never been observed experimentally. At the moment, the reason is theoretically still under debate. According to reference [27], the Kondo length should appear as a crossover scale. It can appear either when one probes the dependence of physical quantities a distance from the impurity or when the impurity is embedded in a finite size structure. The detection of Kondo screening cloud is difficult because it is very large. To see it, one must look for a crossover at large distances but at these distances the effects are weak, precisely because the distances are so large.

4.3.2 Magnetic field dependence of resistivity

In order to verify our method in an independent way, low-temperature magnetoresistance (MR) measurements were also performed.

Figure 4.4.a shows the normalized MR values $\frac{[\Delta R_{\square}(B)-\Delta R_{\square}(0)]}{R_{\square}(0)R_{\square}(B)} \equiv -\Delta\sigma$ for different Co complex concentrations at 2 K [28]. A minimum at B = 0 was found for all curves, attributed to weak anti-localization (WAL). Weak localization (WL) and WAL are quantum corrections to the resistivity due to coherent back scattering in disordered systems [2] (for details, see Chapter 3). In case of weak spin-orbit coupling, the effect leads to an enhanced probability for the carriers to return to the point of origin, i.e. WL, and therefore to an increased resistivity. However, in solids with large spin-orbit coupling, as for Au in our case, WAL occurs, which gives a negative quantum contribution to the resistivity. WL and WAL are suppressed by a (perpendicular) magnetic field, lifting time-reversal symmetry, which provides a way to derive the carrier phase coherence length, l_ϕ [2]. The normalized MR curves of figure 4.4.a showed clear WAL minima, with a width that strongly increased with Co complex concentration.

In Figure 4.4.b the low-field data were fitted with the theory of Hikami, Larkin and Nagaoka [29]

$$\Delta\sigma(B) = -\frac{e^2}{2\pi^2\hbar\hbar}\left[f\left(\frac{B_1}{B}\right) - \frac{3}{2}f\left(\frac{B_2}{B}\right) + \frac{1}{2}f\left(\frac{B_{\phi_\emptyset}}{B}\right)\right] \quad (4.4)$$

where $f(x) = \psi\left(x+\frac{1}{2}\right) - \ln(x)$ with $\psi(x)$ the digamma function, B_1, B_2 and B_ϕ are characteristic magnetic fields defined by $B_1 = B_e + B_{s.o.} + B_s$, $B_2 = B_i + \frac{4}{3}B_{s.o.} + \frac{2}{3}B_s$ and $B_\phi = B_i + 2B_s$, referring to contributions from elastic (e), inelastic (i), spin-orbit (s.o.) and magnetic (s) scattering. At low magnetic fields, B_1 was dominated by $B_{s.o.}$, which is independent of magnetic field. The same holds for B_2, leaving B_ϕ as the parameter determining the shape of the WAL curves. From B_ϕ we could derive the phase coherence length via $l_\phi(2\text{ K}) = \sqrt{\frac{\hbar}{4eB_\phi(2\text{ K})}}$ for the different Co complex concentrations, which are also plotted in figure 4.3. The phase coherence length monotonically decreased from 1.1 μm to 150 nm with increasing Co complex concentration. Assuming that the inelastic scattering

contribution to be the same for all samples, the decrease of l_ϕ with increasing Co complex concentration could be fully attributed to enhanced (phase-breaking) spin scattering off the introduced magnetic impurities. These results thus provided independent evidence that effectively tuning the magnetic impurity concentration via our molecular spin doping scheme was successful.

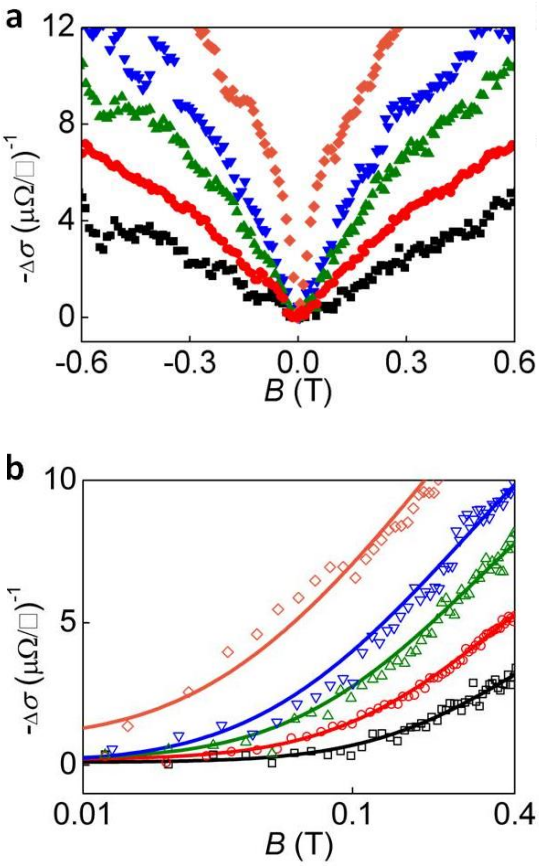

Figure 4.4 (a), Magnetoresistance $\frac{[\Delta R_\square(B)-\Delta R_\square(0)]}{R_\square(0)R_\square(B)} \equiv -\Delta\sigma$ at 2K for the same Au film with inserted molecular monolayers made from mixed Co complex[x%]/Zn complex[(100-x)%] solutions with x =0 (orange diamonds), x = 25 (blue down triangles), 50 (green up triangles), 67 (red dots), and 100 (black squares). (b) Data of (a) fitted to weak localization theory, Eq. (3), with B_e = 57 T and B_{so}= 0.13 T.

Conclusions

A conceptually novel and very easy approach to dope metal films with a tunable amount of magnetic impurities from a molecular monolayer was achieved. Kondo and magnetoresistance measurements demonstrated that the impurity concentration in the metal was directly proportional to the molecular spin dopant concentration in solution. Although up to now it was widely believed that inter-impurity coupling sets in at ~100 ppm levels, our molecularly doped impurity systems showed pure Kondo behaviour down to 2K at impurity levels as high as 786 $\pm$ 10 ppm. Therefore this technique can be used as a powerful way to reach unprecedented impurity concentrations, while avoiding undesired aggregation or segregation. This should pave the way for further study of spin phenomena that lie at the very heart of solid-state physics, such as the Kondo effect, RKKY interaction, spin glasses, and magnetic phase transitions.

4.4 Monolayer Characterization

A. Electrochemistry

Electrochemical measurements were performed with an AUTOLAB PGSTAT10 in a custom-built three-electrode setup with bare gold substrates as the working electrode, an Ag/AgCl reference electrode, and a platinum wire as counter electrode.

To determine the coverage of a monolayer of 100% Co complex on the Au surface, cyclic voltammetry measurements were performed, which are shown in figfigure 4.5. Measurements were done with an Au electrode covered with a monolayer of the Co complex in a 0.1 mM tetra-n-butylammonium hexafluorophosphate acetonitrile solution. A peak was observed around 0.375 V, which was attributed to the redox activity of the Co^{2+} ion. Integration of the *I-V* curves gives the total charge *Q*, from which the surface coverage Γ of the monolayer can be determined by $\Gamma = \frac{Q}{nFA}$, where *n* is the number of electrons per mol of reaction, *F* the Faraday constant and *A* the surface area. By taking *I-V* curves for different scan rates, *Q* could be determined as a function of the scan rate, as shown in figfigure 4.5.b. The independence of Q on the scan rate shows

that it is a surface-confined process, as is expected for a monolayer [30]. $\Gamma = 5.0 \times 10^{-11}$ mol cm^{-2} was found.

B. Calculations for maximum impurity concentration:

The maximum amount of Co complexes (n_{Co}) on the 6.8×2.2 mm^2 Si/300nmSiO_2/5nmAu substrate surface was obtained from $n_{Co} = \Gamma S N_A$, where S is the surface area of the substrate and N_A is the Avogadro constant. The amount of gold atoms (n_{Au}) in the 5nm Au layer was estimated as $n_{Au} = \frac{\rho V}{M} N_A$, where ρ is the density of Au at room temperature, V is the volume of the gold film and M is the molar mass of Au. The maximum impurity concentration in ppm is given by $c = 1 \times 10^6 \frac{n_{Co}}{n_{Au}} \approx 10^3$ppm.

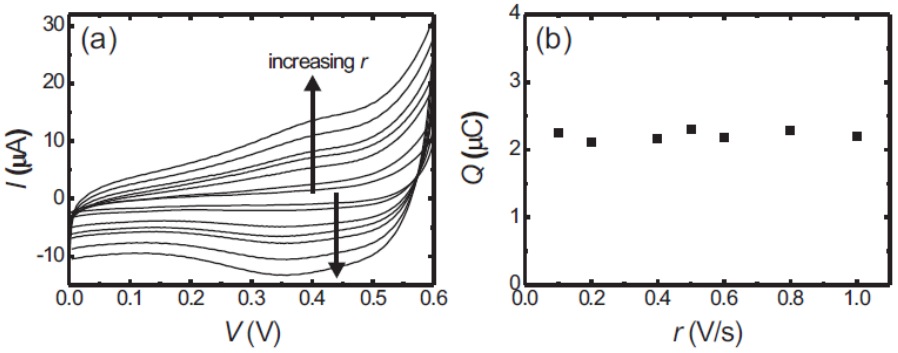

Figure 4.5 Cyclic voltammetry measurements on a monolayer of the Co complex. (a) Current I vs. voltage V for different scan rates r (the direction of the arrows denote increasing r) and (b) charge Q vs. scan rate, obtained from the curves in (a).

C. X-ray photoelectron spectroscopy (XPS) measurements

XPS analysis was carried out on the following samples:

SA1) Si/SiO_2(300 nm)/Au(2.5 nm)/Co-complex SAM;

SA2) Si/SiO_2(300 nm)/Au(2.5 nm)/1:1 Co:Zn-complexes SAM ;

SA3) Si/SiO_2(300 nm)/Au(2.5 nm)/Co-complex SAM/Au(2.5 nm) ;

SA4) Si/SiO_2(300 nm)/Au(2.5 nm)/1:1 Co:Zn-complexes SAM/Au(2.5 nm).

Figure 4.6 shows the XPS spectra of the SA1 and SA2 after subtraction of a linear background. For the Au/SAM samples, *i.e.* SA1 and SA2, a comparison of the Co(2*p*) intensity relative to the Au(4*f*) intensity from the substrate showed that the Co-coverage for the pure Co-compound was a factor of 1.9 higher than that of the 1:1 mixture of Co- and Zn-compounds (the Co(2*p*) spectra are shown in figure 4.6). This is in good agreement with the expected reduction of a factor of two, certainly considering that the signals were rather weak. The integrated Co(2*p*) intensity was about 1% of the integrated background intensity in the Co(2*p*) region for SA1. Using the convention that a signal should exceed three times the standard deviation of the background noise (proportional to the square root of the background signal) such that its detection is 99% certain, we find that this Co(2*p*) signal amounts to about eight times the detection limit.

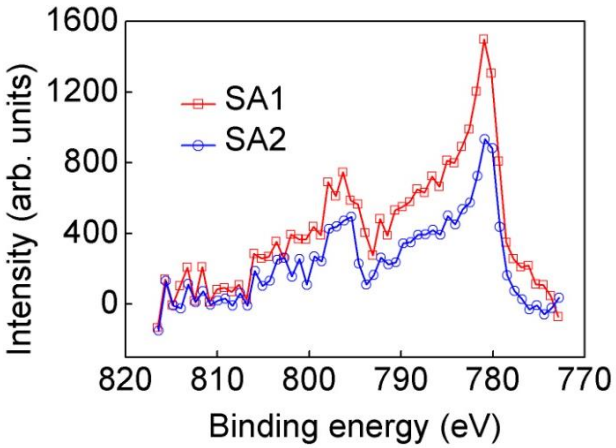

Figure 4.6 Co(2p) signals of SA1 and SA2, after subtraction of a linear background.

We found a Co:Zn ratio of 1:1.1 for the nominally 1:1 mixture (SA2), based on the integrated intensities of the Co(2*p*) and Zn($2p_{3/2}$) lines, and using atomic sensitivity factors corrected for the transmission function of the XPS analyzer. This was again fully consistent with expectations. The binding energies of both Co- and Zn core levels were in agreement with those of charged species in compounds such as oxides.

For Au/SAM/Au samples, i.e. SA3 and SA4, the Co- and Zn-signals were strongly attenuated by the top Au layer. Due to the large electron density in Au, even very thin Au layers lead to a significant reduction of core-level peaks originating from buried elements. The Co(2*p*) signal of SA3 is about two times the detection limit of the measurement. For such weak signals, it was not possible to make solid, quantitative claims concerning either the atomic coverage or the chemical state (related to the binding energy). For the 1:1 mixture, i.e. SA4, the Co- and Zn-peak intensities were essentially at the detection limit.

D. Estimate for mean distance between spin impurities:

From above, it is clear that the Co concentration '*c*' (in ppm) is proportional to the Co complex molecular coverage 'Γ' (in mol/cm^2). So the molecular coverage corresponding to $c = 786 \pm 10$ ppm can be estimated by $\Gamma_{786\mathrm{ppm}} \approx \frac{786}{1000}\Gamma_{1000\mathrm{ppm}} = 3.9 \times 10^{-11}\ \mathrm{mol\ cm^{-2}}$. This means one molecule per 4 nm^2. Assuming all the spin impurities are distributed in a 2D plane with close packing, the mean inter-impurity distance is approximately $\sqrt{2 \times 4\mathrm{nm}^2} \approx 3$ nm. If we assume a homogenous (3D) distribution through the whole film, we find a very similar number as the film thickness is of same order as the inter-impurity distance.

E. Sheet resistance of all samples for magnetoresistance measurement:

The sheet resistance of all samples at 150K for magnetoresistance measurement is given in

table 1. The standard deviation of the distribution of sheet resistances of these samples was 29.5 **Ω/□.** The variation in sheet resistance may imply slight differences in the morphology of the gold films, which may contribute to both the inelastic and elastic scattering of the conduction electrons [2, 28]. (note that all samples had the same nominal Au/SAM/Au composition, while the ration of Co- to Zn-complexes was varied within the SAM). In spite of the modest variation in sheet resistance, the shape of the magnetoresistance curves was dominated by magnetic scattering introduced via the Co complexes.

Table 1 Sheet resistance at 150K of all samples for magnetoresistance measurement.

Co-complex concentration (%)	0	25	50	67	100
Sheet resistance at 150K (Ω/□)	106.9	152.3	172.8	173.0	177.9

References

[1] J. Kondo, "Resistance minimum in dilute magnetic alloys," *Prog. Theor. Phys.,* vol. 32, pp. 37-49, 1964.

[2] G. Bergmann, "Weak Localization and Its Applications as an Experimental Tool," in *50 Years of Anderson Localization*, E. Abrahams, Ed., ed: World Scientific, 2010.

[3] J. W. Loram, T. E. Whall, and P. J. Ford, "Resistivity of Some CuAuFe Alloys," *Phys. Rev. B,* vol. 2, pp. 857-874, 1970.

[4] B. de Boer, A. Hadipour, M. M. Mandoc, T. van Woudenbergh, and P. W. M. Blom, "Tuning of metal work functions with self-assembled monolayers," *Adv. Mater.,* vol. 17, pp. 621-625, Mar 8 2005.

[5] W. Chen, D. Qi, X. Gao, and A. T. S. Wee, "Surface transfer doping of semiconductors," *Prog. Surf. Sci.,* vol. 84, pp. 279-321, Sep-Oct 2009.

[6] J. C. Ho, R. Yerushalmi, Z. A. Jacobson, Z. Fan, R. L. Alley, and A. Javey, "Controlled nanoscale doping of semiconductors via molecular monolayers," *Nat. Mater.,* vol. 7, pp. 62-67, Jan 2008.

[7] W. P. Voorthuijzen, M. D. Yilmaz, W. J. M. Naber, J. Huskens, and W. G. van der Wiel, "Local Doping of Silicon Using Nanoimprint Lithography and Molecular Monolayers," *Adv. Mater.,* vol. 23, pp. 1346-1350, Mar 18 2011.

[8] E. C. P. Smits, S. G. J. Mathijssen, P. A. van Hal, S. Setayesh, T. C. T. Geuns, K. A. H. A. Mutsaers*, et al.*, "Bottom-up organic integrated circuits," *Nature,* vol. 455, pp. 956-959, Oct 16 2008.

[9] B. Lee, Y. Chen, F. Duerr, D. Mastrogiovanni, E. Garfunkel, E. Y. Andrei*, et al.*, "Modification of Electronic Properties of Graphene with Self-Assembled Monolayers," *Nano Lett.,* vol. 10, pp. 2427-2432, Jul 2010.

[10] T. Gang, M. D. Yilmaz, D. Atac, S. K. Bose, E. Strambini, A. H. Velders*, et al.*, "Tunable doping of a metal with molecular spins," *Nat Nano,* vol. 7, pp. 232-236, 04//print 2012.

[11] S. Kremer, W. Henke, and D. Reinen, "High-spin-low-spin equilibria of cobalt(2+) in the terpyridine complexes $Co(terpy)_2X_2 \cdot nH_2O$," *Inorg. Chem.,* vol. 21, pp. 3013-3022, 1982 1982.

[12] J. Park, A. N. Pasupathy, J. I. Goldsmith, C. Chang, Y. Yaish, J. R. Petta*, et al.*, "Coulomb blockade and the Kondo effect in single-atom transistors," *Nature,* vol. 417, pp. 722-725, Jun 13 2002.

[13] V. Madhavan, W. Chen, T. Jamneala, M. F. Crommie, and N. S. Wingreen, "Tunneling into a single magnetic atom: Spectroscopic evidence of the Kondo resonance," *Science,* vol. 280, pp. 567-569, Apr 24 1998.

[14] J. T. Li, W. D. Schneider, R. Berndt, and B. Delley, "Kondo scattering observed at a single magnetic impurity," *Phys. Rev. Lett.,* vol. 80, pp. 2893-2896, Mar 30 1998.

[15] D. Goldhaber-Gordon, H. Shtrikman, D. Mahalu, D. Abusch-Magder, U. Meirav, and M. A. Kastner, "Kondo effect in a single-electron transistor," *Nature,* vol. 391, pp. 156-159, Jan 8 1998.

[16] W. G. van der Wiel, S. De Franceschi, T. Fujisawa, J. M. Elzerman, S. Tarucha, and L. P. Kouwenhoven, "The Kondo effect in the unitary limit," *Science,* vol. 289, pp. 2105-2108, Sep 22 2000.

[17] E. L. Altshuler, B. L. Altshuler, and A. G. Aronov, "Quasielastic electron electron-scattering and anomalous magnetoresistance," *Solid. State. Commun.,* vol. 54, pp. 617-620, 1985 1985.

[18] G. Chen and N. Giordano, "Thickness dependence of the Kondo effect in AuFe films," *Phys. Rev. Lett.,* vol. 66, pp. 209-211, 1991.

[19] T. A. Costi, A. C. Hewson, and V. Zlatic, "TRANSPORT-COEFFICIENTS OF THE ANDERSON MODEL VIA THE NUMERICAL RENORMALIZATION-GROUP," *J Phys.-Condens. Mat.,* vol. 6, pp. 2519-2558, Mar 1994.

[20] F. Mallet, J. Ericsson, D. Mailly, S. Uenluebayir, D. Reuter, A. Melnikov*, et al.*, "Scaling of the low-temperature dephasing rate in Kondo systems," *Phys. Rev. Lett.,* vol. 97, Dec 1 2006.

[21] C. Bauerle, F. Mallet, F. Schopfer, D. Mailly, G. Eska, and L. Saminadayar, "Experimental test of the numerical renormalization-group theory for inelastic scattering from magnetic impurities," *Phys. Rev. Lett.,* vol. 95, Dec 31 2005.

[22] D. R. Hamann, "New Solution for Exchange Scattering in Dilute Alloys," *Phys. Rev.,* vol. 158, pp. 570-580, 1967.

[23] P. L. Taylor and O. Heinonen, *A Quantum Approach to Condensed Matter Physics*. Cambridge: Cambridge University Press, 2002.

[24] A. Mordijck, I. Deckers, and M. Labro, "Transition in the overcompensated multichannel Kondo alloy au-v - susceptibility and resistivity data," *J. Magn. Magn. Mater.,* vol. 104, pp. 2081-2082, Feb 1992.

[25] W. Wei, R. Rosenbaum, and G. Bergmann, "Magnetic scattering in AuCo and AgCo with weak localization," *Phys. Rev. B,* vol. 39, pp. 4568-4571, Mar 1 1989.

[26] N. O. Birge, D. C. Ralph, O. Ujsaghy, G. Zarand, A. Zawadowski, V. Chandrasekhar*, et al.*, *Kondo Effect and Dephasing in Low-Dimensional Metallic Systems*. Dordrecht: Kluwer Academic Publishers, 2000.

[27] I. Affleck, "The Kondo screening cloud: what it is and how to observe it," *ArXiv.org,* vol. 0911.2209v2, 2010.

[28] G. Dumpich and A. Carl, "Anomalous temperature-dependence of the phase-coherence length for inhomogeneous gold-films," *Physical Review B,* vol. 43, pp. 12074-12077, May 15 1991.

[29] S. Hikami, A. I. Larkin, and Y. Nagaoka, "Spin-orbit interaction and magnetoresistance in the 2 dimensional random system," *Prog. Theor. Phys.,* vol. 63, pp. 707-710, 1980 1980.

[30] F. Beck, "Cyclic voltammetry—simulation and analysis of reaction mechanisms. By David K. Gosser, Jr., VCH, New York 1993, xi, 154 pp., hardcover, DM 124.00, ISBN 3-527-28226-2, disks included (5 1/4" and 3 1/2")," *Electroanalysis,* vol. 7, pp. 298-298, 1995.

Chapter 5

Tuning the Kondo effect in thin Au films by depositing a thin layer of Au on molecular spin-dopants

In the previous Chapter, we discussed the Kondo upturn (increase of the resistivity with decreasing temperature for T<10K) in ultrathin Au films covered with the self-assembled monolayers (SAMs) of cobalt(II) terpyridine complexes (Co complexes), and showed that it was much stronger when a thin Au layer was sputter deposited on top. In this Chapter, tuning of the Kondo effect in thin Au films with SAMs of Co complexes is addressed. The tuning is realized by altering the ligand structure around the Co^{2+} ions of the molecular complex by means of depositing a thin Au capping layer on top of the SAMs either by magnetron sputtering (more energetic) or e-beam evaporation (softer). It was shown that the Kondo effect is slightly enhanced with respect to that of the uncapped film when the cap is deposited by evaporation, and significantly enhanced when magnetron sputtering was used. The increase in the Kondo effect was related to the increase in the impurity-electron interaction. The increased interaction was attributed to the change in the electronic environment of the Co^{2+} ion as a result of partial destruction of the terpyridine ligands around the Co^{2+} ion upon Au deposition. The study shows that it is possible to change the strength of the impurity-host interaction in such systems with depositing a thin layer of Au on top the molecules, by varying the kinetic energy distribution of the Au atoms arriving at the surface. This allows for tuning of the magnetic impurity states, e.g. the spin quantum number, binding energy with respect to the host Fermi energy, and orbital overlap via the ligand structure around the ions.

This chapter has been published as D. Ataç, T. Gang, M. D. Yilmaz, S. K. Bose, A. T. M. Lenferink, C. Otto, M. P. de Jong, J. Huskens and W. G. van der Wiel, *Nanotechnology* **24** 375204 (2013).

5.1 Introduction

As discussed in Chapter 4, the interaction between conduction electrons and isolated magnetic impurities may lead to very rich physics. Particularly, the Kondo effect has been studied extensively over the last decades as it provides a prototype system for many-body correlation effects [1-3].

In order to investigate such electron-impurity interactions over a wide range of concentrations, the impurities must be introduced inside the host homogeneously, i.e. without clustering or segregation. In Chapter 4, this was achieved by molecular doping of a thin Au film with magnetic impurities, reaching very high concentrations (~800 ppm) without any effects of agglomeration [4]. Our method relied on inserting isolated localized magnetic impurities into a gold film from a self-assembled monolayer (SAM) of metal terpyridine complexes; Co(tpy)(tpy-SH) (Co complex) containing a metal ion with an unpaired spin (Co^{2+}). Temperature-dependent resistance measurements of the Au films doped with Co complexes showed an increase in the resistivity at low temperatures (Kondo upturn) as was described in Chapter 3 and 4.

The molecular magnetic doping method enables investigating the Kondo effect by changing the magnetic impurity concentration in a thin film. It may also allow for manipulating the Kondo temperature (T_K) (described in Chapter 3 and 4), as it was investigated in this study. There are reports where the T_K was tuned in organic-inorganic hybrid systems through a single atom or organic molecule and probed via an STM tip. In these studies, the T_K was manipulated by altering the spin-orbit coupling in several ways, such as by changing the number of molecules around a central magnetic molecule [5], by tuning the symmetry of the ligand field through the local coordination to the substrate [6], or by modifying the relative coupling strength via changing the molecule to electrode distance in a break junction [7]. In contrast to those studies, we tune the T_K in a thin film by deposition of a very thin layer (5 nm) of Au on top of the molecules (Au capping) with two different deposition methods: e-beam evaporation and magnetron sputtering. Sputter-deposition of the Au capping layer was expected to (partially) destroy the organic ligands of the organometallic complexes, due to the relatively high kinetic energy of the arriving Au atoms. It is known that the kinetic energy per deposited metal atom in thermal evaporation is around 0.3 eV, whereas in

sputtering it is on the order of 40 eV, *i.e.* ~130 times larger [8-10]. On the other hand, typical molecular bond strengths are on the order of ~2 eV. Therefore, it was expected that sputtering would cause damage to the molecular structure, while with evaporation the molecular bonds would remain largely intact. It should be noted that a change in the bonds directly involving the Co^{2+} ions would have a more drastic effect on the electronic environment of these ions than a change on the ligand further away from the Co^{2+} center. Such a dramatic change at the Co site, possibly involving ligand atoms being replaced by Au atoms, might lead to an increase in the strength of the interaction between the impurity spin and conduction electrons and improve the electronic coupling between the Co-impurities and the Au host, which would result in an increased Kondo upturn and higher T_K. In addition to the change of the Co coordination sites, the geometrical structure of the thin film can also play a role. For instance, monolayers on Au without capping sit on ~5 nm Au, whereas the capped monolayers are sitting in the middle of Au with the same thickness. Therefore, the electrons may have a larger probability for colliding with Co center.

5.2 Experimental Methods

We inspected the low temperature dependence of the resistivity and magnetoresistance on the monolayers (ML) of Co complexes assembled on Au without any Au cap: ML/Au(~18nm) , with sputter deposited Au cap: sp-Au(~5nm)/ML/Au(~5nm), with e-beam evaporated Au cap: eb-Au(~5 nm)/ML/Au(~5nm) (where “sp-Au” and “eb-Au” stand for “sputtered Au cap” and “e-beam evaporated Au cap” ,respectively) and the bare Au film before ML formation on top of it: Au(~18 nm). The samples were prepared on SiO_2 (300 nm)/Si substrates for electrical measurements and on transparent CaF_2 substrates for Raman spectroscopy measurements. The Au capped monolayers sp-Au/ML/Au and eb-Au/ML/Au were sandwiched between two Au layers of ~5nm. The sputter-deposited bottom Au films were prepared in the same sputtering run. The films consisted of non-connecting islands and became conducting only after the depositions of capping layers on top of the formed monolayers. The bare Au(~18 nm) and the ML/Au(~18 nm) samples are actually the same sample before and

after the ML formation. The magnetron sputtering conditions for bottom Au and sputtered cap depositions were the same: at room temperature in 6.6×10^{-3} mbar Ar pressure with 60 W power (at 440 V) from an Au (99.99%) target. The Au target was cleaned via 1 min pre-sputtering before every deposition run. The sheet resistances of the samples at 150K were 188 Ω/sq, 353 Ω/sq, 259 Ω/sq and 332 Ω/sq for Au, ML/Au, eb-Au/ML/Au and sp-Au/ML/Au, respectively.

The SAMs of Co complexes on the Au films were formed by immersing the Au films into 1 mM solutions of Co(tpy)(tpy-SH) complexes in acetonitrile overnight at room temperature, as was described in Chapter 3. The Au capping was performed right after monolayer preparation to avoid contamination from prolonged exposure to ambient conditions. Capping by sputtering was explained above, while the capping by e-beam evaporation was performed at room temperature with an e-beam emission current of 220 mA and an acceleration voltage of 10 kV (2.2 kW power), at 0.2 Å/s deposition rate.

The effect of Au capping on the molecular structure of the complex and the electronic environment of the Co^{2+} core ion was investigated by X-ray absorption spectroscopy (XAS) and surface-enhanced Raman spectroscopy (SERS).

5.3 Results and Discussion:

5.3.1 Electron transport and magnetoresistance measurements

Electron transport measurements were performed using a physical properties measurement system (PPMS, Quantum Design) with an excitation current of 3 μA.

Figure 5.1.a shows the temperature dependence of the resistivity of samples consisting of *(i)* a bare Au film (Au), *(ii)* a monolayer of Co(tpy)(tpy-SH) on the same Au film without additional Au capping layer (ML/Au), and monolayers with *(iii)* sputtered (sp-Au/ML/Au) and *(iv)* e-beam evaporated Au caps (eb-Au/ML/Au). Although the sheet resistances were intended to be the same, there were sample-to-sample resistivity variations. To make a direct comparison possible, the resistivity values were normalized in the same way as in Chapter 4

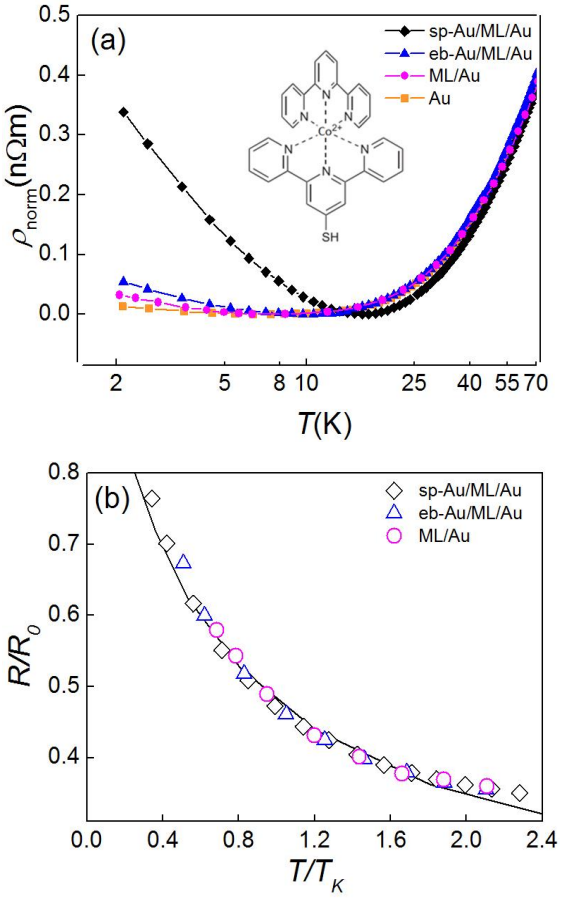

Figure 5.1 (a) Normalized resistivity versus temperature for a 99.99% pure gold film: Au (orange squares), the identical gold film with a monolayer of Co(tpy)(tpy-SH) complexes: ML/Au (pink circles), Co(tpy)(tpy-SH) complexes capped with a thin layer of e-beam evaporation deposited Au: eb-Au/ML/Au (blue triangles) and sputter-deposited Au: sp-Au/ML/Au (black diamonds). Inset: structure of the Co(tpy)(tpy-SH) complex. (b) Normalized resistivity plotted against normalized temperature with the contribution of the bare gold film subtracted for temperatures below T_{min}. The solid line is the fit to NRG theory for S=1/2 Kondo system. Extracted Kondo temperatures are 3 K, 4.2 K and 6.2 K for ML/Au, eb-Au/ML/Au and sp-Au/ML/Au samples, respectively.

according to $\rho_{\mathrm{norm}}(T\frac{\rho(T)-\rho_{\mathrm{min}}}{\rho(150\mathrm{K})-\rho_{\mathrm{min}}}\times\rho_{\mathrm{Au}}(150\ \mathrm{K})$, where ρ_{min} is the minimum resistivity value of each curve and ρ_{Au}(150K) is the resistivity of the Au film at 150K [4].

The general behavior of the curves was consistent with the results of Chapter 4. For the highest temperatures, the resistivity of all films exhibit the same T^5 dependence, which is characteristic of phonon scattering. All curves, however, show a resistivity minimum ρ_{min}, and an increase in resistivity with decreasing temperature.

As can be seen in figure 5.1.a, the monolayer with sputter-deposited Au cap shows by far the largest upturn, followed by the monolayer capped with evaporated Au, the monolayer without Au cap, and finally the bare Au sample with the same thickness. The upturn in the bare Au film was attributed to magnetic impurities (the most abundant being iron) in the 99.99% pure gold source material we used, and to weak anti-localization and electron–electron interactions, which can also contribute to a temperature-dependent part of the resistivity [4].

We obtained T_{min} values of 6.4 K for Au, 8.4 K for ML/Au and 9.7 K for eb-Au/ML/Au, and 16 K for sp-Au/ML/Au. The Kondo temperature for each curve was extracted from fits to the numerical renormalization-group (NRG) theory [11-13] (figure 5.1.b). The extracted T_K, from small to large values, were 3 K for the ML/Au, 4.2 K for eb-Au/ML/Au, and 6.2 K for sp-Au/ML/Au. The value of the Kondo temperature corresponds to the binding energy of the correlated conduction electron-impurity state [14]. In other words, the Kondo temperature of the system can be considered as a measure of the interaction strength between the magnetic impurity and the conduction electrons. Therefore, the higher T_K observed for eb-Au/ML/Au and the highest T_K for sp-Au/ML/Au is indicative of the stronger interaction between the spin of the Co^{2+} ion and the conduction electrons.

There could be two possibilities for this: One is the location where the complexes reside; on the surface for the ML/Au case and in the middle of the film for the eb-Au/ML/Au and sp-Au/ML/Au cases, in the sense that the Co^{2+} ion and Au atoms would physically be closer, so that the electrons have a larger

probability for colliding with Co, certainly if the film thickness is on the order of (or smaller than) the mean free path, which is the case here. The second is the change in the electronic environment of the Co^{2+} ions as a result of the Au deposition. However, as the following analysis will show, the first possibility can explain the higher T_K only for the eb-Au/ML/Au sample, because the molecular structure was not significantly altered upon Au evaporation. On the other hand, for the sp-Au/ML/Au sample, evidence of changes in the coordination sites of Co, and therefore a modification of the Co^{2+} electronic environment, were obtained. Since the measurements of the eb-Au/ML/Au sample showed that the location of the molecules has a only small effect on the Kondo upturn, it can be concluded that the change in electronic environment of Co^{2+} causes the highest T_K for the sputtered sample (see discussion below).

In order to confirm the increased interaction between impurity spins and conduction electrons in Au-capped monolayers, the electron phase coherence length (l_φ) was determined from weak anti-localization (WAL) (see Chapter 3 and Chapter 4) feature in the magnetoresistance measurements (figure 5.2). Weak anti-localization can be suppressed by a magnetic field (perpendicular to the thin film plane), lifting time-reversal symmetry, which provides a way to derive the carrier phase coherence length, l_φ [15]. To extract l_φ ,the low-field magnetoresistance curves were fitted to the theory of Hikami, Larkin and Nagaoka (figure 5.2.b) [16].

Figure 5.2.a shows the magnetoresistance curves at 2K. Each curve was normalized according to the equation $-\Delta\sigma \equiv \frac{[\Delta R_\square(B)-\Delta R_\square(0)]}{R_\square(0)R_\square(B)}$, as was described in Chapter 4.

A minimum at B = 0 T was observed for all curves, corresponding to weak anti-localization (WAL). The widths of the curves strongly increases from the bare Au film to the sputter capped monolayer. Figure 5.2.b shows the low-field part of the magnetoresistance data with the magnetic field in logarithmic scale. The solid lines are fits to the theory of Hikami, Larkin and Nagaoka [16]. The extracted l_φ values are 584 nm for Au, 453 nm for the ML/Au, 280 nm for eb-Au/ML/Au, and 132 nm for sp-Au/ML/Au. The decrease in l_φ for ML/Au compared to Au can be

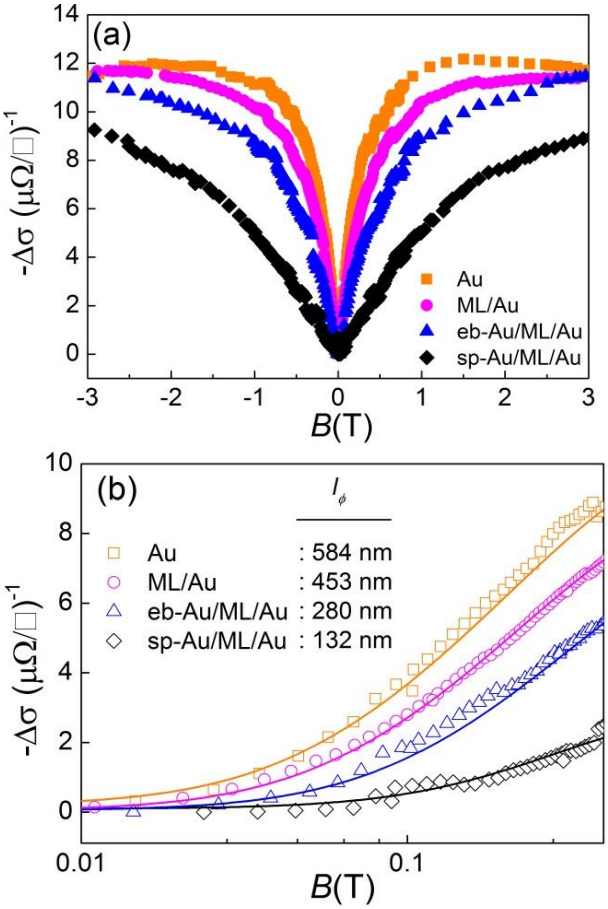

Figure 5.2 (a) Normalized magnetoresistance versus applied magnetic field B at 2K for ML/Au (pink circles), eb-Au/ML/Au (blue triangles) and sp-Au/ML/Au (black diamonds). (b) Data for values of B between 0.01 T and 0.4 T, re-plotted with a logarithmic B-axis. Solid lines are fits to weak localization theory. Inset: extracted phase coherence lengths.

related to the spin scattering off the magnetic impurities assembled on the Au film, which is consistent with the higher Kondo upturn.The even smaller value of l_φ in the sp-Au/ML/Au, compared to the eb-Au/ML/Au and ML/Au confirms the increase in spin scattering also observed in the Kondo upturn. These findings suggest that the electronic environment of the impurities is strongly affected by the different Au capping procedures. We will address this issue further in the following sections.

5.3.2 X-ray absorption spectroscopy (XAS) measurements

XAS is a powerful and surface-sensitive technique to characterize the element-specific electronic structure of materials [17]. Since the Au capping layers we used were very thin, it was still possible to probe the spectral features of the molecules. The details of the XAS measurements can be found in Chapter 3.

The experimental setup at beamline D1011 of MAX-lab, Lund, Sweden contained a sample preparation chamber, separated from the measurement chamber with a vacuum valve, which was used for *in-situ* deposition of Au by thermal evaporation using a W filament wire coated with Au. The base pressure of the preparation chamber was 10^{-10} mbar and the pressure during the Au deposition was $\sim 5 \times 10^{-9}$ mbar. All XAS spectra were measured at room temperature in total electron yield mode, with a probing depth of about 10 nm. The backgrounds for correction of the Co L-edge, C K-edge and N K-edge spectra were measured from a clean, *in-situ* deposited Au film on a Si substrate, and removed from the XAS spectra.

The SAM of Co complexes were formed on 20 nm Au films (ML/Au), which is thick enough to block signal contributions from the Si substrate. The samples were loaded into the load-lock of the UHV system immediately after monolayer formation to avoid contamination resulting from prolonged exposure to air. After measuring the XAS and photoemission spectra (PES) spectra of the ML/Au, several *in-situ* Au evaporation steps were performed at room temperature. The evaporation and measuring procedure was repeated four times in order to see the effect of increasing Au evaporation on the spectra. The increase of the Au coverage after each deposition was estimated to be around 0.25 nm by evaluating the attenuation of the C1s peak (originating from the monolyers) in PES measurements. A background signal, measured from a clean Au layer on top of Si, was subtracted from all XAS measurements. It should be noted that the signal to background ratio in the spectrum taken after the 4^{th} evaporation (evap. 4) was very low, such that background contributions may not be completely removed from the data.

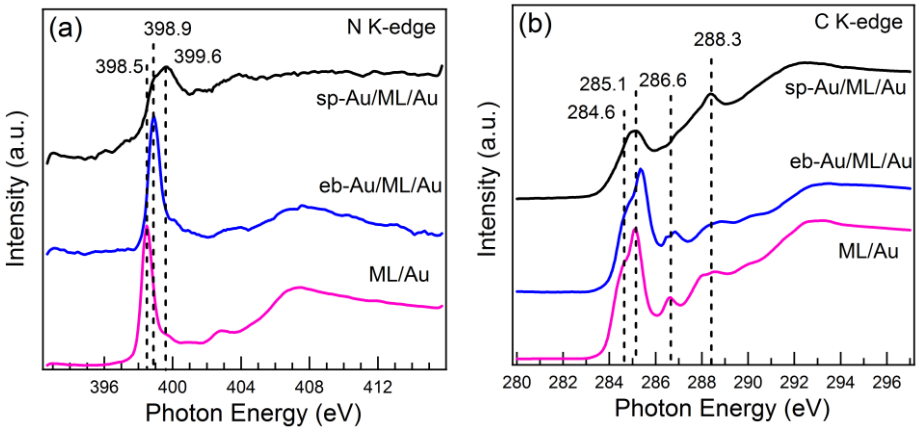

Figure 5.3 (a) N K edge and (b) C K edge spectra of ML/Au (pink), eb-Au/ML/Au (blue) and sp-Au/ML/Au (black).

The N K-edge XAS spectra (figure 5.3.a) of the ML/Au showed a resonance at 398.5 eV with a shoulder at around 399.6 eV. According to the literature on N K-edge spectra obtained for similar molecules containing terpyridine (tpy) groups, the peak at 398.5 eV can be assigned to a π^* resonance, which is typical for many aromatic systems comprising N atoms [18]. The shoulder at 399.6 eV was attributed to the nitrogen-to-metal coordination, indicating charge transfer from the nitrogen to the metal, similar to previous reports on N K-edge spectra of similar molecular systems, such as (tpy-Pt) [19] and (tpy-Pd) [18-20] complexes.

The C K-edge XAS spectra of the samples are shown in figure 5.3.b. The peak assignments were again made according to previously published data of tpy-containing monolayers assembled on metals. In the ML/Au spectrum, the resonance at 285.1 eV and the shoulder at 284.6 eV were attributed to the C(1s) to π^* C-N transition and the C(1s) to π^* C-C transition of the tpy ligand, respectively [18-21]. The 288.3 eV resonance was assigned to excitations from the C(1s) core level into hydrogen-derived antibonding orbitals, C–H* [18]. The resonance at about 286.6 eV is attributed to a C(1s) to π^* transition on the pyridine rings, while the two broad peaks at 292.85 eV are due to C1s to σ^* shape resonance [21, 22].

Upon capping the monolayer with Au by evaporation, (eb-Au/ML/Au), the shape of the spectral features in both N K-edge and C K-edge did not change,

however the peaks were observed to be slightly shifted towards higher excitation energies, indicating that the Au atoms diffuse inside the monolayer [23]. However, in case of the sputter-deposited Au cap (sp-Au/ML/Au), the main peaks were suppressed and broadened significantly. This indicates that, in contrast to deposition by evaporation, sputter-deposition of Au onto the molecules alters the C-C and C-N bonds of the ligand significantly. It must be taken into consideration that that a change in the bonds at the close proximity of the Co^{2+} would have a more drastic effect on its electronic environment than a change on the ligand further away from the center. Therefore Co L-edge spectra hold valuable information. In figure 5.4, the Co L_3 edge spectra of ML/Au, ML/Au after 4 runs of *in-situ* Au evaporation and sp-Au/ML/Au are given.

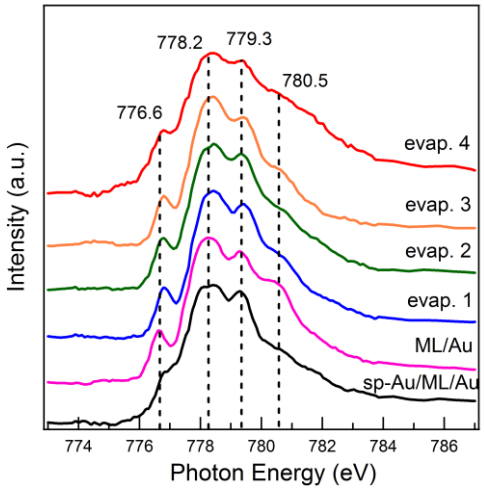

Figure 5.4 Co L3-edge spectra of ML/Au (pink), ML/Au after 4 following evaporation runs (blue, green, orange, red) and sp-Au/ML/Au(black)

The Co L_3-spectra originate mainly from electronic transitions from Co($2p_{3/2}$) core levels to Co(3d) unoccupied states. The 2p core holes and 3d valence electrons interact strongly, which localizes the core-excited states. In ionic transition metal complexes, the degree of localization is sufficiently high and the L-edge spectra can be described in terms of atomic multiplets. This enables

straightforward probing of the Co valence and the coordination environment of the Co ions in the complexes [24, 25].

In all Co L_3-edge spectra of the Co(tpy)(tpy-SH) complexes, with or without Au capping, significant multiplet peaks, which stem from Coulomb and exchange interactions between the 2p core hole and the 3d valance electrons, can be clearly observed. The atomic multiplet structures were consistent with Co^{2+} ions (electronic configuration $3d^7$) in the high-spin state [25-27]. More specifically, the spectra resemble those of various systems containing Co^{2+} ions in a (distorted) octahedral (O_h) ligand field, with a crystal field parameter 10*Dq*, or crystal field splitting energy, close to 1 eV, such as CoO [25-28]. Despite some variations in the spectra of capped- *versus* non capped monolayers, the presence of atomic multiplet peaks showed that the core-excited states remain localized on the Co-ions [25]. The spectra of eb-Au/ML/Au are very similar to that of the ML/Au, whereas the spectrum of the sp-Au/ML/Au shows significant changes in the multiplet structure. In eb-Au/ML/Au, the shoulder at 780.5 eV was slightly suppressed while the peak at 776.6 eV remained intense. However, for the sp-Au/ML/Au, both the 780.5 eV and 776.6 eV features were suppressed more significantly. Experiments and simulations in the literature on Co^{2+} ions in octahedral bonding environments demonstrate that, for larger values of 10Dq, the multiplet structure widens, such that the 776.6 eV and 780.5 eV features become more pronounced [25, 26, 28]. It can thus be concluded that the crystal field splitting energy is slightly smaller for the eb-Au/ML/Au compared to ML/Au, while sp-Au/ML/Au exhibits the smallest crystal field splitting.

Since Au-deposition by evaporation appears to leave the molecular bonds intact, the small reduction of the ligand field splitting can be ascribed to the effect of Au atoms embedding the molecules. The proximity of the electron clouds of the Au atoms closest to the central Co-ion may be expected to somewhat suppress the ligand field originating from the six N atoms that are covalently bonded to Co, reducing the energy splitting between the e_g and t_{2g} orbitals. For the sputter-capped sample, molecular bonds are broken during deposition, such that the Co-N bonds may be replaced by Co-Au bonds. In the most extreme case, the N-cage surrounding the Co-ions may be destroyed completely, with the Co being dissolved into the fcc Au matrix. A comparison with Co L-edge spectra of 1.5

at.% Co in Au, for which the Co multiplet structure can also be observed but is strongly suppressed suggests that the Co bonding environment remains at least partially intact [29].

5.3.3 Surface enhanced Raman spectroscopy (SERS) measurements

Raman spectroscopy provides detailed information about the structure, vibrational and electronic properties, and orientation of molecules [30]. It is based on the detection of energy differences in inelastic photon scattering, which are specific for a given chemical bond, allowing identification of molecules. The vibrational information forms a spectral fingerprint of the molecule. The typically very low spontaneous Raman scattering probability is greatly enhanced in the proximity of metal surfaces, due to the presence of local surface plasmons: giving rise to so-called surface-enhanced Raman scattering (SERS). SERS can provide information even for single molecules. Strong enhancement is observed for rough metallic surfaces due to electromagnetic enhancement, which originates from the enhancement of the incident electromagnetic field by surface plasmons of the metallic nanoparticles [31, 32].

Sputtered thin Au layers have been already used previously as SERS substrates due to their rough surfaces [30]. Therefore, our system, consisting of molecules with thiol end groups assembled on a thin sputtered Au surface, was expected to show significant Raman signals of the Co-complexes.

The details on the Surface enhanced Raman spectroscopy (SERS) measurements are given in Chapter 3. It was confirmed that no degradation of the molecular layer occurred with the laser power level used (10mW).

Figure 5.5 shows the Raman spectra of the samples ML/Au (pink), eb-Au/ML/Au (blue) and sp-Au/ML/Au (black). The distinct spectral features observed on ML/Au were due to the monolayers, and were comparable with the spectra of very similar complexes reported in literature [33-36]. The peaks between approximately 1100 and 1200 cm^{-1} were associated with phenyl-based modes [34]. The peaks between 1250 and 1290 cm^{-1} were attributed to the C-H wagging vibration, while the peak at 1020.5 cm^{-1} and the peaks between the regions 1332 cm^{-1} to 1600 cm^{-1} were assigned to pyridine ring breathing vibrations

[34]. The resonance at 1332 was attributed to the trigonal ring breathing vibration, mostly located on the central pyridine ring.

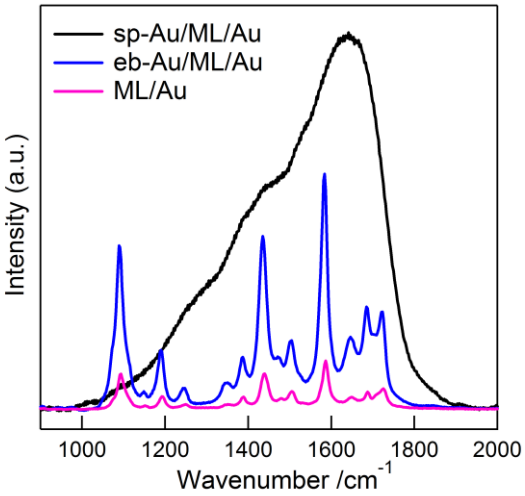

Figure 5.5 Surface-enhanced Raman spectra of ML/Au (pink), eb-Au/ML/Au (blue) and sp-Au/ML/Au (black).

After Au evaporation on the molecular monolayer, the peaks were further enhanced in the spectra in agreement with an earlier report [31]. The peak shapes remained unchanged, which indicates that the vibrational modes, and therefore the molecular bonds, were not altered significantly after Au evaporation. On the other hand, after sputter-deposition of Au; the distinct peaks were lost and a broad feature emerged instead, indicating that the molecular bonds were destroyed upon sputtering. This is consistent with the C- and N K-edge measurements, and points to damage due to the relatively high kinetic energy of the Au atoms arriving on the surface during sputter-deposition. Similar results have been reported in the past [30, 31].

Conclusions

Co(tpy)(tpy-SH) monolayers on top of Au films without additional Au cap, and with evaporated and sputtered Au caps were investigated by electron transport measurements, XAS and Raman spectroscopy. The Kondo upturn and the Kondo temperature were slightly higher for eb-Au/ML/Au (4.2K) compared to ML/Au (3K) and by far the highest for sp-Au/ML/Au (6.2K). Consistent with this, the extracted phase coherence lengths were the smallest for the sputtered Au cap (132 nm), and the largest for the bare Au film (584 nm). The higher Kondo upturn and T_K and the smaller phase coherence lengths can be attributed to enhanced interaction between the Co-ions and the Au conduction electrons. XAS and Raman spectroscopy showed that the molecular structure remained intact after e-beam evaporation. However upon sputtering, the molecular bonds are broken during deposition, such that the Co-N bonds may be replaced by Co-Au bonds. In the most extreme case, the N-cage surrounding the Co-ions may be destroyed completely, with the Co being dissolved into the fcc Au matrix. Still, the Co bonding environment remains at least partially intact, judging from the persistence of multiplet structure in the Co L-edge XAS spectra. Since the measurements of eb-Au/ML/Au samples showed that the location of the molecules has a small effect on the Kondo upturn, it can be concluded that the change in electronic environment of Co^{2+} the predominant reason for the highest T_K for the sputtered samples. These results imply that it is possible to change the strength of impurity-host interactions in such system with depositing a thin layer of Au on top the molecules by sputtering or e-beam evaporation. This allows for tuning of the magnetic impurity states, e.g. the spin quantum number, binding energy with respect to the host Fermi energy, and orbital overlap via the ligand structure around the ions.

References

[1] H.-B. Zhuang, Q.-f. Sun, and X. C. Xie, "Scanning tunneling spectroscopy of a magnetic atom on graphene in the Kondo regime," *EPL (Europhysics Letters),* vol. 86, p. 58004, 2009.

[2] A. V. Kretinin, H. Shtrikman, D. Goldhaber-Gordon, M. Hanl, A. Weichselbaum, J. von Delft*, et al.*, "Spin 1/2 Kondo effect in an InAs nanowire quantum dot: Unitary limit, conductance scaling, and Zeeman splitting," *Physical Review B,* vol. 84, p. 245316, 12/19/ 2011.

[3] M. A. Blachly and N. Giordano, "Kondo effect in one-dimensional Au(Fe)," *Physical Review B,* vol. 46, pp. 2951-2957, 08/01/ 1992.

[4] T. Gang, M. D. Yilmaz, D. Atac, S. K. Bose, E. Strambini, A. H. Velders*, et al.*, "Tunable doping of a metal with molecular spins," *Nat Nano,* vol. 7, pp. 232-236, 04//print 2012.

[5] V. Iancu, A. Deshpande, and S.-W. Hla, "Manipulation of the Kondo Effect via Two-Dimensional Molecular Assembly," *Phys. Rev. Lett.,* vol. 97, p. 266603, 12/28/ 2006.

[6] E. Minamitani, N. Tsukahara, D. Matsunaka, Y. Kim, N. Takagi, and M. Kawai, "Symmetry-Driven Novel Kondo Effect in a Molecule," *Phys. Rev. Lett.,* vol. 109, p. 086602, 08/22/ 2012.

[7] J. J. Parks, A. R. Champagne, G. R. Hutchison, S. Flores-Torres, H. D. Abruña, and D. C. Ralph, "Tuning the Kondo Effect with a Mechanically Controllable Break Junction," *Phys. Rev. Lett.,* vol. 99, p. 026601, 07/11/ 2007.

[8] R. P. Godwin and E. Lüscher, "Desorption energies of gold and copper deposited on a clean tungsten surface," *Surf Sci.,* vol. 3, pp. 42-48, 1// 1965.

[9] S. K. D. S. D. Ekpe, "Energy Deposition at the Substrate," in *Reactive Sputter Deposition*, ed Verlag Heidelberg Berlin: Springer, 2008, pp. 229-255.

[10] U. H. Kwon, S. H. Choi, Y. H. Park, and W. J. Lee, "Multi-scale simulation of plasma generation and film deposition in a circular type DC magnetron sputtering system," *Thin Solid Films,* vol. 475, pp. 17-23, 3/22/ 2005.

[11] T. A. Costi, A. C. Hewson, and V. Zlatic, "Transport-coefficients of the anderson model via the numerical renormalization-group," *Journal of Physics-Condensed Matter,* vol. 6, pp. 2519-2558, Mar 1994.

[12] F. Mallet, J. Ericsson, D. Mailly, S. Uenluebayir, D. Reuter, A. Melnikov*, et al.*, "Scaling of the low-temperature dephasing rate in Kondo systems," *Phys. Rev. Lett.,* vol. 97, Dec 1 2006.

[13] C. Bauerle, F. Mallet, F. Schopfer, D. Mailly, G. Eska, and L. Saminadayar, "Experimental test of the numerical renormalization-group theory for inelastic scattering from magnetic impurities," *Phys. Rev. Lett.,* vol. 95, Dec 31 2005.

[14] A. C. Hewson, *The Kondo problem to heavy fermions*: Cambridge university press, 1997.

[15] G. Bergmann, "Weak Localization and Its Applications as an Experimental Tool," in *50 Years of Anderson Localization*, E. Abrahams, Ed., ed: World Scientific, 2010.

[16] S. Hikami, A. I. Larkin, and Y. Nagaoka, "Spin-orbit interaction and magnetoresistance in the 2 dimensional random system," *Prog. Theor. Phys.,* vol. 63, pp. 707-710, 1980 1980.

[17] D. Bazin and L. Guczi, "Soft X-ray absorption spectroscopy in heterogeneous catalysis," *Applied Catalysis A: General,* vol. 213, pp. 147-162, 5/30/ 2001.

[18] E. Darlatt, C. H. H. Traulsen, J. Poppenberg, S. Richter, J. Kühn, C. A. Schalley*, et al.*, "Evidence of click and coordination reactions on a self-assembled monolayer by synchrotron radiation based XPS and NEXAFS," *Journal of Electron Spectroscopy and Related Phenomena,* vol. 185, pp. 85-89, 4// 2012.

[19] K. Mori, K. Watanabe, Y. Terai, Y. Fujiwara, and H. Yamashita, "Hybrid Mesoporous-Silica Materials Functionalized by PtII Complexes: Correlation between the Spatial Distribution of the Active Center, Photoluminescence Emission, and Photocatalytic Activity," *Chemistry – A European Journal,* vol. 18, pp. 11371-11378, 2012.

[20] J. Poppenberg, S. Richter, E. Darlatt, C. H. H. Traulsen, H. Min, W. E. S. Unger*, et al.*, "Successive coordination of palladium(II)-ions and terpyridine-ligands to a pyridyl-terminated self-assembled monolayer on gold," *Surf Sci.,* vol. 606, pp. 367-377, 2// 2012.

[21] C. Battocchio, G. Polzonetti, L. Gambino, N. Tuccitto, A. Licciardello, and G. Marletta, "Comparison between angular dependent NEXAFS analysis and theoretical calculations of molecular orientation of new functional mixed aromatic molecules deposited onto Au/Si(111)," *Nuclear Instruments and Methods in Physics Research Section B: Beam Interactions with Materials and Atoms,* vol. 246, pp. 145-150, 5// 2006.

[22] J. A. Horsley, J. Stöhr, A. P. Hitchcock, D. C. Newbury, A. L. Johnson, and F. Sette, "Resonances in the K shell excitation spectra of benzene and pyridine: Gas phase, solid, and chemisorbed states," *The Journal of Chemical Physics,* vol. 83, pp. 6099-6107, 1985.

[23] L. Lozzi, S. Santucci, and S. La Rosa, "Au/CuPc interface: Photoemission investigation," *Journal of Vacuum Science & Technology A,* vol. 22, pp. 1477-1481, 2004.

[24] Y. Liang, H. Wang, J. Zhou, Y. Li, J. Wang, T. Regier*, et al.*, "Covalent Hybrid of Spinel Manganese–Cobalt Oxide and Graphene as Advanced Oxygen Reduction Electrocatalysts," *J. Am. Chem. Soc.,* vol. 134, pp. 3517-3523, 2012/02/22 2012.

[25] A. M. H. R. Hakimi, F. Schoofs, R. Bali, N. A. Stelmashenko, M. G. Blamire, S. Langridge*, et al.*, "Origin of magnetism in cobalt-doped indium tin oxide thin films," *Physical Review B,* vol. 82, p. 144429, 10/20/ 2010.

[26] Y. J. Lee, M. P. de Jong, and W. G. van der Wiel, "Electronic structure of Co^{2+} ions in anatase Co:TiO_2 in relation to heterogeneity and structural defects," *Physical Review B,* vol. 83, p. 134404, 04/05/ 2011.

[27] F. M. F. de Groot, J. C. Fuggle, B. T. Thole, and G. A. Sawatzky, "2p x-ray absorption of 3d transition-metal compounds: An atomic multiplet description including the crystal field," *Physical Review B,* vol. 42, pp. 5459-5468, 09/15/ 1990.

[28] F. M. F. d. Groot, M. Abbate, J. v. Elp, G. A. Sawatzky, Y. J. Ma, C. T. Chen*, et al.*, "Oxygen 1s and cobalt 2p X-ray absorption of cobalt oxides," *Journal of Physics: Condensed Matter,* vol. 5, p. 2277, 1993.

[29] W. D. Brewer, A. Scherz, C. Sorg, H. Wende, K. Baberschke, P. Bencok*, et al.*, "Direct Observation of Orbital Magnetism in Cubic Solids," *Phys. Rev. Lett.,* vol. 93, p. 077205, 08/11/ 2004.

[30] P. E. Colavita, M. S. Doescher, A. Molliet, Ú. Evans, J. Reddic, J. Zhou*, et al.*, "Effects of Metal Coating on Self-Assembled Monolayers on Gold. 1. Copper on Dodecanethiol and Octadecanethiol," *Langmuir,* vol. 18, pp. 8503-8509, 2002/10/01 2002.

[31] T. Wadayama and M. Oishi, *Surface-enhanced Raman spectral study of Au nano-particles/alkanethiol self-assembled monolayers/Au(111) heterostructures*. Kidlington, ROYAUME-UNI: Elsevier, 2006.

[32] A. Merlen, V. Gadenne, J. Romann, V. Chevallier, L. Patrone, and J. C. Valmalette, "Surface enhanced Raman spectroscopy of organic molecules deposited on gold sputtered substrates," *Nanotechnology,* vol. 20, p. 215705, 2009.

[33] M. Presselt, B. Dietzek, M. Schmitt, J. Popp, A. Winter, M. Chiper*, et al.*, "Zinc(II) Bisterpyridine Complexes: The Influence of the Cation on the π-Conjugation between Terpyridine and the Lateral Phenyl Substituent," *The Journal of Physical Chemistry C,* vol. 112, pp. 18651-18660, 2008/11/27 2008.

[34] E. Campagnoli, J. Hjelm, C. J. Milios, M. Sjodin, Z. Pikramenou, and R. J. Forster, "Adsorption dynamics and interfacial properties of thiol-based cobalt terpyridine monolayers," *Electrochimica Acta,* vol. 52, pp. 6692-6699, 8/1/ 2007.

[35] A. C. Sant'ana, W. A. Alves, R. H. A. Santos, A. M. D. Ferreira, and M. L. A.Temperini, *The adsorption of 2,2':6', 2''-terpyridine, 4'-(5-mercaptopentyl)-2,2':6', 2''-terpyridinyl, and perchlorate on silver and copper surfaces monitored by SERS* vol. 22. Kidlington, ROYAUME-UNI: Elsevier, 2003.

[36] P. W. Hansen and P. W. Jensen, "Vibrational studies on bis-terpyridine-ruthenium(II) complexes," *Spectrochimica Acta Part A: Molecular Spectroscopy,* vol. 50, pp. 169-183, 1// 1994.

Chapter 6

Transport Properties of Graphene on Self Assembled Monolayers

In this chapter, transport properties of single layer graphene sheets on SiO_2/Si substrates functionalized with self-assembled monolayers of a NH_2-Co-BisTpy complex (Co complex), NH_2-Zn-BisTpy complex (Zn complex) and a 1:1 mixture of the two complexes were investigated. It was observed that the SAMs induced p-type doping of graphene, which resulted in a hysteresis effect. The observed hysteresis effect was used to build memory devices.

6.1 Introduction

Graphene is an atomically thin layer of sp^2 hybridized C atoms arranged in a honeycomb lattice. It has unique electronic properties arising from its characteristic band structure. Graphene is identified as a zero-gap semiconductor with its conduction band and valence band touching each other at a charge neutrality point, known as the Dirac point (V_d). Close to the Dirac point, the energy dispersion is linear and the carriers behave like massless, relativistic particles [1-3]. Graphene has attracted significant attention from both scientific and engineering communities due to its notable properties such as high mobility (values up to 120,000 $cm^2\ V^{-1}s^{-1}$ was observed in clean suspended graphene at 240 K [2]), flexibility and ultrathin structure. A number of reviews and books on graphene are available in literature [1, 4-7].

It is known that the electronic properties of graphene are very sensitive to the environmental conditions, since it is atomically thin and therefore all charge carriers reside at the surface. It can get doped easily with molecular species/adsorbates on the surface or in the interface between the substrate and graphene. In order to control the doping level or investigate the effect of doping or the doping mechanism, various self-assembled monolayers have been inserted at the interface between graphene and the dielectric. In some studies, SAMs were used to decrease the influence of doping from the environment or from the dielectric interface to obtain more stable graphene devices [8-11], while in other studies SAMs were used to purposely dope the graphene and shift the Dirac point [12,13] and thus introduce a hysteresis effect for memory device applications [14-18].

In this study, we tried to modify the properties of Chemical Vapor Deposition (CVD) grown graphene sheets by inserting a SAM at the graphene/SiO_2 interface. We used molecular complexes which included the same metal containing terpyridine groups ((Co-BisTpy) and (Zn-BisTpy)) as the complexes that were used in the Chapter 4 and Chapter 5. The original aim was to observe the effect of the spin of the Co complex on the graphene conduction. However, in temperature dependent measurements, the undoped graphene samples also showed a pronounced resistivity increase, possibly due to the much larger

influence of defects [19] or grain edges in graphene [20]. Any significant effect originating from the Co complexes could not be detected (data not shown). However, another interesting observation was present in the devices with molecular layers between the graphene/substrate interface: a hysteresis effect due to interaction of graphene with the underlying monolayers.

The hysteresis effect shows itself as a shift in the position of the maximum resistance point of graphene (Dirac point), depending on the gate voltage (V_g) sweep direction (forward or backward), maximum-minimum gate voltage range and sweep rate. The presence of a hysteresis loop due to the applied gate voltage creates clearly distinguishable states with different resistances, which can be used as states "0" (low resistance state) and "1" (high resistance state) in memory devices. Graphene layers on top of SiO_2/Si substrates are investigated and known to show the hysteresis effect [8, 9, 14, 21-25].

There are various reports on hysteresis effects observed in graphene devices, related to the presence of adsorbed molecules from ambient air. These effects are sometimes considered to be a drawback, causing instability in electrical behavior [8, 21]. However, hysteresis can also lead to memory effects, by applying voltages with opposite polarity.

The effect is in general attributed to electrical doping of the graphene as a result of charge redistribution over the graphene/adsorbate system. Several mechanisms have been proposed to explain the doping and associated hysteresis effect, as summarized below.

Carrier trapping

In this mechanism, charges originating from the graphene sheet are trapped in trap sites upon sweeping the gate voltage. These trap sites can be due to defects in the dielectric layer underneath, or adsorbates on the graphene surface or at the graphene/dielectric interface [8, 25, 26]. When the back gate starts at negative (positive) gate voltages, holes (electrons) are transferred from the graphene into trap centers, and the graphene experiences a more positive (negative) potential than due to that of V_g alone. The charge trapping thus results in the loss of holes (electrons), therefore the charge neutrality point is reached at

lower (higher) gate voltages compared to the neutral Dirac point, which is referred to as the downshift (upshift) of the V_d. Figure 6.1 shows the doping of graphene by trapping holes from graphene into traps in the dielectric surface (left) and the hysteresis behavior resulting from this charge trapping (right). The black curve shows the ideal curve for the gate sweep behavior of undoped graphene.

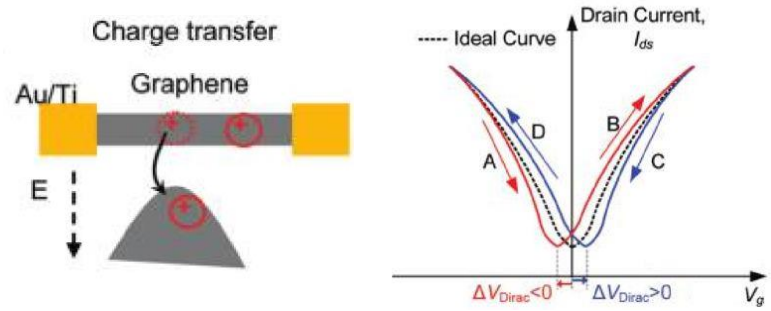

Figure 6.1 Charge transfer from graphene to charge traps in the dielectric (left) and the corresponding hysteresis effect (right) [4,10].

Electrochemical doping

Doping may also originate from electrochemical reactions between the graphene and adsorbate species from the environment such as H_2O and O_2 [9, 21] or NO_2, toluene [14]. The reaction is based on electron transfer from/to graphene to/from molecular species via an electrochemical redox reaction. For the case of H_2O and O_2 present at the surface or substrate-graphene interface, the reaction is:

$$O_2 + 2H_2O + 4e^-(\text{graphene}) \underset{\text{red}}{\overset{\text{ox}}{\rightleftharpoons}} 4OH^- \qquad (6.1)$$

The direction in which the reaction equilibrium shifts is determined by the relative height of the Fermi level of the graphene (E_F) and the Fermi level of the reducing and oxidizing species (E_{redox}). E_F and E_{redox} are controlled by the gate voltage and the density of redox states (D_{ox} and D_{red}) (figure 6.2). D_{ox} and D_{red} are electronic density of states (DOS) functions, which reflect the electron energy

level distribution around the oxidation potential (E_{ox}) and the reduction potential (E_{red}), for occupied (D_{ox}) and un-occupied states (D_{red}). E_{redox} is the energy where the DOS of reducing and oxidizing species are equal: $D_{ox}(E_{redox})=D_{red}(E_{redox})$ [9, 21].

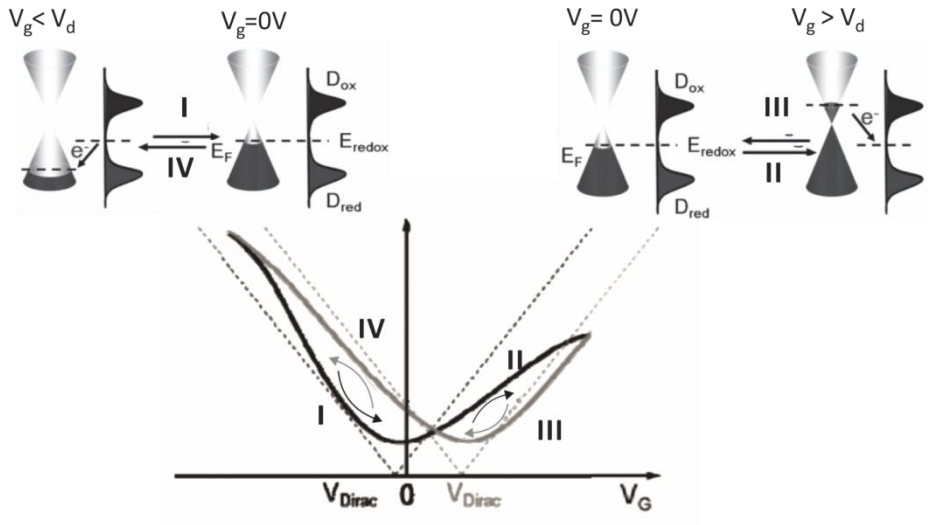

Figure 6.2 Schematic illustration of the dynamic process of charge-transfer between molecular species and graphene through a redox reaction under negative (top left) and positive (top right) gate voltages. The associated hysteresis effect in graphene FETs is shown at the bottom. The arrows indicate the sweep direction of the gate voltage, which helps to distinguish the hysteretic behavior in the electron- and hole doping sides, modified from Ref. [21].

The electrochemical doping mechanism and the resulting hysteresis are depicted in figure 6.2. A more detailed description can be found in Ref. [21]. When V_g is smaller than V_d, the reaction proceeds in the "backward" direction, which means that electrons are transferred from the molecular species to graphene, contributing to the filling of the graphene valance band (top left in figure 6.2). Therefore, when V_g is swept from negative voltages to zero (process I) the V_d will be reached at smaller voltages than zero, downshifting the V_d. When V_g is larger than V_d, the reaction proceeds in the "forward" direction, meaning that electrons are transferred from graphene to the molecular species (top right in figure 6.2). This results in a decrease of the electron concentration from the

conduction band of the graphene. Therefore, when V_g is swept from positive voltages to zero (process III), V_d will be reached before V_g reaches zero in this sweep direction, upshifting the V_d. For the processes of II and IV, a similar reasoning can be used. In this mechanism, the shift of the Dirac point is in the same direction as the case for the charge trapping mechanism: downshift (upshift) when the V_g is swept from negative (positive) to positive (negative) (bottom in figure 6.2).

Capacitive gating

In this mechanism, direct charge transfer from/to graphene is not present. Instead, charges are attracted to graphene as a result of the enhanced electric field due to polarization effects. This mechanism is observed when there are polar molecules/adsorbates on the graphene surface or at the dielectric/graphene interface, or when the dielectric surface itself contains polar groups. After applying V_g, dipoles (in the dielectric or polar molecules) align along the external electrical field, inverse charges move toward graphene from the contacts. Therefore, the local electric field near the graphene is enhanced. The enhanced local electric field helps to attract more majority carriers through the metallic contacts and the carrier density in graphene is effectively increased (figure 6.3) [25]. This mechanism is called "capacitive gating".

This type of hysteresis was reported in graphene/SAM/SiO_2 stacks, for SAMs including polar molecules [12, 13, 17]. It should be noted that the direction of the shift of V_d due to this doping mechanism is opposite to that of the charge trapping and electrochemical doping mechanisms. That is, the V_d upshifts (downshifts) when sweeping from negative (positive) to positive (negative) voltages. The direction of these shifts thus can be used to identify the mechanism.

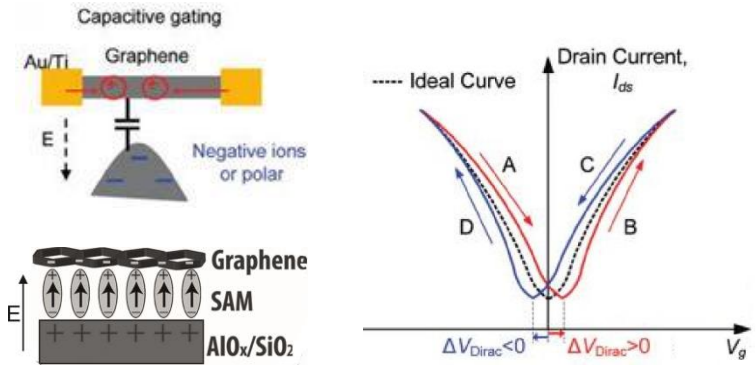

Figure 6.3 Capacitive gating induced charge doping in graphene. The external electric field polarizes the dipoles in dielectric [25] or SAM [12] and attracts electrons to the graphene. The hysteresis effect due to capacitive gating [8].

Initially, the mechanism of the doping in our case was predicted to be "electrochemical doping ", based on electron transfer from/to the metal core ion of the complexes. In Chapter 3, cyclic voltammetry measurements showed that Co^{2+} in the (Co-BisTpy) complex can be oxidized to Co^{3+} at relatively low energy (~0.25 eV). On the other hand, oxidation of Zn^{2+} was not observed in the literature possibly due to a very high oxidation energy. The cyclic voltammetry data of the (Zn-BisTpy) complex shows a reduction process at a potential in the range -0.77 to -0.81 V. This process was assigned to the reduction of the terpyridine-coordinated metal centers within the complex, that is, the Zn^{II}/ Zn^{I} couple [27]. Due to the difference in the oxidation behavior of the two metal ions, the hysteresis behavior in graphene/SAM systems containing Zn complexes was expected to be absent or smaller compared to those containing Co complexes. Although it was found that this was not the case, our graphene/SAM system proved to have a potential to be used in memory devices.

6.2 Sample preparation

The sample preparation was composed of substrate surface functionalization with SAMs, graphene transfer over the functionalized and bare (unfunctionalized) substrate surfaces, and device patterning.

We used highly doped Si wafers with 300nm thermally grown SiO_2 layers as substrates. Since the substrate surface was SiO_2 in this case, the complexes that were used in Chapter 4 and 5 were modified into complexes Bis-[4'-(5-aminopentyloxy)-2,2',6',2"terpyridine] cobalt(II) complex and Bis-[4'-(5-aminopentyloxy)-2,2',6',2"terpyridine] zinc(II) complex (NH_2-Co-BisTpy) and (NH_2-Zn-BisTpy) complexes. The substrates were functionalization with SAMs of the NH_2-Co-BisTpy complex (Co complex), the NH_2-Zn-BisTpy complex (Zn complex) and a 1:1 mixture of the two complexes (for see Chapter 3). In summary, the functionalization was performed in 3 steps (figure 6.4).

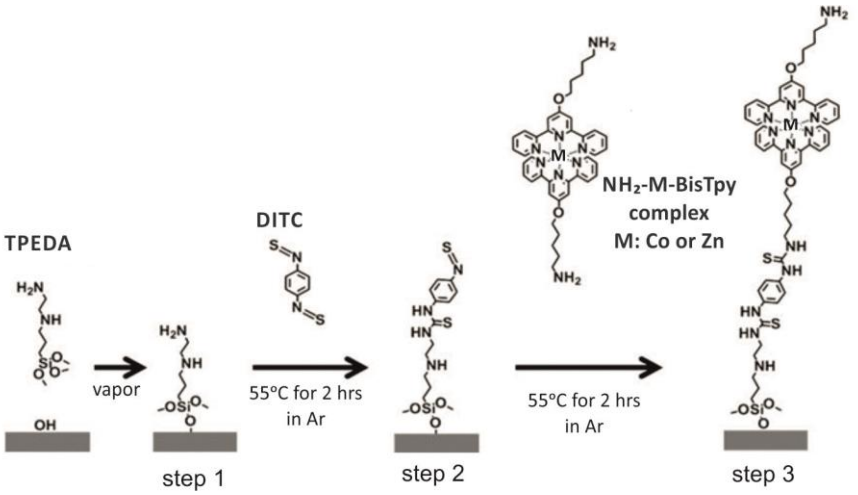

Figure 6.4 Scheme of NH_2-Co-BisTpy and NH_2-Zn-BisTpy SAM formation in three steps as explained in the main text.

Before the 1st step, the SiO_2 surface was activated in piranha solution. In the 1st step, a silanized monolayer was formed by vapor deposition of TPEDA (N-([3-(trimethoxysilyl) propyl]ethylenediamine). In the 2nd step, the resulting amine-terminated monolayers were functionalized with DITC (p-phenylene diisothiocyanate). In the 3rd step, the DITC-terminated monolayer was immersed in a 2mM ethanol solution of the NH_2-Co-BisTpy complex, the (NH_2-Zn-BisTpy) complex, or a 1:1 mixture of (NH_2-Co-BisTpy) and (NH_2-Zn-BisTpy) complexes. Each step was followed by a contact angle measurement in order to check the

modification of the surface. In addition, an x-ray photoemission (XPS) measurement was performed after the 2nd and 3rd steps to monitor the functionalization.

We used CVD grown graphene due to its scalability and manufacturability for large-area device integration. Graphene growth and patterning was performed by Matt Barnes and Gareth Jones from University of Exeter. Graphene was grown on 25um Alpha Aesar 99.99999% Cu foils. A PMMA (polymethylmethacrylate) support layer was spin coated over the graphene/foil and dried in vacuum for 60min. The graphene on the underside of the Cu foil (that was free of PMMA) was removed by argon ion etching. Subsequently, the Cu foil under the PMMA supported graphene was etched away by immersing in APS (ammonium persulphate ($(NH_2)_4S_2O_8$)) for 5 hours. The remaining graphene/PMMA was cleaned with DI water several times and scoop-transferred on the substrates with SAMs (will be referred to as Co complex, Zn complex and Co:Zn). One substrate without SAMs was also used (will be referred to as SiO_2). After graphene transfer, the samples were air dried overnight and then baked on a hotplate at 150°C for 30min. They were subsequently soaked in PMMA for 60 min at 60 °C followed by 2-propanol rinse and nitrogen dry.

The devices were patterned into Hall bar structures by e-beam lithography. The graphene layer outside the Hall bar was etched by reactive ion etching and the Au(30nm) contacts were deposited by evaporation. The device layout can be seen figure 6.5.b

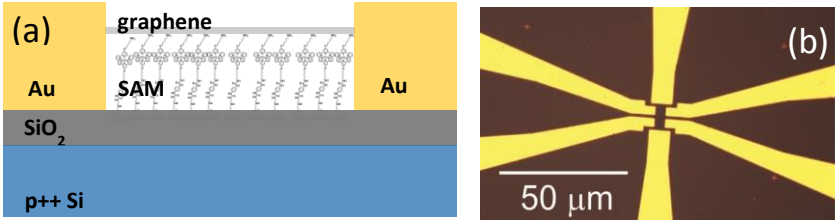

Figure 6.5 (a) Schematic of the device layout with SAMs between the substrate surface and graphene. (b) An optical microscope image of the device.

6.3 Results and Discussion

The monolayers were characterized by contact angle, XPS and Raman spectroscopy measurements. The transport properties of graphene with/without SAMs were investigated by measuring the resistance variation due to forward-backward gate sweeps.

6.3.1 XPS and contact angle measurements

The formation of SAMs was confirmed by water contact angle and XPS measurements. The contact angle measurements were acquired in air after each SAM formation step: after formation of the amino silane layer, after applying the DITC group and finally after complexation of the metal containing (NH_2-M-BisTpy) complex (M: Co and Zn). It was observed that the contact angle varied after each step, which implied the surface modification. The contact angle for the Co, Zn and the 1:1 mixture of Co and Zn monolayers were in the same range, indicating similar coverages on the surface.

The XPS measurements taken after the assembling of aminosilane and DITC on the SiO_2 surface (referred to as DITC in figure 6.6) and after complexation with the metal containing group (referred to as Co complex, Zn complex and the Co:Zn mixture) are shown below. Figure 6.6 shows a wide binding energy scan of all samples. It can be seen that all the expected elements are present and no signs of contamination is visible. It should be noted that the $Co2p_{1/2}$ and $Co2p_{1/2}$ peaks are visible only in the Co containing monolayers (Co and Co:Zn). Similarly $Zn2p_{1/2}$ and $Zn2p_{1/2}$ peaks are present only in Zn containing monolayers (Zn and Co:Zn).

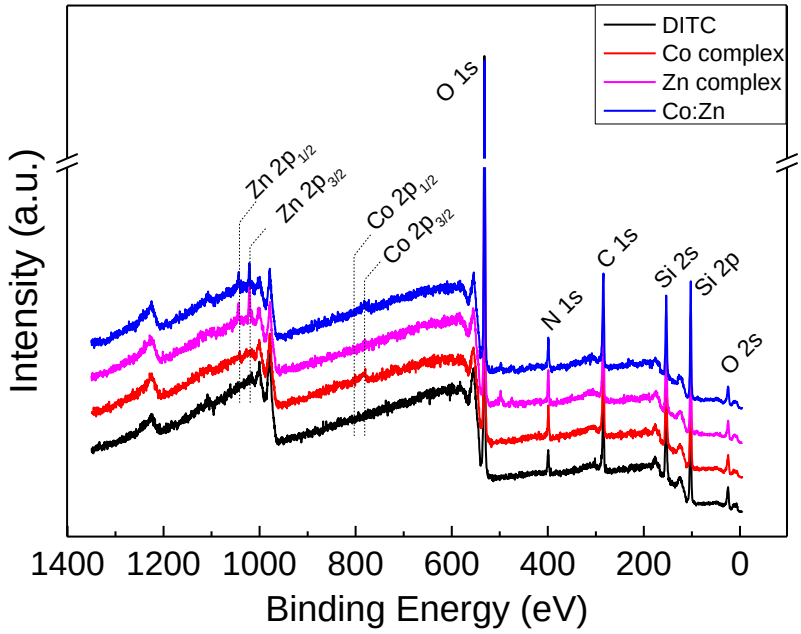

Figure 6.6 Wide scan XPS spectra of SiO2 surfaces decorated with aminosilane and DITC monolayer (DITC) (black) and complete complexes involving Co (red), Zn (pink) and a 1:1 mixture of Co and Zn complexes (Co:Zn mixture) (blue).The curves were shifted for clarity.

The chemical states of the C, N, Co and Zn atoms of the SAMs were investigated via narrow scans in C1s, N1s (figure 6.7), Co2p and $Zn2p_{3/2}$ (figure 6.8) regions.

In figure 6.7.b a minor positive shift (towards higher binding energy) in the N1s region (0.3eV) and in figure 6.7.a, a more pronounced positive shift (0.6 eV) in the C1s region was observed after application of the metal containing group (step 3) over the DITC/aminosilane SAMs. A similar positive shift was observed in literature when C1s spectra of $NH_2C_6H_4Si(OCH_3)_3$ (p-aminophenyltrimethoxysilane) SAMs were compared to that of $NH_2C_3H_6Si(OC_2H_5)_3$ (3-aminopropyltriethoxysilane) SAMs [17]. These two SAMs resemble our case before- and after complexation of the metal containing groups. Thus, the shift indicates that the complexation of the metal containing group with the DITC/aminosilane SAMs was successful [17]. The intensity of the C1s and N1s peaks increased in nearly the same amount after the complexation of the metal

containing group. After the complexation, the atomic ratios of C/N, calculated from the ratio of the peak areas, increased similarly compared to the aminosilane/DITC SAM (4.9±0.27). The C/N ratio for the Co SAM was 5.44±0.3, for the Zn SAM was 5.37±0.19 and for the mixed SAM was 5.23±0.24. The same increase was anticipated, since both metal containing groups include identical numbers of C and N atoms. The shifts in the peak positions, the increase in the intensity of the C1s and N1s peaks, and the contact angle measurements supported the successful complexation of the metal containing group with the existing DITC/aminosilane monolayer on the substrate surface.

In figure 6.8, narrow scans of the Co2p and $Zn2p_{3/2}$ regions were compared for the SAMs containing only Co or only Zn complexes and the SAMs consisting of 1:1 mixture of Co and Zn complexes. It was confirmed that the 1:1 mixture SAM contains both Co and Zn containing complexes. The Co and the Zn atomic concentration in the mixed SAM was similar, 1.26±0.3 and 1.53±0.7, respectively. This supports that the mixed SAM was indeed containing the Zn and the Co complexes in a nearly 1:1 ratio. The binding energies of both Co and Zn peaks indicated that these species were in oxidized state.

In order to make a rough estimation on the surface coverage of the complete complexes, the Si peak intensity after the 2nd (DITC) and the 3rd (NH_2-Co-BisTpy) SAM formation steps were used (I_0 and I, respectively). Using a very simplistic model, the thickness increase (d) upon adding of the NH_2-Co-BisTpy was roughly calculated to be 6 Å according to $I=I_0\ e^{-\mu d}$, where μ is the inelastic mean free path (μ was taken to be 4nm assuming that the density of the added layer was 1g/cm^2 according to [28]). Using the molecular weight of the NH_2-Co-BisTpy (845.85 g/mol), a surface coverage of roughly in the order of ~10^{13} molecule/cm^2 was estimated.

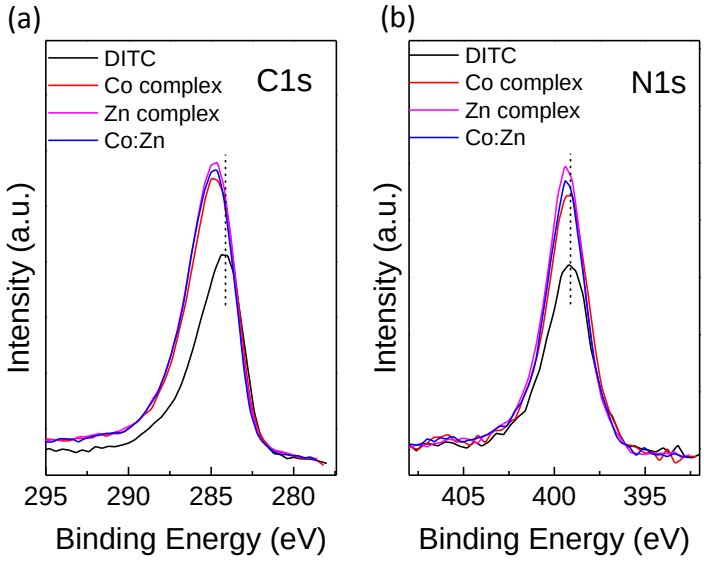

Figure 6.7 XPS scans of all samples in the (a) C1s and (b) N1s region. DITC stands for the SAM before complexation of the metal containing groups.

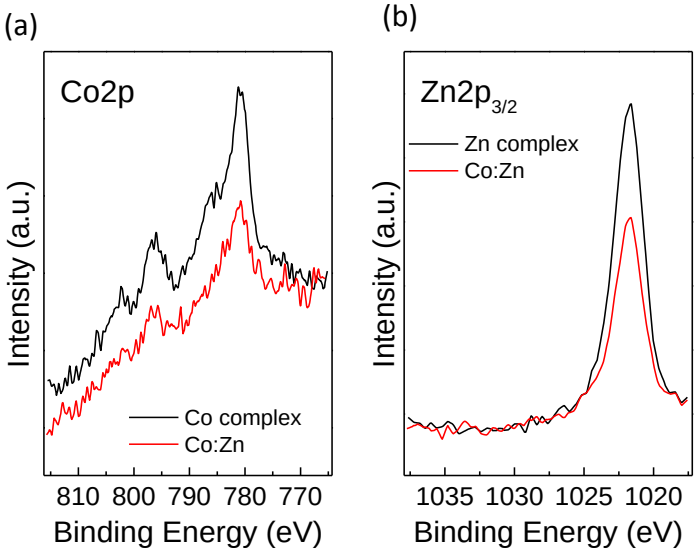

Figure 6.8 XPS scans of the (a) Co2p region for a Co complex SAM and a 1:1 mixed Co and Zn SAM, and (b) the Zn2p region for a Zn complex SAM and a 1:1 mixed Co and Zn SAM.

6.3.2 Raman Spectroscopy

Raman spectroscopy can provide insights into the doping level of graphene. The Raman spectra of pristine graphene on a bare SiO_2 (SiO_2) and on SiO_2 substrates that were decorated with Co complexes (Co), Zn complexes (Zn) and a 1:1 mixture of Co and Zn complexes (Co:Zn) were acquired using an excitation laser with a 532 nm wavelength. The obtained spectra from one set of samples can be seen in figure 6.9. In the spectra, differences were observed between SiO_2 sample and samples with SAMs. At the same time, variations between different type of SAMs were also present. This may be due to sample to sample differences in the structure of graphene sheets rather than the monolayer type. The comparisons (peak shifts, intensities) of G and 2D bands below were carried out for the measured set of samples in figure 6.9.a. It is very difficult to conclude about monolayer type related trends due to possible sample to sample differences.

As can be seen in figure 6.9.a, the Raman spectra of the bare graphene as well as graphene sheets transferred on the SAMs involved three typical peaks of CVD grown graphene monolayers [29, 30]. The peaks corresponded to the D band (1343 cm^{-1}), the G band (1588 cm^{-1}) and the 2D band (2683 cm^{-1}). The 2D peaks of all samples can be fitted with a single Lorentzian peak with a FWHM between 30-34 cm^{-1}, indicating that all graphene samples were monolayers. The presence of the D band indicates the existence of defects in all samples including the bare graphene, which is typically the case for CVD grown graphene sheets [29, 31-33].

The peak position of the 2D band (ω_{2D}) and G band (ω_G) upshifted slightly for the graphene on SAMs compared to graphene on SiO_2 (Figure 6.9.b). The upshift of the 2D peak may imply increase in number of graphene layers or the doping effect [32, 34]. As mentioned earlier, the fact that the 2D bands show a single Lorentzian peak indicates that the graphene layers were monolayer sheets [34]. Therefore, the upshift of the 2D band could be attributed to doping.

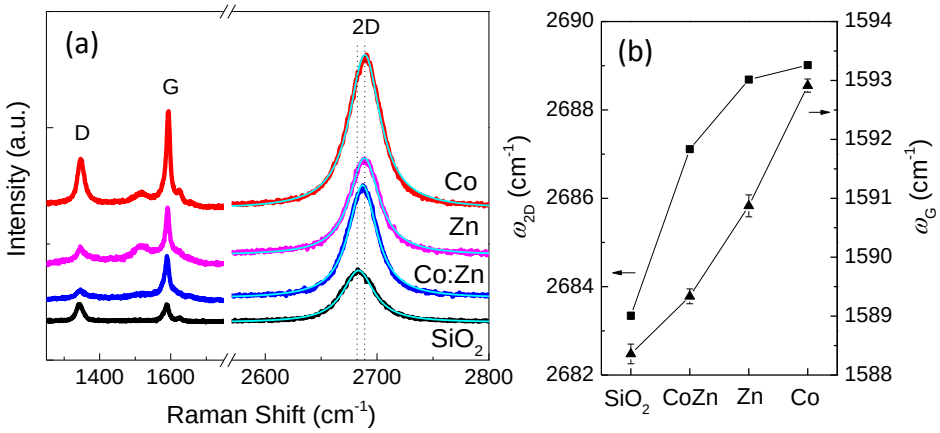

Figure 6.9 (a) Raman spectra for graphene on SAM modified SiO_2 and bare SiO_2 substrates. The blue curves are the Lorentz fits of the 2D peaks. (b) The peak position of the 2D band (ω_{2D}) and G band (ω_G).

Figure 6.10.a shows the ω_{2D} variation with ω_G. It was observed that the ω_{2D} increased with increasing ω_G for graphene on SAMs. In literature, reports on charge carrier modulation by an electric field effect attributes the increase of ω_{2D} with ω_G to p-type doping due to the accumulated charge carriers on graphene (for n-doped graphene the trend is in the opposite direction) [35, 36]. According to this, increasing ω_{2D} with increasing ω_G in our data indicates that the SAMs caused p-type doping of graphene [17].

The intensity of the 2D band (I_{2D}) was shown to be strongly dependent on charge carrier modulation by electric field effect doping [37]. Therefore the I_{2D}/I_G ratio is considered to be an important parameter to estimate the doping density [17, 35, 37] and used for molecularly doped graphene as well [13, 17]. Figure 6.10.b shows the I_{2D}/I_G ratio vs ω_G for graphene on SAMs and a bare SiO_2 substrate. The I_{2D}/I_G ratio decreased for the graphene on SAMs compared to graphene on the bare substrate. This behavior indicates that SAMs caused p doping of the graphene, especially for the Co complex [17, 21, 38].

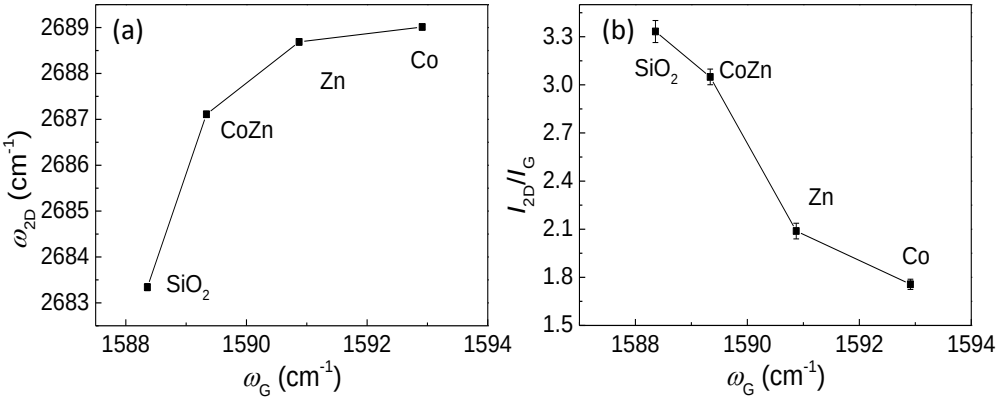

Figure 6.10 (a) Peak position of 2D (ω_{2D}) vs G (ω_G) peaks of graphene on SAM modified SiO_2 and bare SiO_2 substrates. (b) Intensity ratio of G and 2D peaks (I_G/I_{2D}) vs ω_G.

6.3.3 Electrical measurements

The transport properties of graphene devices on SiO_2/Si substrates functionalized with SAMs of Co complex (Co-SAM), Zn complex (Zn-SAM) and 1:1 mixed Co and Zn complexes (Co:Zn-SAM) and a bare SiO_2 substrate (SiO_2) were investigated by measuring the resistance dependence during forward and backward back gate voltage sweeps. The resistances was measured in a 2-terminal configuration by applying a constant current of 10nA across two adjacent leads in devices (figure 6.5.a). First, all devices were annealed in a N_2 flow for three hours at 170 ^oC (a safe temperature for avoiding degradation of the molecular complexes). Following, the devices were electrically contacted in air and loaded into the measurement system. Prior to start measurements, the samples were stayed in vacuum overnight inside the measurement system to reduce unintentional doping. All electrical measurements were conducted at room temperature and in vacuum ($5.6x10^{-6}$ mbar).

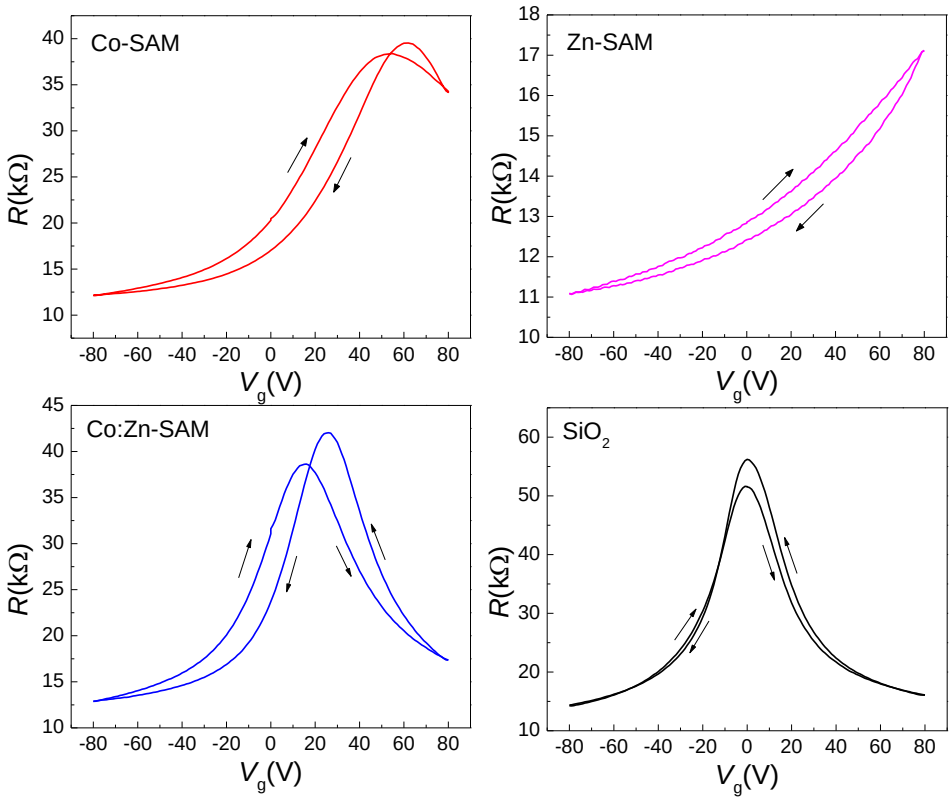

Figure 6.11 Forward and backward gate voltage (Vg) sweeps of graphene on SiO_2/Si substrates functionalized with SAMs of Co complex, Zn complex and 1:1 mixed Co and Zn complexes (Co:Zn) and a bare SiO_2 substrate.

Resistance vs gate voltage measurements with forward and backward gate sweeps were performed on four sets of devices containing each SAM type and SiO_2 (in total 16 devices). All samples containing SAMs showed similar behavior independent of molecule type (data not shown). All SiO_2 devices behaved the same way, which was different from the devices with SAMs (will be discussed further). Figure 6.11 shows measurement results from one set of devices that were loaded and measured together. The arrows in figure 6.11 indicate the sweep directions. The V_g sweep rate was 1V/s. The following measurements were also performed on this set of samples.

The Dirac point (V_d) on the SiO_2 sample was observed to be around 1V (±1V) for gate voltage sweeps in both positive and negative directions. The V_d of the graphene sheets on all SAM-treated substrates showed a shift toward positive gate voltages. In this set of samples, the largest shift was observed for the Zn-SAMs: the V_d moved beyond the applied V_g range. In other three sets, other SAMs also had large V_d in similar range and there were Zn-SAM samples having smaller V_d. The positive shifts of the V_d are consistent with p-type doping of the graphene, which was found in the Raman measurements as well. In addition, significant hysteresis effects were visible with clear Dirac point shifts between forward and backward sweeps (ΔV_d). In this set, Co-SAM and Co:Zn-SAM showed ΔV_d of around 7 V and 8 V, respectively. ΔV_d of the Zn-SAM is unknown, since V_d lies out of the measurement range. Similarly, SAM samples of the other sets (with V_d within the measured V_g range) showed ΔV_d in the same range. However, SiO_2 samples in all sets had nearly no V_d shifts (not more than 2V), therefore the hysteresis effect and the V_d shifts were attributed to the presence of the SAMs. The hysteresis direction in all SAM samples was the same. That is, the V_d downshifted during the voltage sweep from negative to positive, and upshifted during sweeping in the opposite direction.

The V_d positions and ΔV_d showed sample-to-sample variations in SAMs of each kind, independent of the molecular complex type. Therefore, from the electrical data, the SAM type could not be identified. This may be related to different amounts of graphene defects (Raman spectroscopy revealed that the graphene had defects). The mentioned sample-to-sample variations makes it very difficult to draw conclusions about SAM-type-related effects.

The hysteresis direction observed in the the SAM-devices was in agreement with the doping mechanisms of (1) charge transfer from/to graphene to the molecular species and (2) charge trapping at the molecules. That is, when the applied gate voltage was negative (positive) with respect to the Dirac point, holes (electrons) were injected from graphene to the SAM. When the gate voltage was swept to more positive (negative) voltages, since some of the holes (electrons) are transferred to the molecule, the V_d was being reached at smaller (bigger) voltages compared to the original V_d. A similar behavior was observed for graphene on a SAM of $NH_2(CH_2)_3Si(OEt)_3$ (APTES) (which is an NH_2 terminated

molecule, similar to the complexes in this study), and the hysteresis was attributed to charge trapping/detrapping by the APTES SAM, at the site of the nitrogen atom, which has an electron lone pair enabling the charge transfer [15-17]. Considering the findings of the APTES study and the absence of a clear dependence of the hysteresis behavior on the molecular complex type, the origin of the hysteresis in this study was also attributed to charge transfer between the graphene and the NH_2-group at the topside of the molecular complex. Due the absence of monolayer type related observations in the electrical data, the influence of the metal core (Co or Zn) of the complex is unclear at the moment. A way to observe metal core related effects could be investigating a version of these complexes without the NH_2-group on top.

In order to get a better understanding of the observed hysteresis behavior on SAM-devices, further experiments were carried out with gate voltage sweeps between different V_g ranges from ±10V to ±80V. Figure 6.12 shows only the sweeps between ±50 V, ±60 V, ±70 V and ±80 V. It was observed that in SAM samples the hysteresis became stronger as the V_g-range increased. This can be ascribed to the trapping of more charges in the SAM as V_g increases [31]. The SiO_2 sample on the other hand, did not show a pronounced, monotonic hysteresis increase.

As mentioned earlier, the hysteresis effect can be used to build a memory device. Depending on the gate voltage history, states of higher and lower resistance can be clearly distinguished which can be used as memory states “0” (off/high resistance state) and “1” (on/low resistance state), respectively. One can switch between the two states by applying gate voltages (writing-erasing voltages) that are much larger and much smaller than the V_d, which was ± 80V in our experiments. The reading voltage (V_{read}) can be chosen between the writing-erasing voltages where the two states are optimally distinguishable. The shift of the V_d (ΔV_d) is referred as the hysteresis window [15]. As shown in figure 6.12, the hysteresis window can be increased by increasing the writing and erasing voltage (V_g range). Another way to increase the hysteresis window is to increase the time that the writing voltage and erasing voltage is applied, though this obviously results in slower operation. Figure 6.13 shows *V*g sweeps for increasing switching times

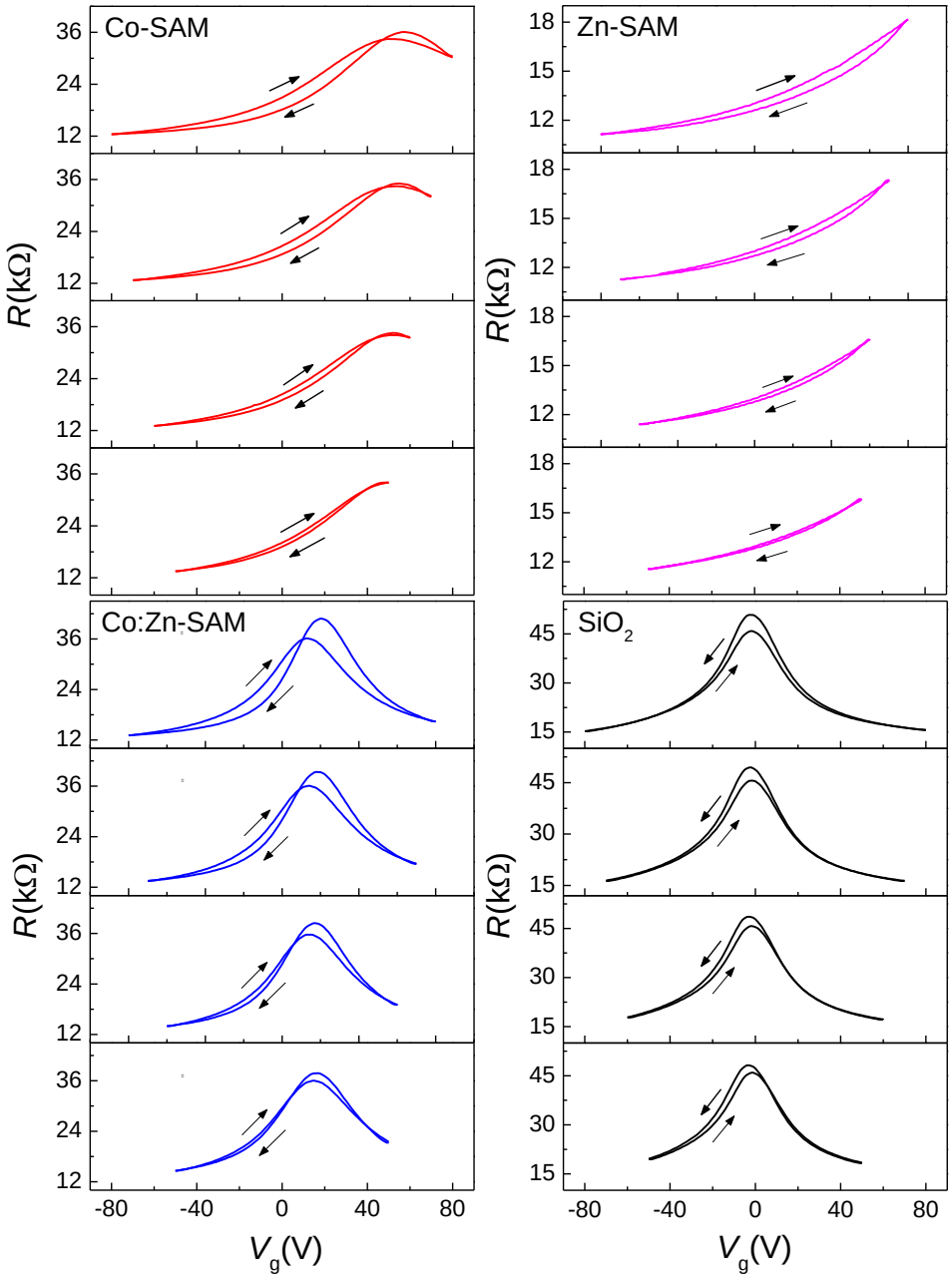

Figure 6.12 Gate voltage (Vg) dependence of the resistance between different Vg sweep ranges for graphene on SiO_2/Si substrates functionalized with SAMs of Co complex, Zn complex and 1:1 mixed Co and Zn complexes (Co:Zn) and a bare SiO_2 substrate.

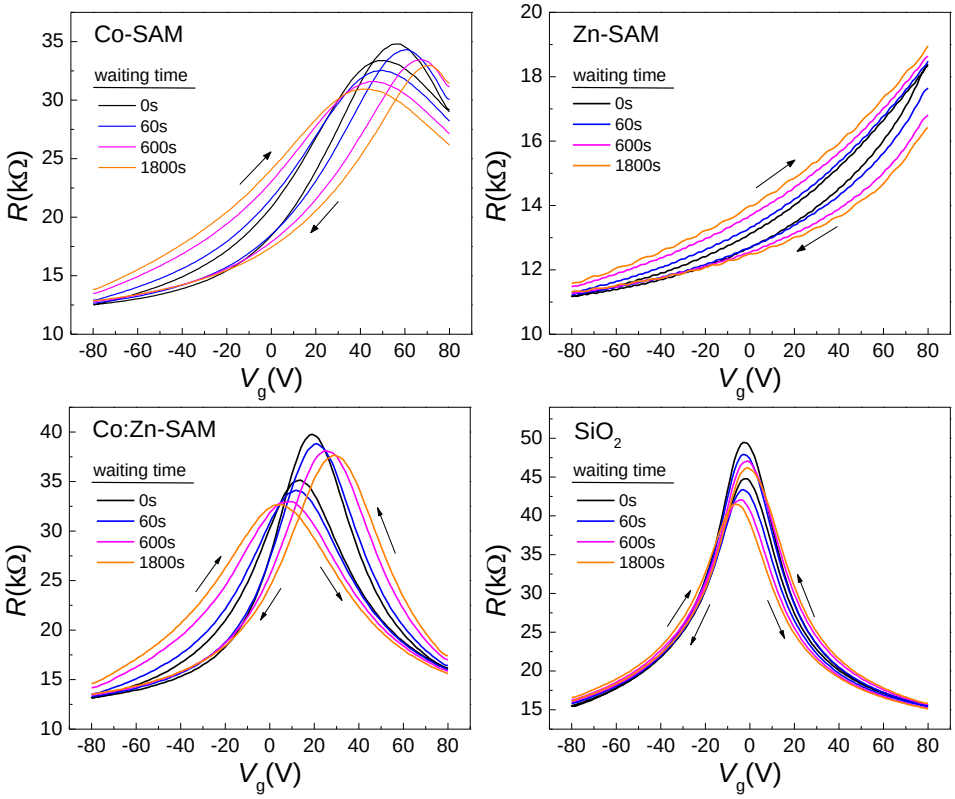

Figure 6.13 Gate voltage sweeps with varying writing and erasing times for graphene on SiO_2/Si substrates functionalized with SAMs of the Co complex, the Zn complex and 1:1 mixed Co and Zn complexes (Co:Zn) and a bare SiO_2 substrate .

The hysteresis window of the devices with SAMs increased with increasing writing/erasing times. Figure 6.14 shows the evalution of the hysteresis windows (ΔV_d) and density of charge trapping sites (n_{trap}) with varying writing/erasing times. The ΔV_d is extracted from figure 6.13 and the density of charge trapping sites, n_{trap}, was estimated from ΔV_d, as following [15, 16, 18]:

$$n_{trap} = \frac{\Delta V_d C_G}{e} \tag{6.2}$$

where C_G = 11.5nF/cm^2 is the gate capacitance per unit area for a 300nm thick SiO_2 layer and e is the unit charge. In this set of samples, the Co-SAM and the Co:Zn-SAM samples showed similar V_d shift for write/erase times up to 60s,

but for longer times, the ΔV_d and n_{trap} of the Co complex showed a more pronounced increase. The difference was suspected to be originating from sample to sample variations rather than the metal ion of the complex, as explained earlier. The Zn-SAM is not present in the figure, since the corresponding V_d was not in the measurement range. The graphene on the bare SiO_2 substrate showed hysteresis as well, but it was smaller compared to the SAM-samples. The charge trap densities for the graphene-on-SAMs samples (2.1×10^{12} cm^{-2}) was about 6-7 times larger than the SiO_2 sample (4×10^{11} cm^{-2}). The excess amount of trapped charge density was attributed to charges injected from graphene into trap sites on the SAMs [15, 16, 18]. From the suppression of the intensity of Si peak upon complexation of the Co-NH_2-Bistpy in XPS measurements, a surface coverage in the order of roughly 10^{13} was predicted. This suggests that only a part of the molecules are taking part in the charge trapping. The charge trapping of the SAMs was most likely due to electron accumulation on the molecules, more specifically on the N lone pairs of the NH_2 group of the complexes [15, 39].

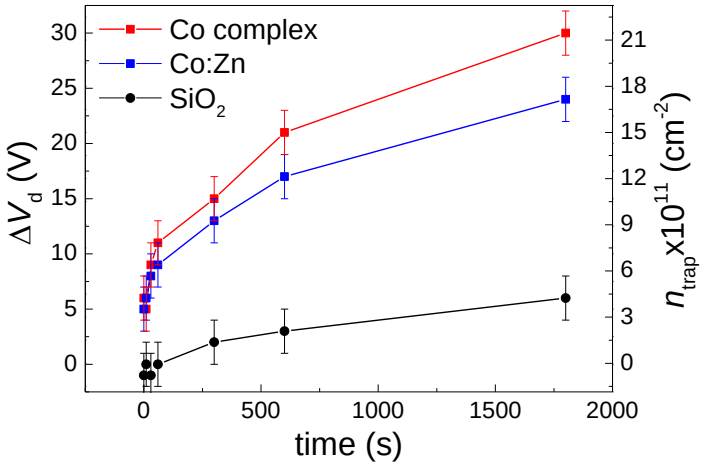

Figure 6.14 Dirac point shifts (ΔV_d) for varying writing and erasing times for graphene on SiO_2/Si substrates functionalized with SAMs of Co complex, 1:1 mixed Co and Zn complexes (Co:Zn) and a bare SiO2 substrate (V_g = ± 80V).

Due to the hysteresis effect observed in the devices, a memory effect was demonstrated by applying an alternating writing voltage of V_g = ±80V. The writing voltages and the reading voltages were applied for 60 s and 300 s, respectively. Reading voltages (V_{read}) were chosen to be the voltages at which the resistance difference of the forward and backward sweeps were maximum (found by subtracting the forward sweep from the backward sweep). Figure 6.15 shows the memory effect of Co-SAM, Co:Zn-SAM SiO_2 samples with the corresponding applied V_g. For the Co-SAM and Co:Zn-SAM samples, ΔV_d was present and V_d of the forward and backward sweeps was within the applied V_g range. Therefore, in these two devices it was possible to access four different resistance states: two states of high/low resistance in the hole-conduction regime (indicated by 1 and 4, respectively in figure 6.15.a and figure 6.15.b) and two states of high/low resistance in the electron-conduction regime (indicated by 2 and 3, respectively in figure 6.15.a and figure 6.15.b). The SiO_2 sample exhibited only two states because SiO_2 did not show a ΔV_d (Figure 6.15.d). The reading voltages on the hole- and electron conduction sides were 18V and 67V, respectively in Co-SAM and 27V and -13V in Co:Zn-SAM. It was observed that the states of high and low resistance were approaching to each other upon prolonged operation but they were still clearly distinguishable in the measured time scale with a long reading time of 300s. The sample containing the Co:Zn mixed SAM showed similar behavior. In the Zn complex device, the degradation of the high resistive state was more pronounced, but still the two states remained distinguishable.

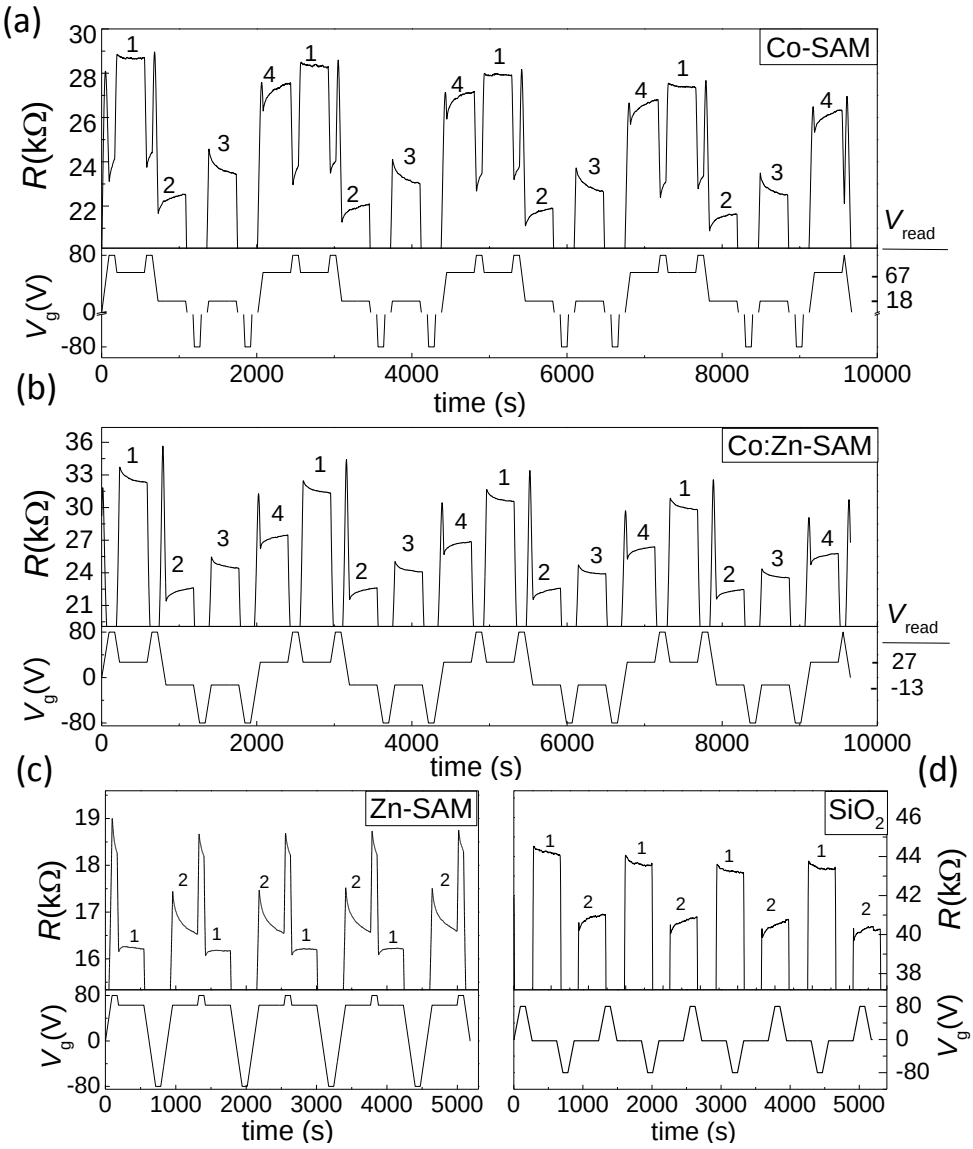

Figure 6.15 Memory effect of graphene on substrates functionalized with SAMs of Co complexes, Zn complexes, mixed Co and Zn complexes, and bare SiO2. The lower panels in the figures represent the applied Vg. Two pairs of high-low resistance (1-4 and 3-2) states are visible for Co-SAM and Co:Zn-SAM samples. The reading voltages are 67V and 18V in the Co-SAM and 27V and -13V in the Co:Zn-SAM device. The reading voltages for the Zn-SAM and SiO_2 devices were 63V and 0V, respectively.

Conclusions

Self-assembled monolayers of molecular complexes including (Co-BisTpy) and (Zn-BisTpy) were used to dope CVD-grown graphene. The SAMs of the molecular complexes were formed on SiO_2/Si substrates and the graphene was transferred onto these modified surfaces. Spin effect could not be detected in temperature dependent measurements. It was observed that the SAMs induced p-type doping of graphene and resulted in a hysteresis effect as a result of charge transfer and trapping. The sample-to-sample variations were larger than possible differences for SAMs containing different molecules. In spite of this, the large hysteresis effects were only observed for samples with SAMs. This SAM/graphene system can be used to make a memory device exhibiting up to 4 different resistance states.

References

[1] A. K. Geim and K. S. Novoselov, "The rise of graphene," *Nature materials,* vol. 6, pp. 183-191, 03//print 2007.

[2] K. I. Bolotin, K. J. Sikes, J. Hone, H. L. Stormer, and P. Kim, "Temperature-Dependent Transport in Suspended Graphene," *Phys. Rev. Lett.,* vol. 101, p. 096802, 08/25/ 2008.

[3] K. S. Novoselov, A. K. Geim, S. V. Morozov, D. Jiang, Y. Zhang, S. V. Dubonos*, et al.*, "Electric Field Effect in Atomically Thin Carbon Films," *Science,* vol. 306, pp. 666-669, October 22, 2004 2004.

[4] A. K. Geim, "Graphene: Status and Prospects," *Science,* vol. 324, pp. 1530-1534, June 19, 2009 2009.

[5] A. H. Castro Neto, F. Guinea, N. M. R. Peres, K. S. Novoselov, and A. K. Geim, "The electronic properties of graphene," *Rev. Mod. Phys.,* vol. 81, pp. 109-162, 01/14/ 2009.

[6] C. N. R. Rao and A. K. Sood, *Graphene: synthesis, properties, and phenomena*: John Wiley & Sons, 2013.

[7] H. Raza, *Graphene nanoelectronics: Metrology, synthesis, properties and applications*: Springer, 2012.

[8] Z. Liu, A. A. Bol, and W. Haensch, "Large-Scale Graphene Transistors with Enhanced Performance and Reliability Based on Interface Engineering by Phenylsilane Self-Assembled Monolayers," *Nano Letters,* vol. 11, pp. 523-528, 2011/02/09 2010.

[9] P. L. Levesque, S. S. Sabri, C. M. Aguirre, J. Guillemette, M. Siaj, P. Desjardins*, et al.*, "Probing Charge Transfer at Surfaces Using Graphene Transistors," *Nano Letters,* vol. 11, pp. 132-137, 2011/01/12 2010.

[10] X. Wang, J.-B. Xu, C. Wang, J. Du, and W. Xie, "High-Performance Graphene Devices on SiO2/Si Substrate Modified by Highly Ordered Self-Assembled Monolayers," *Advanced Materials,* vol. 23, pp. 2464-2468, 2011.

[11] S.-Y. Chen, P.-H. Ho, R.-J. Shiue, C.-W. Chen, and W.-H. Wang, "Transport/Magnetotransport of High-Performance Graphene Transistors on Organic Molecule-Functionalized Substrates," *Nano Letters,* vol. 12, pp. 964-969, 2012/02/08 2012.

[12] N. Cernetic, S. Wu, J. A. Davies, B. W. Krueger, D. O. Hutchins, X. Xu*, et al.*, "Systematic Doping Control of CVD Graphene Transistors with Functionalized Aromatic Self-Assembled Monolayers," *Advanced Functional Materials,* vol. 24, pp. 3464-3470, 2014.

[13] J. Park, W. H. Lee, S. Huh, S. H. Sim, S. B. Kim, K. Cho*, et al.*, "Work-Function Engineering of Graphene Electrodes by Self-Assembled Monolayers for High-Performance Organic Field-Effect Transistors," *The Journal of Physical Chemistry Letters,* vol. 2, pp. 841-845, 2011/04/21 2011.

[14] A. A. Kaverzin, S. M. Strawbridge, A. S. Price, F. Withers, A. K. Savchenko, and D. W. Horsell, "Electrochemical doping of graphene with toluene," *Carbon,* vol. 49, pp. 3829-3834, 10// 2011.

[15] H. Lv, H. Wu, K. Xiao, W. Zhu, H. Xu, Z. Zhang*, et al.*, "Graphene mobility enhancement by organosilane interface engineering," *Appl. Phys. Lett.,* vol. 102, pp. -, 2013.

[16] H. Lv, H. Wu, C. Huang, Y. Wang, and H. Qian, "Graphene nonvolatile memory prototype based on charge-transfer mechanism," *Applied Physics Express,* vol. 7, p. 045101, 2014.

[17] K. Yokota, K. Takai, and T. Enoki, "Carrier Control of Graphene Driven by the Proximity Effect of Functionalized Self-assembled Monolayers," *Nano Letters,* vol. 11, pp. 3669-3675, 2011/09/14 2011.

[18] C.-J. Shih, G. L. C. Paulus, Q. H. Wang, Z. Jin, D. Blankschtein, and M. S. Strano, "Understanding Surfactant/Graphene Interactions Using a Graphene Field Effect Transistor: Relating Molecular Structure to Hysteresis and Carrier Mobility," *Langmuir,* vol. 28, pp. 8579-8586, 2012/06/05 2012.

[19] P. O. Lehtinen, A. S. Foster, Y. Ma, A. V. Krasheninnikov, and R. M. Nieminen, "Irradiation-Induced Magnetism in Graphite: A Density Functional Study," *Phys. Rev. Lett.,* vol. 93, p. 187202, 10/27/ 2004.

[20] M. Fujita, K. Wakabayashi, K. Nakada, and K. Kusakabe, "Peculiar Localized State at Zigzag Graphite Edge," *J. Phys. Soc. Jpn.,* vol. 65, pp. 1920-1923, 1996/07/15 1996.

[21] H. Xu, Y. Chen, J. Zhang, and H. Zhang, "Investigating the Mechanism of Hysteresis Effect in Graphene Electrical Field Device Fabricated on SiO2 Substrates using Raman Spectroscopy," *Small,* vol. 8, pp. 2833-2840, 2012.

[22] P. Joshi, H. E. Romero, A. T. Neal, V. K. Toutam, and S. A. Tadigadapa, "Intrinsic doping and gate hysteresis in graphene field effect devices fabricated on SiO 2 substrates," *Journal of Physics: Condensed Matter,* vol. 22, p. 334214, 2010.

[23] E. Cazalas, I. Childres, A. Majcher, T.-F. Chung, Y. P. Chen, and I. Jovanovic, "Hysteretic response of chemical vapor deposition graphene field effect transistors on SiC substrates," *Appl. Phys. Lett.,* vol. 103, pp. -, 2013.

[24] H. Pinto, R. Jones, J. P. Goss, and P. R. Briddon, "Mechanisms of doping graphene," *physica status solidi (a),* vol. 207, pp. 2131-2136, 2010.

[25] H. Wang, Y. Wu, C. Cong, J. Shang, and T. Yu, "Hysteresis of Electronic Transport in Graphene Transistors," *ACS Nano,* vol. 4, pp. 7221-7228, 2010/12/28 2010.

[26] G. Kalon, Y. Jun Shin, V. Giang Truong, A. Kalitsov, and H. Yang, "The role of charge traps in inducing hysteresis: Capacitance–voltage measurements on top gated bilayer graphene," *Appl. Phys. Lett.,* vol. 99, pp. -, 2011.

[27] A. Winter, C. Friebe, M. Chiper, M. D. Hager, and U. S. Schubert, "Self-assembly of π-conjugated bis(terpyridine) ligands with zinc(II) ions: New metallosupramolecular materials for optoelectronic applications," *Journal of Polymer Science Part A: Polymer Chemistry,* vol. 47, pp. 4083-4098, 2009.

[28] P. J. Cumpson, "Estimation of inelastic mean free paths for polymers and other organic materials: use of quantitative structure–property relationships," *Surface and Interface Analysis,* vol. 31, pp. 23-34, 2001.

[29] W. Li, C. Tan, M. A. Lowe, H. D. Abruña, and D. C. Ralph, "Electrochemistry of Individual Monolayer Graphene Sheets," *ACS Nano,* vol. 5, pp. 2264-2270, 2011/03/22 2011.

[30] Y. Lee, S. Bae, H. Jang, S. Jang, S.-E. Zhu, S. H. Sim*, et al.*, "Wafer-Scale Synthesis and Transfer of Graphene Films," *Nano Letters,* vol. 10, pp. 490-493, 2010/02/10 2010.

[31] G. R. Turpu, M. W. Iqbal, M. Z. Iqbal, and J. Eom, "Relaxation in bi-stable resistive states of chemical vapor deposition grown graphene," *Thin Solid Films,* vol. 522, pp. 468-472, 11/1/ 2012.

[32] H. Gao, Z. Liu, L. Song, W. Guo, W. Gao, L. Ci*, et al.*, "Synthesis of S-doped graphene by liquid precursor," *Nanotechnology,* vol. 23, p. 275605, 2012.

[33] M. P. Levendorf, C. S. Ruiz-Vargas, S. Garg, and J. Park, "Transfer-Free Batch Fabrication of Single Layer Graphene Transistors," *Nano Letters,* vol. 9, pp. 4479-4483, 2009/12/09 2009.

[34] A. C. Ferrari, J. C. Meyer, V. Scardaci, C. Casiraghi, M. Lazzeri, F. Mauri*, et al.*, "Raman Spectrum of Graphene and Graphene Layers," *Phys. Rev. Lett.,* vol. 97, p. 187401, 10/30/ 2006.

[35] DasA, PisanaS, ChakrabortyB, PiscanecS, S. K. Saha, U. V. Waghmare*, et al.*, "Monitoring dopants by Raman scattering in an electrochemically top-gated graphene transistor," *Nat Nano,* vol. 3, pp. 210-215, 04//print 2008.

[36] S. Heydrich, M. Hirmer, C. Preis, T. Korn, J. Eroms, D. Weiss*, et al.*, "Scanning Raman spectroscopy of graphene antidot lattices: Evidence for systematic p-type doping," *Appl. Phys. Lett.,* vol. 97, pp. -, 2010.

[37] S. Pisana, M. Lazzeri, C. Casiraghi, K. S. Novoselov, A. K. Geim, A. C. Ferrari*, et al.*, "Breakdown of the adiabatic Born-Oppenheimer approximation in graphene," *Nature materials,* vol. 6, pp. 198-201, 03//print 2007.

[38] S. Lee, J.-S. Yeo, Y. Ji, C. Cho, D.-Y. Kim, S.-I. Na*, et al.*, "Flexible organic solar cells composed of P3HT:PCBM using chemically doped graphene electrodes," *Nanotechnology,* vol. 23, p. 344013, 2012.

[39] S. Kobayashi, T. Nishikawa, T. Takenobu, S. Mori, T. Shimoda, T. Mitani*, et al.*, "Control of carrier density by self-assembled monolayers in organic field-effect transistors," *Nature materials,* vol. 3, pp. 317-322, 05//print 2004.

Summary

Introducing organic molecules into electronic devices has attracted significant research interest due to its promise in both technological development and fundamental research. Organic molecular materials offer advantages such as low costs, easy fabrication, mechanical flexibility, light weight and chemical tunability, which can be engineered to obtain various functionalities. Organic molecules are used for many purposes as is summarized in Chapter 1. In this thesis work, they were used for magnetic doping of a thin metal film and for modifying electrical properties of graphene.

Theoretical concepts used throughout the thesis are introduced in Chapter 2. The main theoretical concepts are (1) the Kondo effect, which is a many-body phenomenon originating from the interaction of the spin of an isolated magnetic impurity with the spins of surrounding conduction electrons, (2) weak(anti-)localization, a correction to the resistivity due to the electron interference in disordered metals, and (3) crystal field theory, explaining the electronic structure and the origin of the spin state of the cenral metal ion in the molecular complexes used in this thesis work.

In Chapter 3, the experimental methods that were used throughout the thesis work are explained. The preparation of SAMs on thin Au films and SiO_2/Si substrates, and the deposition techniques that were used for Au capping of the SAMs are described. Low-temperature electric and magnetic characterization systems, synchrotron radiation techniques and surface-enhanced Raman spectroscopy are introduced.

A novel molecular fabrication method for magnetic doping of thin metal films with isolated impurities up to high concentrations is discussed in Chapter 4. A monolayer of paramagnetic molecular complexes, with a spin 1/2 core ion (Co complex), were inserted into thin disordered Au films as magnetic dopants. It was possible to dilute the magnetic impurity concentration by mixing the magnetic molecular complexes with their non-magnetic counterpart molecules (Zn complex: same molecules, but with spin 0 core ion) in solution. The concentration

of magnetic impurities in the metal film was directly proportional to the concentration of magnetic complexes in solution. Kondo and weak localization measurements demonstrated that the magnetic impurity concentration can be systematically varied up to ~800 ppm concentration without any sign of inter-impurity interaction, or undesired clustering often suffered from in alternative methods. Our fabrication method proved to be easy to apply and reproducible to a high degree for more than 5 independent fabrication runs. The results showed that magnetic impurity concentrations as high as 800 ppm are not high enough to cause impurities to interact with each other. Our molecular spin doping technique can be used for the investigation of very important physical phenomena such as the Kondo effect, RKKY interaction which can lead to further understanding of impurity-electron, impurity-impurity interactions.

It is also discussed in Chapter 4 that the Kondo effect is strong when a thin layer of Au is sputtered onto the monolayers on Au. Related to this, in Chapter 5, the effect of Au deposition over the monolayers (Au capping) on the magnetotransport properties is discussed. Au deposition was applied by two different techniques; magnetron sputtering and e-beam deposition. The kinetic energy per deposited atom in sputtering is about 2 orders of magnitude higher than for e-beam deposition. It was observed that the Au capping deposited by e-beam deposition increased the Kondo upturn and Kondo temperature (T_K) slightly compared to the uncapped case, while capping by magnetron sputtering had a more pronounced effect. The higher Kondo upturn and T_K, accompanied with smaller phase coherence lengths, can be attributed to enhanced interaction between the Co-ions and the Au conduction electrons. XAS and Raman spectroscopy showed that the molecular structure remained intact after e-beam evaporation. However upon sputtering, molecular bonds were broken during deposition. The change in the electronic environment of the Co^{2+} ions turned out to be the predominant reason for the higher T_K for the sputtered samples. These results imply that it is possible to change the strength of impurity-host interactions in such systems, by tuning the deposition parameters of Au top layers. This allows for tuning of the magnetic impurity states, e.g. binding energy with respect to the host Fermi energy, and orbital overlap via the ligand structure around the ions.

Graphene has attracted significant attention due to its exotic band structure and properties such as light weight, flexibility, optical transparency and very high charge carrier mobility. It is known that the electronic properties of graphene are severely affected by molecular species/adsorbates on the surface, or at the interface between the substrate and the graphene. In Chapter 6, molecular complexes (which involved the same metal ion-terpyridine groups that were discussed in Chapter 4 and Chapter 5) were inserted between graphene sheets and SiO_2/Si substrates The original aim was to observe the effect of the spin of the Co complex on the graphene conduction. However, temperature dependent measurements did not show any significant effect, possibly due to the much larger influence of defects or grain edges in graphene. Instead, it was observed that the molecular complexes induced p-type doping of the graphene, which resulted in a hysteresis effect due to charge transfer and trapping. The sample-to-sample variations were larger than any differences for molecular layers containing different molecules (Co complexes, Zn complexes or a mixture of the two complexes). However, large hysteresis effects were only observed for samples containing molecular complexes. It was shown that our molecular-layer/graphene system can be used to make memory devices exhibiting up to 4 different resistance states.

Samenvatting

Organische moleculen worden in toenemende mate geïntroduceerd in elektronische devices voor technologische ontwikkeling en fundamenteel onderzoek. Voordelen van moleculaire materialen zijn onder andere lage kosten, eenvoudige fabricage, mechanische flexibiliteit, licht gewicht en chemische variatie. Deze kunnen worden toegepast voor verschillende applicaties. Hoofdstuk 1 bevat een samenvatting van applicaties voor organische moleculen. In dit proefschrift worden moleculen gebruikt voor zowel magnetische doping van een dunne metaallaag als de modificatie van elektrische eigenschappen van grafeen.

Hoofdstuk 2 behandelt alle theoretische concepten die in dit proefschrift worden gebruikt: (1) het Kondo effect, een many-body fenomeen dat voortkomt uit de interactie van de spin van een geïsoleerde magnetische onzuiverheid met de spin van de elektronen uit de omgeving, (2) zwakke(anti-)lokalisatie, een correctie van de karakteristieke weerstand door elektroneninterferentie in wanordelijke metalen, en (3) de kristalveldtheorie, die de elektronenstructuur en de spintoestand van de centrale ionen in de in dit werk gebruikte moleculaire complexen beschrijft.

In hoofdstuk 3 worden alle gebruikte experimentele methoden uitgelegd. De preparatie van moleculaire zelf-assemblage op een dunne goudlaag en een Si/SiO_2 substraat, en de depositie technieken voor het bedekken van dergelijke lagen met goud worden uitgelegd. Elektrische en magnetische metingen op lage temperatuur, synchrotronstraling technieken en surface-enhanced Raman spectroscopie worden behandelt.

In hoofdstuk 4 wordt de ontwikkeling beschreven van een nieuwe moleculaire fabricagemethode voor het magnetisch doteren van dunne metaalfilms met geïsoleerde onzuiverheden tot hoge concentraties. Een monolaag van paramagnetische moleculaire complexen, met een spin ½ centraal ion (Co complex), wordt hierbij in een wanordelijke film van goud ingebed als magnetische dotering. De concentratie van magnetische onzuiverheden kon worden verdund door middel van het mengen van de magnetische moleculaire

complexen met een niet-magnetische tegenhanger (dezelfde moleculen, maar met een spin 0 centraal ion) in oplossing. De concentratie van de magnetische onzuiverheden in de metaalfilms was direct proportioneel met de concentratie van de magnetische complexen in oplossing. Metingen van het Kondo effect en zwakke lokalisatie laten zien dat de concentratie tot ~800 ppm systematisch gevarieerd kan worden zonder dat interactie tussen de magnetische onzuiverheden plaatsvindt. Ook is geen ongewenste clustering waargenomen, die vaak voorkomt bij het gebruik van alternatieve methoden. Onze fabricagemethode is eenvoudig toepasbaar en in hoge mate reproduceerbaar in meer dan 5 onafhankelijke fabricage runs. De resultaten lieten zien dat concentraties van magnetische onzuiverheden van 800 ppm niet genoeg waren om interactie tussen hen te krijgen. Onze moleculaire spin doping techniek kan gebruikt worden voor het onderzoek naar belangrijke fysische fenomenen, zoal het Kondo effect, RKKY interactie, hetgeen kan leiden tot een beter begrip van de interactie tussen elektronen en onzuiverheden en onzuiverheden onderling.

Zoals ook in hoofdstuk 4 besproken, was het Kondo effect duidelijk te zien als een dunne laag goud wordt gesputterd op de op een goudlaag aangebrachte monolagen. Met betrekking tot dit resultaat, wordt in hoofdstuk 5 het effect van gouddepositie op een monolaag (Au capping) op de magnetotransport eigenschappen geanalyseerd. Er wordt van twee verschillende gouddepositie methodes gebruik gemaakt: magnetron sputtering en e-beam depositie. Voor sputtering is de kinetische energie per atoom twee ordes van grootte hoger dan voor e-beam depositie. Bij een goud toplaag aangebracht met e-beam depositie was er een lichte toename in de Kondo upturn and de Kondo temperatuur (T_k) vergeleken met samples zonder toplaag. Voor magnetron sputtering was er een duidelijker effect te zien. De hogere Kondo upturn en T_k, samengaand met een kleinere fasecoherentie lengte, kan worden toegeschreven aan een verhoogde interactie tussen de Co-ionen en de geleidingselektronen in het goud. XAS en Raman spectroscopie laten zien dat de moleculaire structuur intact blijft na e-beam depositie, terwijl tijdens sputtering de moleculaire bindingen worden gebroken. De verandering in de elektronische omgeving van de Co^{2+} ionen lijkt de voornaamste oorzaak te zijn van de hogere T_k in samples met een gesputterde toplaag. Deze resultaten geven aan dat het mogelijk is de sterkte van de interacties tussen de onzuiverheden en hun omgeving te beïnvloeden door de

depositieparameters van de dunne goud toplaag te variëren. Hierdoor kunnen de eigenschappen van de magnetische onzuiverheden worden veranderd, zoals de bindingsenergie ten opzichte van de Fermi energie, en de overlap van orbitalen via de ligand structuur rond de ionen.

Grafeen heeft veel aandacht getrokken vanwege de exotische bandenstructuur en eigenschappen zoals licht gewicht, flexibiliteit, optische transparantie en zeer hoge mobiliteit van ladingsdragers. Het is bekend dat de elektronische eigenschappen van grafeen door moleculaire adsorbaten op het oppervlak, of aan het grensvlak tussen het substraat en het grafeen, significant beïnvloed kunnen worden. In hoofdstuk 6 worden moleculaire complexen (met dezelfde metaal ion-terpyridine groepen als in hoofdstuk 4 en 5 beschreven) tussen het grafeen en het SiO_2/Si substraat geplaatst. Het oorspronkelijke doel was om het effect te bestuderen van de spin van het Co complex op de geleiding van grafeen. De temperatuurafhankelijke metingen lieten echter geen significant effect zien, mogelijk ten gevolge van de veel grotere invloed van defecten en domeinranden in grafeen. In plaats daarvan werd gevonden dat de moleculaire complexen p-doping van grafeen veroorzaken en een hysterese-effect door ladingsoverdracht en trapping. De variaties van sample tot sample waren groter dan mogelijke verschillen tussen samples met verschillende moleculen (Co complexen, Zn complexen of een mengsel van deze twee complexen). Grote hysterese-effecten waren echter allen zichtbaar voor samples die moleculaire complexen bevatten. Er is aangetoond dat deze systemen gebruikt kunnen worden voor geheugencomponenten met tot 4 verschillende weerstandswaarden.

Acknowledgements

Here, the thesis has come closer to the end and I find the opportunity to thank all the wonderful people who helped me in numerous ways during the years of my PhD. During my study, I learned a lot from many people and established precious friendships. I am grateful for all the help and support I received for completing the work that was described in this thesis and experiments that could not make it into the thesis.

Foremost, I would like to thank my supervisor and promotor Wilfred van der Wiel for giving me the opportunity to join Nanoelectronics Group as a PhD student. You have been a great supervisor, I could not have asked for any better. I am thankful for your encouragement and guidance. Your enthusiasm, knowledge, experience and creative ideas was what kept me going. I am very much grateful for your kindness and patience during these years. I will never forget your help and support during our hospital adventure with Serkan, you made us feel secure.

I would like to thank Michel de Jong, who helped me on every stage of my study with his valuable suggestions and feedback. Thank you for your support, this work would not be completed without your help. I have been very impressed of your energy, enthusiasm and engineering skills, especially during the experiments in Max Lab. I am grateful to you for reading my thesis, your comments and corrections improved it significantly. Thank you for your contribution to the Dutch translation of the summary section as well. Your support during Serkan's illness and Dutch translation of his reports was deeply appreciated.

I gratefully acknowledge European Research Council (ERC) for the financial support of this research.

I would like to thank to my committee members Jurriaan Huskens, Harold Zandvliet, Cees Otto, Bart Jan Ravoo, Tamalika Banerjee and Monica Craciun for taking time from their busy schedule to evaluate this work.

I would like to thank Jurriaan for his invaluable contribution to my project. I am grateful to you for offering me the facilities in the chemical lab and all the insightful discussions. My special thanks go to Aldrik, Deniz, Richard and Carlo. Deniz and Richard synthesed the molecular complexes, without your efforts this study would not be possible. Deniz was one of the first people I met here, thank you for your advices and support. I am thankful for the friendship of him and his lovely wife Burcu. Carlo, you were a very nice person to work with. Thank you for your efforts on monolayer formation in the last chapter until the last days of your PhD.

It is my pleasure to thank to Tian, Saurabh and Elia. I am very pleased to have met you as my collogues and my friends. You made my life much easier by helping me whenever I needed. I learned a lot from all of you. Tian, thank you for your help and guidance starting from my first day. Saurabh, your critical look improved this work and your existence made our office a happy place. Elia, thanks to your programming skills and suggestions, the time for the measurements with Heliox decreased significantly. Thank you for letting me bother you so frequently. I would like to acknowledge Wauter Naber, preliminary data of my project was from him and Peter Tijsen who was working on the project when I started my PhD.

I would like to thank to Monica Craciun together with Saverio Russo from University of Exeter for our collaboration. I am grateful for the contribution of Matt Barnes and Gareth Jones, PhD students of Monica Craciun for their hard work on fabrication of graphene devices and Raman spectroscopy measurements that were discussed in Chapter 6.

I acknowledge Cees Otto and Aufried Lenferink for the Raman spectroscopy measurements in Chapter 5 and the valuable discussions.

My special thanks go to my dear paranymphs and office mates Ksenia and Janine. You bring color to our office and the whole group. I feel very lucky to have you as my friends. You made my life in NE happy and enjoyable. I will always remember your encouragement, support and the cheerful conversations we had in our office. Thanks to your help and support I will survive the big day with less worry. Janine, thank you for the Dutch translation of the summary of my thesis.

Julia, Lan Anh and Ina thank you for your warm friendship. I hope the best for all of you.

I would like to thank Floris for constructive feedbacks during group meetings. Johnny (Sanderink), Thijs and Martin, I sincerely thank you for being always helpful with the problems in the lab. Karen and Susan, it was a great pleasure to meet you. Karen, thank you for helping with the administrative work. Susan, it was very nice of you and Chimene to visit us. Your cheerful laugh will be one of the memories I will not forget.

I would like to acknowledge all the cleanroom staff, especially Robert, Rene, Huib and Hans for keeping the equipment running and for their useful advices. Gerard Kip, thank you for the XPS measurements of Chapter 4 and Chapter 6.

I had the chance to work with many great people in our group. Kai, thank you for your help in the lab, even outside the working hours. My office neighbors Michel (Zoontjes) and Filipp, thank you for enduring my frequent visits to your office. Pepijn, it was a pleasure to work with you on your bachelor's thesis. I would like to thank to all (current and former) members of our group; Johnny (Wong), Wen, Peter (Eerkes), Rabindra, Zhihua, Bojian, Dogan, Matthias, Chris, Joost, Sergei, Elmer, Jelmer, Hao, Frank, Liang (Du), Celestine, Dilu, Liang (Ye), Jelle, Gulbostan, Koert and Maarten. I wish success for all of you in your studies.

There are a number of people that I am so much grateful to have met. Oktay and Banu thank you for your friendship and help. Your visits to Enschede made the best weekends. Our time in Samos was one of my best holidays. Serkan, Banu and Hadi, thank you so much for your help when I needed. Ozgun, I will never forget how you took care of me when I got sick, I deeply appreciate it. Mustafa, Tolga and Hale, thank you for the nice time together.

My special thanks go to Serkan. You inspired me to join the group. I am thankful for the many good and bad days that we shared together. Your endless support and care made it possible for me to complete this thesis. I wish all the success and happiness in the world for you.

My friends from Turkey, thank you for being with me all these years. Your presence made my life most enjoyable and my visits to Turkey were more valuable thanks to you. I love all of you!

Kuslarim Hale, Duygu, Feyzan, Nihan, Nevin and Filiz, I am blessed with friends like you. You always encouraged me and cheered me up. Hale and Feyzan, being abroad was easier with you on the other side of the phone. Duygu, having a conversation with you was enough to see the problems smaller. I wish success and happiness for all you girls.

Ece, I am more than happy that you moved to Izmir, I will be able to see you whenever I am there. Thank you for being there for me all these years. Cagricim, my best friend from high school, I am very happy to have you all these years.

I made several valuable friends during my master study in IZTECH that I still love deeply. Baris, Tuna, Atike, Nesli, Mehmet, Irem thank you for making time to see me during my holidays in Turkey. Our meetings were one of the best parts of my holidays.

Most importantly, my family, my dear mother, my dear father, brother, sister and my lovely niece Derin; thank you with all my heart for your confidence and endless support. You were the ones that I missed the most. I always felt safe and strong thanks to your love and support. I am most thankful and happy to have you as my family. I love you very much! ☺

Sevgili ailem; oncelikle Annecim ve Babacim; Abicim, Ablacim ve sevgili yegenim Derincim. Desteginiz ve sevginiz icin size tum kalbimle tesekkur ederim. Doktora surecince en cok ozlediklerim sizler oldunuz. Sevginiz ve desteginiz sayesinde kendimi guclu ve guvende hissettim. Ailem oldugunuz icin cok mutlu ve minnattarim. Sizi cok seviyorum! ☺

Derya

November, 2014

Author Biography

Derya Ataç was born in Balikesir, Turkey, on March 2nd, 1984. She obtained her B.Sc. degree from Dokuz Eylül University, Izmir, Turkey, in 2007. Following, she obtained her M.Sc. degree from Department of Physics in Izmir Institute of Technology (IZTECH), Turkey, in 2010. During her M.Sc. study, she worked as a teaching and research assistant at IZTECH. She carried out her M.Sc. work on "Growth and Characterization of Aluminum Doped Transparent and Conductive Zinc Oxide Thin Films" under supervision of Assoc. Prof. Yusuf Selamet and Assist. Prof. Süleyman Tarı. She joined NanoElectronics Group in University of Twente in June 2010 as a PhD candidate and worked on "Tuning Electron Transport in Metal Films and Graphene with Organic Monolayers" under supervison of Prof. Dr. Wilfred G. van der Wiel. Her doctoral research is described in this thesis. Currently she is a postdoctoral researcher in the project "Towards the fabrication of (multiple) Graphene layers by (CVD/ALD) for energy-storage applications" under supervision of Assoc. Prof. Michel de Jong and Assist. Prof. Alexey Kovalgin.

Publications

D. Ataç, T. Gang, M. D. Yilmaz, S. K. Bose, A. T. M. Lenferink, C. Otto, M. P. de Jong, J. Huskens and W. G. van der Wiel *Tuning the Kondo effect in thin Au films by depositing a thin layer of Au on molecular spin-dopants* Nanotechnology 24 375204 (2013).

T. Gang, M. Deniz Yilmaz, **D. Ataç**, S. K. Bose, E. Strambini, A. H. Velders, M. P. de Jong, J. Huskens and W. G. van der Wiel *Tunable Molecular Spin Doping of a Metal* Nature Nanotechnology 7, 232–236 (2012).

S. Büyükköse, B. Vratzov, **D. Ataç**, J van der Veen, P.V. Santos and W.G. van der Wiel *Ultrahigh-frequency surface acoustic wave transducers on ZnO/SiO2/Si using nanoimprint lithography Nanotechnology* **23** 315303 (2012).